THERMOELECTRIC MATERIALS BASED ON DOPED STRONTIUM TITANATES

Marja Jerič

Doctoral Dissertation
Jožef Stefan International Postgraduate School
Ljubljana, Slovenia

Supervisor: Prof. Dr. Miran Čeh, Jožef Stefan Institute, Ljubljana, Slovenia

Evaluation Board:
Prof. Dr. Slavko Bernik, Chair, Jožef Stefan Institute, Ljubljana, Slovenia
Asst. Prof. Dr. Boštjan Jančar, Member, Jožef Stefan Institute, Ljubljana, Slovenia
Prof. Dr. Mehmet Ali Gülgün, Member, Sabanci University, Instanbul, Turkey

MEDNARODNA PODIPLOMSKA ŠOLA JOŽEFA STEFANA
JOŽEF STEFAN INTERNATIONAL POSTGRADUATE SCHOOL



Marja Jerič

THERMOELECTRIC MATERIALS BASED ON DOPED STRONTIUM TITANATES

Doctoral Dissertation

TERMOELEKTRIČNI MATERIALI NA OSNOVI DOPIRANIH STRONCIJEVIH TITANATOV

Doktorska disertacija

Supervisor: Prof. Dr. Miran Čeh

Ljubljana, Slovenia, October 2016

Acknowledgments

I would like to thank Prof. Dr. Miran Čeh for supervision, guidance and encouraging words through my years at the Jožef Stefan Institute. His knowledge and experience have helped me to grow as a scientist. Also, I would like to thank Prof. Dr. Slavko Bernik, Asst. Prof. Boštjan Jančar and Mateja Košir for useful discussions in the field of thermoelectrics and interpretation of the measurement results. Thank you Silvo Zupančič and Marjeta Maček Kržmanc from K9 as well as Dr. Aljaž Iveković and Matej Kocen from K7 for technical assistance in high-temperature sintering and TGA measurements, Medeja Gec and Andreja Šestan from K7 and CEMM for TEM sample preparations and Dr. Janez Zavašnik from CEMM for TEM investigations. I would like to thank Luka Suhadolnik for drawing the schematic model of the thermoelectric module. Sincere gratitude goes also to Prof. Dr. Mehmet Ali Gülgün from the Sabanci University in Turkey.

Thanks to all of the wonderful and special people at the K7 department, especially everybody from "room E51" for helpful discussions and suggestions, as well as the informal laughs and cries in between.

Special thanks go to Dr. Johannes de Boor for employing the thermoelectric measurements, for thorough discussions on the results, and also for kindness and a pleasant company during my stay at the Institute of Materials Research in Cologne (DLR). Werner Schönau is gratefully acknowledged for thermal conductivity measurements. I would like to kindly thank the entire Department of Thermoelectric Materials and Systems (Prof. Dr. Eckhard Müller at the forefront) as well as the Department of Central Analytical Research and Metallography at the Institute of Materials Research for thoughtful assistance and fruitful suggestions. I am sincerely grateful for the opportunity to carry out a part of my PhD research at DLRs' Institute of Materials Research.

I would like to thank the Slovenian Research Agency for funding this PhD work. Also, I thank the Slovene Human Resources Development and Scholarship Fund for financially supporting my research work in Germany.

Last but not least, I would like to express my sincere gratitude to my family: Karlo, my two precious children: Ivana and Marko, my parents and my big sister, for their love and selfless support. Hvala!

Abstract

Increasing concern for the environment promotes the search for alternative sources of energy that would be ecologically sound. In this sense, waste heat, produced as a side effect of machines operation, could be used as a power source by employing thermoelectric devices. Thermoelectric generators are namely able to convert temperature gradient directly into electrical voltage by the Seebeck effect.

Up to date, most used thermoelectric materials have been metal-based alloys, which however suffer from high temperature instability, when they are not properly protected. Their constituents are frequently also highly toxic. In mid-90' of the 20^{th} century scientists' attention was drawn towards oxide-based materials, which showed promising power factors and high temperature stability. Since then, many oxide materials have been studied, such as ZnO, $Ca_3Co_4O_9$, $CaMnO_3$, and $SrTiO_3$. In spite of all the efforts, the thermoelectric figure of merit of oxide-based materials remains low. It is commonly accepted that the drawback of oxide-based materials arises from the high thermal conductivity originating from the crystal lattice vibrations (phonons).

PhD work, presented in this thesis, consisted of synthesis of thermoelectric materials based on Nb-doped $SrTiO_3$ (STNO), their microstructural characterization and physical properties measurements. In order to study the effect on the materials reduction, STNO was sintered in different atmospheres. The results showed that the reducing atmosphere strongly affects the reduction of Ti^{4+} into Ti^{3+} of STNO and the formation of oxygen vacancies. Secondly, STNO microstructure was modified by introducing phonon barriers in order to lower the lattice thermal conductivity. Planar faults of the Ruddlesden-Popper (RP) phases are well known structural defects in the $SrTiO_3$ system and were therefore chosen to be introduced in the STNO. Two approaches were employed: addition of RP-type platelet seed crystals (Seeded STNO) or addition of excess SrO or CaO (STNO;SrO or STNO;CaO). RP-type seeds were made by the molten salt synthesis and characterized in a separate study. Microstructural investigations of Seeded STNO showed anisotropic grains with up to 100 μm planar faults in a matrix of large isotropic grains, which contained no faults. Addition of excess SrO resulted in numerous planar faults running in all directions. STNO;CaO showed a microstructure of isotropic to slightly anisotropic grains with planar faults. In comparison with STNO, prepared with the same synthesis conditions, the thermal conductivity of Seeded STNO was only slightly reduced, however, the electrical conductivity showed a metallic behavior. On the other hand, the thermal conductivity was significantly reduced in STNO:SrO and especially in STNO:CaO. In this regard, adding excess CaO has proven to be a promising method to lower thermal conductivity of STNO. On the other hand, addition of seeds resulted in enhanced electrical conductivity and consequently the highest thermoelectric figure of merit of the studied microstructures.

Povzetek

Naraščajoča skrb za okolje spodbuja iskanje novih, okoljsko neoporečnih virov energije. Tako bi, na primer, odvečno toploto, ki se kot stranski produkt tvori pri delovanju naprav, lahko s pomočjo termoelektričnih naprav uporabili kot vir energije. Termoelektrični generatorji lahko namreč pretvorijo temperaturni gradient neposredno v električno napetost preko Seebeckovega učinka.

Trenutno so najbolj uprabljani termoelektrični materiali kovinske zlitine, ki pa so visokotemperaturno nestabilne, kadar niso ustrezno zaščitene. Poleg tega velikokrat sestojijo iz močno strupenih komponent. Pozornost znanstvenikov se je zato sredi 90. let 20. stoletja usmerila v materiale na osnovi oksidov, ki izkazujejo obetaven faktor moči in visokotemperaturno obstojnost. Od takrat se je preučevalo veliko vrst oksidnih materialov, kot so ZnO, $Ca_3Co_4O_9$, $CaMnO_3$ in $SrTiO_3$. Kljub prizadevanjem pa termoelektrični faktor kvalitete ostaja nizek. Splošno je sprejeto, da pomanjkljivost materialov na osnovi oksidov predstavlja visoka termična prevodnost, ki izhaja iz nihanja kristalne mreže (fononov).

Doktorsko delo, predstavljeno v tej disertaciji, je obsegalo sintezo termoelektričnih materialov na osnovi $SrTiO_3$, dopiranega z Nb (STNO), mikrostrukturno karakterizacijo in meritev fizikalnih lastnosti. Da bi preučili vpliv na redukcijo materiala, smo STNO sintrali v različnih atmosferah. Rezultati so pokazali, da reduktivna atmosfera močno vpliva na redukcijo Ti^{4+} v Ti^{3+} v STNO in na nastanek kisikovih praznin. Nadalje je bil cilj spremeniti mikrostrukturo STNO z uvajanjem fononskih preprek, ki bi znižale termično prevodnost. Planarne napake Ruddlesden-Popperjevih (RP) faz so znani strukturni defekti v sistemu $SrTiO_3$ in smo jih zato izbrali za uvajanje v strukturo STNO. Uporabili smo dva pristopa: dodatek ploščičastih kristalov RP-tipa (STNO s kalmi) ali dodatek presežka SrO ali CaO (STNO;SrO ali STNO;CaO). Kali RP-tipa so bile narejene s sintezo taljenih soli in preučene v ločeni raziskavi. Preiskava mikrostrukture STNO s kalmi je razkrila anizotropna zrna z do 100 μm dolgimi planarnimi napakami v matrici velikih izotropnih zrn brez defektov. Dodatek presežnega SrO je povzročil številne planarne napake v vseh smereh. STNO;CaO je izkazal mikrostrukturo izotropnih do rahlo anizotropnih zrn s planarnimi napakami. V primerjavi s STNO, pripravljenim v istih pogojih sinteze, je bila termična prevodnost STNO s kalmi znižana le v manjši meri, medtem ko je bila električna prevodnost kovinskega tipa. Po drugi strani pa sta bili termični prevodnosti STNO;SrO in predvsem STNO;CaO znatno znižani. Na podlagi teh rezultatov se je izkazalo, da je dodatek presežnega CaO obetaven način zniževanja termične prevodnosti v STNO. Po drugi strani pa je dodatek kali v STNO povzročil večjo električno prevodnost in posledično najvišji termoelektrični faktor kvalitete med preučevanimi mikrostrukturami.

Contents

List of Figures **xv**

List of Tables **xvii**

Abbreviations **xix**

Symbols **xxi**

1 Introduction **1**
1.1 Thermoelectric Effect ... 1
1.1.1 Electron and Heat Transport in Solids ... 3
1.1.1.1 Electron Transport ... 3
1.1.1.2 Heat Transport ... 4
1.1.2 Electron and Phonon Scattering ... 5
1.1.3 Electrical Resistivity and Conductivity ... 6
1.1.4 Seebeck Coefficient ... 6
1.1.5 Thermoelectric Figure of Merit ... 7
1.2 High-Temperature Oxide Thermoelectrics ... 8
1.2.1 Nb-Doped $SrTiO_3$ Thermoelectric Material ... 10
1.2.1.1 Crystal Structure of $SrTiO_3$ and Nb-Doped $SrTiO_3$ ... 10
1.2.1.2 Defect Chemistry of Nb-Doped $SrTiO_3$ ... 13
1.2.1.3 Energy Band Structure of $SrTiO_3$ and Nb-Doped $SrTiO_3$ ... 15
1.2.1.4 Carrier Concentration of Nb-Doped $SrTiO_3$ ... 16
1.2.1.5 Thermoelectric Properties of Nb-Doped $SrTiO_3$ ... 17

2 Aims and Hypothesis **21**
2.1 Description of the Problem ... 21
2.2 Aims of the Dissertation ... 21
2.3 Organisation of the Experimental Work ... 22

3 Materials and Methods **23**
3.1 Synthesis ... 23
3.1.1 Solid State Synthesis of 20% Nb-Doped $SrTiO_3$ ... 23
3.1.2 Molten Salt Synthesis of Ruddlesden-Popper Type Platelet Crystals ... 24
3.1.3 Seeded Nb-Doped $SrTiO_3$ ... 24
3.1.4 Nb-Doped $SrTiO_3$ with Excess SrO or CaO ... 25
3.2 Characterisation Methods ... 25
3.2.1 X-Ray Powder Diffraction (XRD) ... 25
3.2.2 Scanning Electron Microscopy (SEM) ... 25
3.2.3 Transmission Electron Microscopy (TEM) ... 25
3.2.4 Thermogravimetric Analysis (TGA) ... 26
3.2.5 Rietveld Analysis ... 26

3.2.6 Measurement of Thermoelectric Properties 26
3.2.6.1 Thermal Conductivity Measurements 26
3.2.6.2 Seebeck Coefficient and Electrical Conductivity Measurements 26

4 Nb-Doped $SrTiO_3$ Synthesized in Different Atmospheres 27

5 Lowering the Thermal Conductivity of $Sr(Ti_{0.8}Nb_{0.2})O_3$ by SrO and CaO Doping: Microstructure and Thermoelectric Properties 33

6 Influence of Nb-Doping of $Sr_3Ti_2O_7$ Platelet Crystals on Their Composition and Crystal Growth 43

7 An Enhanced Thermoelectric Figure of Merit for $Sr(Ti_{0.8}Nb_{0.2})O_3$ Based on RP-Polytype Induced Microstructure 57

8 Conclusions 65

References 67

Bibliography 75

Biography 77

List of Figures

Figure 1.1: Shematic presentation of thermoelectric module and a single thermocouple, (enlarged in the inset) consisting of two types of material: p-type and n-type.....3
Figure 1.2: Energy band diagrams of conductors, semiconductors or insulators. Based on the positions of the valence and conduction band with the relation to the Fermi level, semiconductor can be intrinsic, n-type or p-type.....4
Figure 1.3: Thermoelectric parameters; Seebeck coefficient S, electrical conductivity σ and thermal conductivity κ and power factor $S^2\sigma$ and figure of merit ZT depending on the carrier concentration of Bi_2Te_3. 8
Figure 1.4: Review of thermoelectric materials, based on their optimal operating temperature and toxicity (a) and abundancy of materials constituents in the Earth's crust (b) adapted from He et al.....9
Figure 1.5: Unit cell of $SrTiO_3$ and TiO_6 octahedra, formed by the oxygen atoms. Green spheres are the strontium atoms, blue is the titanium and red are the oxygen atoms. 11
Figure 1.6: Complex ternary system SrO-TiO_2-Nb_2O_5 in air in the temperature range from 1275 to 1475 °C.....12
Figure 1.7: First three members of the Ruddlesden-Popper series, adapted from a paper from Rijnders.....13
Figure 1.8: Vacancy concentration depending on the oxygen partial pressure $P(O_2)$ and donor concentration.....14
Figure 1.9: Energy band structure of STNO depending on the Ti-Ti distance.....15
Figure 1.10: Density of states of 0%, 25% and 50% Nb-doped $SrTiO_3$ 15
Figure 1.11: Density of states of (a) 10%, (b) 5% deficient and (c) 0% Sr-deficient STNO (fully electronically compensated) 16
Figure 1.12: Carrier concentration (n) depending on $P(O_2)$ and donor content. 17
Figure 1.13: Thermoelectric properties of STNO single crystals and epitaxial films; (a) Electrical conductivity and Hall mobility (inset) of versus temperature, (b) carrier concentration, Hall mobility, Seebeck coefficient and carrier effective mass versus niobium doping concentration, (c) Seebeck coefficient versus temperature an calculated scattering parameter.....18
Figure 1.14: Thermal conductivity of STO ceramics depending on the grain size. Phonon mean free path of single crystal and polycrystalline ceramics depending on temperature.20
Figure 3.1: (a) High temperature tube furnace for sintering in air or argon and (b) Chamber furnace for sintering in argon/hydrogen or hydrogen atmosphere. 23
Figure 3.2: Binary phase diagram showing the NaCl-KCl eutectic at 657 °C, at the 1:1 molar ratio of the salts. The scheme on the right illustrates the crystal growth in a molten salts medium when the temperature is raised above the eutectic temperature of the salts. 24
Figure 4.1: STNO powders obtained by crushing the pellets, sintered in (a) air, (b) argon, (c) argon/hydrogen and (d) hydrogen atmosphere. 27
Figure 4.2: TGA curves of STNO samples initially sintered in different atmospheres (air-red, argon-green, argon/hydrogen-blue and hydrogen-black line). Weight increases are

proportional to degrees of oxidation due to incorporation of oxygen into the STNO oxygen deficient structures..... 28
Figure 4.3: Secondary electron images (SEI) and Back-scattered electron images (BEI) of STNO samples, sintered in different atmospheres; (a) air, (b) argon, (c) argon/hydrogen, and (d) hydrogen. Numbered dots are the EDXS measuring points of which the results are given in Table 4.2. 29
Figure 4.4: EDXS specters. Measuring points (1-7) are indicated in Figure 4.3. 30
Figure 4.5: XRD patterns of initial STNO powder (red line) and STNO powders sintered in different atmospheres: air (orange line), argon (green line), argon/hydrogen (blue line) and hydrogen (black line). 31
Figure 4.6: Unit cell dimensions of STNO samples, sintered in different atmospheres (different $P(O_2)$) obtained by the Rietveld refinement of the XRD patterns..... 32

List of Tables

Table 4.1: Mass change (in %) and calculated concentration of [Ti^{3+}] (in %) of STNO samples sintered in different atmospheres.....29
Table 4.2: Atomic elements concentration (± 0.2 %) from the EDXS measurements of STNO-air, STNO-Ar, STNO-Ar/H_2 and STNO-H_2. Atomic % of oxygen is calculated by the STO stoichiometry. Measuring points are indicated in the SEM image of Figure 4.3.30
Table 4.3: Unit cell dimensions based on the Rietveld analyses of XRD data of STNO, sintered in different atmospheres; a (cube edge length) and V (volume). 31
Table 6.1. Results of EDXS analysis of platelet crystals as a function of x in $Sr_3(Ti_{1-x}Nb_x)_2O_7$. 51

Abbreviations

PF	... Power factor
N-process	... Normal process
U-process	... Umklapp process
STO	... $SrTiO_3$
STNO	... Nb-doped $SrTiO_3$
YSZ	... Yttria-stabilized-zirconia
AO	... BaO, SrO or CaO
PGEC	... Phonon-glass electron-crystal
Seeded STNO	... STNO with Ruddlesden-Popper-type seeds
STNO;SrO	... Nb-doped $SrTiO_3$ with excess SrO
STNO;CaO	... Nb-doped $SrTiO_3$ with excess CaO
RP	... Ruddlesden-Popper
PIPS	... Precision Ion Polishing System
DLF	... Diamond-lapping film
HRTEM	... High resolution transmission electron microscopy
STEM	... Scanning transmission electron microscopy
DSC	... Differential scanning calorimeter
LFA	... Laser flash apparatus
TGA	... Thermogravimetric analysis
SEM	... Scanning electron microscopy
TEM	... Transmission electron microscopy
BEI	... Back-scattered electrons image
SEI	... Secondary electrons image
EDXS	... Energy-dispersive x-ray spectroscopy
STNO-air	... Nb-doped $SrTiO_3$ sintered in air
STNO-Ar	... Nb-doped $SrTiO_3$ sintered in argon
STNO-Ar/H_2	... Nb-doped $SrTiO_3$ sintered in argon-hydrogen
STNO-H_2	... Nb-doped $SrTiO_3$ sintered in hydrogen
MSS	... Molten salt synthesis
XRD	... X-ray powder diffraction
RPM	... Rates per minute

Symbols

ZT	... Thermoelectric figure of merit
$P(O_2)$	... Oxygen partial pressure
σ	... Electrical conductivity
κ	... Thermal conductivity
Π	... Peltier coefficient
κ_L	... Lattice thermal conductivity
κ_e	... Electrical thermal conductivity
S	... Seebeck coefficient
E	... Energy
J	... Current density
E_F	... Fermi energy
L	... Lorenz factor
T	... Temperature
k_{Th}	... Thomson coefficient
ΔT	... Temperature difference
∇T	... Temperature gradient
Q	... Heat energy
c	... Heat capacity
c_P	... Heat capacity at constant pressure
v	... Velocity of a particle
α	... Thermal diffusivity
ρ	... Density
E_f	... Electric field
V	... Thermoelectric voltage
m^*	... Charge carrier effective mass
h	... Planck constant
k_B	... Boltzmann constant
m_0	... True electron mass
e	... Electronic charge
n	... Charge carrier concentration
μ	... Charge carrier mobility
τ	... Mean free time between electron collisions
t	... Goldsmid structural tolerance factor
r_A	... Ionic radius of A
r_B	... Ionic radius of B
r_X	... Ionic radius of X
δ	... Oxygen deficiency
s	... Spacing between the tips
C	... Geometrical correction factor
M_{STNO}	... Molar mass of $Sr(Ti_{0.8}Nb_{0.2})O_3$
M_O	... Molar mass of oxygen

Δm ... Weight increase after oxidation in %

Chapter 1

Introduction

Increasing global concern for the environment raised new strategies in order to exploit the energy sources to their maximum and at the same time by preservation of the ecosystem. Alternative sources of energy, such as solar power, geothermal energy and waste heat, are gaining increased attention. More than half of the energy input in power plants and machines gets discarded as waste heat. This kind of waste can be turned into a favorable source of energy by implying thermoelectric generators, which are able to convert temperature gradient directly into electrical voltage. These considerably simple devices contain no moving parts, which prolongs their lifetime and operational reliability.

Nowadays, the development of thermoelectric devices is on one hand oriented towards improvement of the thermoelectric materials in terms of enhancing their thermoelectric figure of merit (ZT) and search for non-toxic materials with naturally abundant constituents and, on the other hand, optimizing the thermoelectric modules.

So far, most widely used materials in thermoelectric devices have been tellurium and antimony compounds. However, even though these kinds of materials are efficient thermoelectrics, some consist of heavy toxic elements which are, without being properly protected, not stable at elevated temperatures. To exploit waste heat from high temperature sources, such as car engines, power plants and furnaces, a great deal of research has been directed to semiconductor oxide-based materials, which are chemically and mechanically stable up to high temperatures (700 °C and more). Even though the power factors - PF (Seebeck coefficient squared and multiplied by electrical conductivity) of oxide-based single crystals and thin films showed promising values, their high thermal conductivity was found to be the main disadvantage. Another challenge is to obtain the promising properties of single crystals and thin films in polycrystalline bulk ceramics, which usually show inferior thermoelectric performance, due to specific characteristics of polycrystalline materials, which mostly arises from the grain boundaries (scattering, segregation of defects, energy filtering, etc.). Since the thermal conductivity in oxides is determined by the lattice phonons, an obvious approach would be to enhance the phonon scattering in the material, which would preferably lead to an increased overall thermoelectric figure of merit.

1.1 Thermoelectric Effect

Thermoelectric effect is a common term of three interrelated physical effects, which were independently discovered by three scientists: Thomas Johann Seebeck, Jean Peltier and William Thomson (Lord Kelvin). In 1826 Seebeck [1] reported that a magnetic field is produced by heating the junction between two different electrical conductors. It was

subsequently realized that an electric current is generated as well. The Seebeck effect is thus defined as an electromotive field (E_{emf}) generated in the presence of a temperature gradient (∇T) (Eq. 1.1).

$$E_{emf} = -S\nabla T \tag{1.1}$$

A decade later Peltier [2] found that an electric current (I) passing through a thermocouple produces heat which is now known as the Peltier effect (Eq. 1.2):

$$Q_P = \Pi I \tag{1.2}$$

where Q_P is the Peltier heat (power) and Π the Peltier coefficient.

The interdependency between the Seebeck and Peltier effect has been discovered by Thomson in 1951 by applying the thermodynamics theory [3] (Eq. 1.3):

$$\Pi = S \times T \tag{1.3}$$

where Π is the Peltier coefficient, S Seebeck coefficient and T temperature. He also predicted a third thermoelectric effect, which he had demonstrated experimentally later on, and is now known as the Thomson effect. It describes the evolution or absorption of heat when a potential difference is applied to a material which is exposed to temperature difference (Eq. 1.4):

$$Q = k_{Th} J \nabla T \tag{1.4}$$

where k_{Th} is the Thomson coefficient, J current density and ∇T thermal gradient.

The thermoelectric phenomenon is exploited either by thermoelectric generators or thermoelectric refrigerators. In both cases, the thermoelectric module is made of numerous thermocouples which are electrically connected in series and thermally in parallel (Figure 1.1). Each couple consists of two types of material: p-type, in which charge carriers are positively charged holes, and n-type material in which charge carriers are negatively charged electrons. In refrigerators, the current is added to the module which gives a rise to the Peltier effect that appears as heating or cooling of the device. In power generators, however, a temperature gradient is introduced which enables the electrons to pass from one side of the material to another resulting in an electrical voltage by means of the Seebeck effect.

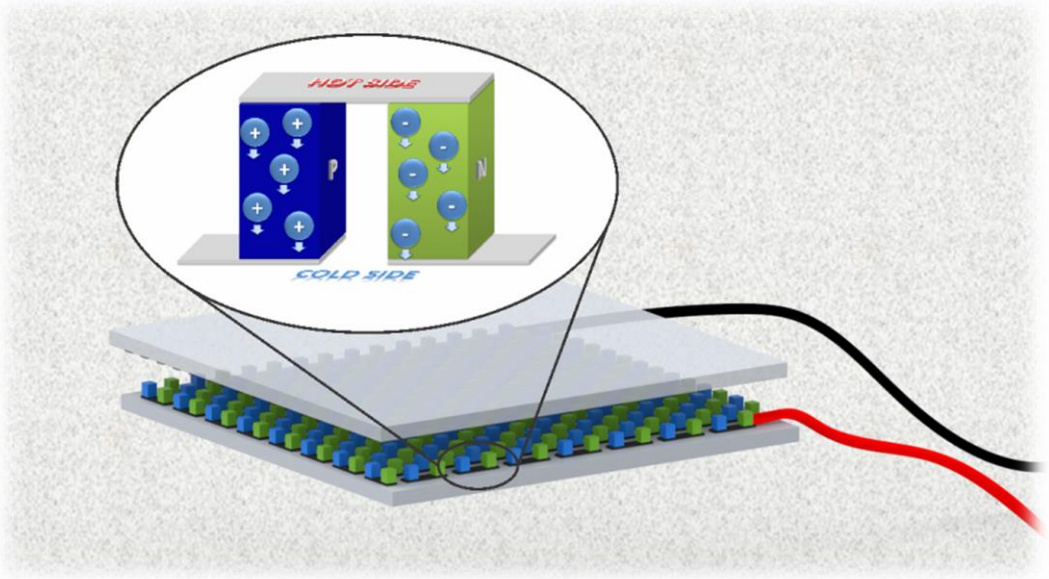


Figure 1.1: Schematic presentation of thermoelectric module and a single thermocouple, (enlarged in the inset) consisting of two types of material: p-type and n-type. Thermoelectric module model made by Luka Suhadolnik.

A good thermoelectric material should basically possess a large Seebeck coefficient, which is a measure of the magnitude of the induced thermoelectric voltage. On the other hand, thermal conductivity and electrical resistivity ought to be low to retain the temperature difference in the material and to ensure high electron mobility, respectively. Nevertheless, the electron and heat transport properties are interdependent, so optimizing one parameter individually leads to deterioration of another which, in the end, results in unchanged or even lower thermoelectric performance. For example, metals with a high electrical conductivity and low Seebeck coefficient, which results in a low power factor, are not appropriate to be used as thermoelectrics. On the other hand, semiconducting materials with a low thermal conductivity suffer from low power factor due to poor electrical conductivity, even though their Seebeck coefficient is sufficient. Therefore, proper ratio has to be found between these conflicting intrinsic properties of each material individually in order to obtain a thermoelectric material with satisfactory properties [4].

1.1.1 Electron and Heat Transport in Solids

1.1.1.1 Electron Transport

Charge carriers which contribute to the electron transport in solids can be negative – electrons, or positive – electron holes. The "hole" refers to a positive charged position due to a lack of an electron. Energies of electrons of a solid lie inside contiunuous energy bands that are separated by forbidden regions (energy band gaps). Energy of the band gap between the filled valence band and partly occupied conduction band determines the electron tranport behavior of a material. In addition, only electrons with partially filled states are able to move to other energy bands while the completely filled lower bands do not contribute to the transport in solids [5]. Based on the position of the Fermi level and

the energy of the band gap, the material behavior is either highly conductive, semi conductive or insulating (Figure 1.2).

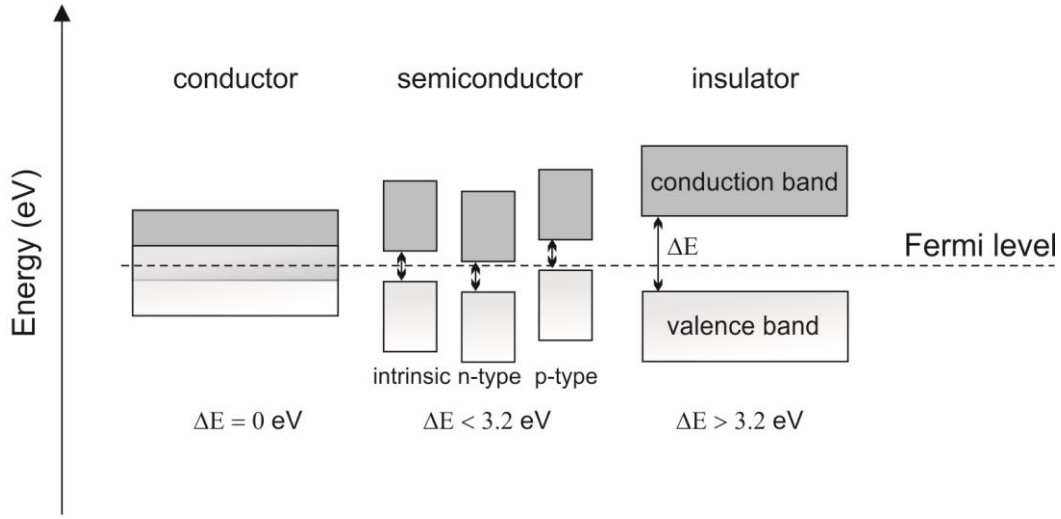


Figure 1.2: Energy band diagrams of conductors, semiconductors or insulators. Based on the positions of the valence and conduction band with the relation to the Fermi level, semiconductor can be intrinsic, n-type or p-type.

Thereby, when the valence and conduction band overlap (E = 0) and the Fermi level enters the conduction band, the material is a good conductor. When the energy between the bands is lower than 3.2 eV and in addition the Fermi level is close to the conduction band, the material is a semiconductor. When a sufficient energy is provided to a semiconductor, electrons near the Fermi level from the valence band are able to overcome the band gap energy and move into the conduction band. Three possible positions of the valence and conduction band in relation to the Fermi level can occur. When the bands are equally distant from the Fermi level, the material is an intrinsic semiconductor. Moreover, when the conduction band is closer to the Fermi level, the semiconductor is n-type, while in the case of the valence band being closer to the Fermi level, the semiconductor is p-type. Finally, insulators are materials with an energy band gap greater than 3.2 eV. The Fermi level of insulators lies well within the band gap, so that the electrons from the valence band cannot enter the conduction band, even when a significant energy is provided.

1.1.1.2 Heat Transport

The heat in a solid can be transmitted through several excitations, however, the majority of the heat transport is dominated by electrical carriers (electrons or holes) and lattice vibrations. Due to interaction forces, the atoms in a solid are not static but rather in a vibrational motion about their equilibrium positions in the crystal lattice [6]. Such vibrational wave packets, also commonly called phonons, were first described by Peierls [7] in 1929. By neglecting the insubstantial excitations, the total thermal conductivity (κ) can be written as a sum of the lattice (κ_L) and the electrons/holes (κ_e) contributions, seen in Eq. (1.5).

$$\kappa = \kappa_L + \kappa_e \tag{1.5}$$

The quantity of the lattice and electronic contribution depends on the materials energy band structure and the charge carrier density. In conductors, the majority of the heat is transported by the charge carriers due to high charge carrier density, while in semiconductors and insulators the heat transport is dominated by phonons [6]. A good estimation of the electronic contribution to the total thermal conductivity can be calculated using the electrical conductivity by the Franz-Wiedemann law [8], presented in Eq. (1.6).

$$\kappa_e = LT\sigma \tag{1.6}$$

where L is the Lorenz factor (2.45×10^{-8} WΩ/K^2), T is temperature and σ electrical conductivity.

Fourier's law on thermal conductivity describes the heat energy (Q) generated in the presence of a thermal gradient (∇T), seen in Eq. (1.7).

$$\kappa = \frac{Q}{\nabla \mathrm{T}} \tag{1.7}$$

In the view of kinetic theory, a particle with a defined heat capacity c travels with a velocity (v) in the presence of a temperature gradient (∇T), thus the energy (E) changes in a defined time (t), as written in Eq. (1.8).

$$\frac{\partial E}{\partial t} = cv\nabla T \tag{1.8}$$

Material's heat capacity c is defined as a ratio of the amount of heat energy (∂Q) transferred to an object and the resulting increase in temperature (dT) of the material (Eq. 1.9).

$$c\ (T) = \frac{\partial Q}{dT} \tag{1.9}$$

Thermal conductivity of a material can be measured directly or calculated from materials constant pressure heat capacity – c_p, thermal diffusivity – α and density – ρ (Eq. 1.10). Thermal diffusivity describes how quickly a material reacts to a change in temperature.

$$\kappa = c_p\ \alpha\ \rho \tag{1.10}$$

1.1.2 Electron and Phonon Scattering

In a polycrystalline solid, charge carriers and phonons cannot roam freely through crystal but rather scatter due to different interactions, lattice defects, other phonons, other electrons, grain boundaries, surfaces or impurities.

Electron collisions can be either elastic or inelastic. Energy of the electron is maintained if it is scattered elastically, while it is lowered due to inelastic scattering. The transport of electrons can be disturbed by either other electrons' Coulomb forces or by phonons [6]. The phonons can interact with other phonons, which is called the phonon-phonon scattering. Phonons can interact in two temperature-dependent processes: Normal (N) or Umklapp (U). In N-process, the phonon momentum is preserved, which has negligible effect on the lattice thermal conductivity. In contrary, the U-process changes the momentum of two phonons colliding which increases the phonon scattering in the lattice significantly. Phonons can scatter from electrons, which is referred to as the phonon-

electron scattering. Another scattering process can occur due to mass-difference between the atoms in the crystal lattice, while the grain boundary scattering becomes relevant for low-dimensional nanostructures. Which mechanism of scattering is present in the material is strongly dependent on the temperature. For example, scattering of electrons on impurities is stronger at lower temperatures. On the other hand, temperature-dependent electron transport behavior depends on the type of material. In conductors, there is a great number of charge carriers. By increasing the temperature, the electrons start to move more rapidly and consequently collide more frequently, which results in higher electrical resistance. In a semiconductor, however, the electrical transport is promoted by elevated temperatures, since more electrons can overcome the narrow energy band gap and participate in the electron transport when there is additional energy added. Nevertheless, the phonon scattering increases as the temperature rises due to lower phonon mean free path [9], [10]. At low temperatures, the phonons are scattered mostly by grain boundaries. At intermediate temperatures, defect scattering starts to predominate, while at high temperatures the U-processes take over the scattering.

1.1.3 Electrical Resistivity and Conductivity

Electrical resistivity (ρ) of a material is an intrinsic property of a material that describes to what extent the material opposes the electric current (I) to flow freely in the presence of an electric field (E_f). Reciprocally, electrical conductivity (σ) is the ability of a material to conduct electricity (Eq. 1.11).

$$\rho = \frac{E_f}{I} = \frac{1}{\sigma} \tag{1.11}$$

Electrical conductivity depends on the intrinsic properties of a material and also on the temperature, which is connected to temperature-dependent electron mobility. For example, metals are good conductors at low temperature, while at higher temperatures their resistivity increases due to an increased number of collisions between many mobile carriers. On the other hand, semiconductors tend to exhibit low electrical conductivity at low temperatures due to a small number of charge carriers. At elevated temperatures, the number of charged carriers increases giving rise to the electrical conductivity. Electrical conductivity depends on the concentration of the dominant charge carriers (n) and on the temperature-dependent mobility (μ_n) [11], described in Eq. (1.12).

$$\sigma = e\, n\, \mu_n(T) \tag{1.12}$$

where e is the electronic charge and T temperature.

1.1.4 Seebeck Coefficient

When a temperature gradient is applied to a thermoelectric material, the charged carriers diffuse from the hot side to the cold side of the material. This way, an electrical potential is built and it results in an induced thermoelectric voltage [12]. Seebeck coefficient (S) is therefore defined as a measure of the magnitude of an induced thermoelectric voltage (ΔV) in response to a temperature difference (ΔT) across the material – Eq. (1.13).

$$S = -\frac{\Delta V}{\Delta T} \tag{1.13}$$

Absolute value of the Seebeck coefficient is high once one of the carriers, either positive or negative, prevails in the material. In addition, the sign of the measured Seebeck

coefficient indicates which charge carriers dominate. Seebeck coefficient of a bulk semiconductor depends i.a. on the carrier concentration (n) and charge carrier effective mass (m^*), as seen in the expression of Eq (1.14).

$$S = \frac{8m^*\pi^2 k_B^2}{3eh^2} T \left(\frac{\pi}{3n}\right)^{\frac{2}{3}} \tag{1.14}$$

where e is the electronic charge, h Planck constant and k_B Boltzmann constant.

1.1.5 Thermoelectric Figure of Merit

A good thermoelectric material should possess a low thermal conductivity (κ) to maintain a temperature gradient, high Seebeck coefficient (S), and electrical conductivity (σ) to ensure a high thermoelectrical voltage output. These three parameters are combined in a dimensionless temperature-dependent (T) thermoelectric figure of merit (ZT) – Eq (1.15).

$$ZT = \frac{S^2\sigma}{\kappa} T \tag{1.15}$$

Materials with a ZT higher or close to 1 are considered to be suitable for practical applications. All three main thermoelectric parameters are connected through the carrier concentration (n). Therefore, finding the optimal carrier concentration for a thermoelectric material is a key to enhance its figure of merit. Nevertheless, the requirements of thermoelectric parameters are conflicting; to ensure a high Seebeck coefficient and a low thermal conductivity the carrier concentration should be low, whereas a high carrier concentration is needed for a high electrical conductivity. The electrical conductivity is related to carrier concentration (n) through the carrier mobility (μ) – Eq. (1.16).

$$\sigma = ne\mu = \frac{ne^2\tau}{m^*} \tag{1.16}$$

where e is the carrier charge, τ is the mean free time between colisions, and m^* is the carrier effective mass. The upper part of the ZT equation, Seebeck coefficient squared and multiplied by electrical conductivity ($S^2\sigma$), is often referred to as power factor (PF). For a sufficient ZT value, power factor ought to be as high as possible. However, these two parameters are inversely proportional, which is why complex approaches must be taken to achieve a so-called trade-off between Seebeck coefficient and electrical conductivity, that is to enhance one parameter without lowering the other at the same time [13]. In addition to the carrier concentration, finding optimal m^* is another challenge to ensure a high power factor, since high values of m^* result in a large S but small σ, due to lower velocities of the heavy carriers leading to a low mobility [4]. Thus, a balance between high m^* and efficient mobility has to be achieved.

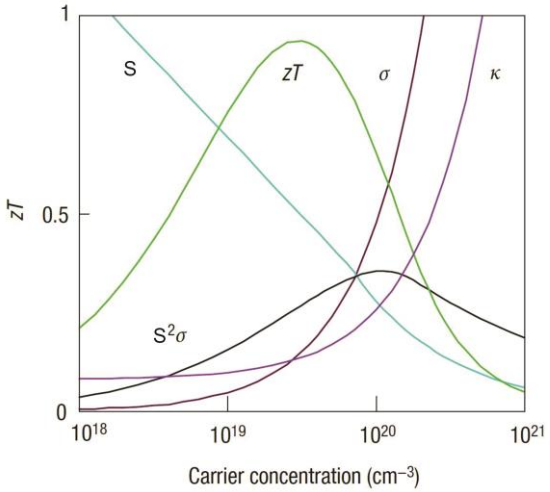


Figure 1.3: Thermoelectric parameters; Seebeck coefficient S, electrical conductivity σ and thermal conductivity κ and power factor $S^2\sigma$ and figure of merit ZT depending on the carrier concentration of Bi_2Te_3 [14], [4].

Figure 1.3 shows thermoelectric parameters and ZT depending on the carrier concentration in the case of Bi_2Te_3, a graph taken from the paper of Snyder and Toberer [4] based on the empirical data from Rowe and Min [14]. It can be noticed that individual thermoelectric parameters either linearly increase or lineraly decrease with carrier concentration. However there is a maximum peak for the power factor ($S^2\sigma$) and ZT between carrier concentrations of 10^{19} and 10^{20} cm^{-3}.

1.2 High-Temperature Oxide Thermoelectrics

Applicability of each thermoelectric material is restricted to a certain temperature range, either due to temperature dependent optimal performance or due to limited chemical stability. Metallic compounds, such as Bi_2Te_3 [15], $CoSb_3$ [16], and Si-Ge alloys [17], are efficient around room temperature, whereas at higher temperatures their properties are deteriorating. Therefore, for harvesting waste heat produced as a side effect of engine vehicles and furnaces operation, materials which are efficient and chemically stable at high temperatures are required. Thus, silicide [18] and oxide [19] compounds are becoming attractive due to their high temperature chemical stability and progressive thermoelectric performance as the temperature difference produced in the material rises. Additional advantage of oxides and silicides over heavy-element based materials is the relative abundancy of their constituents and non-toxicity which has been nicely displayed by He et al. [20] (Figure 1.4).

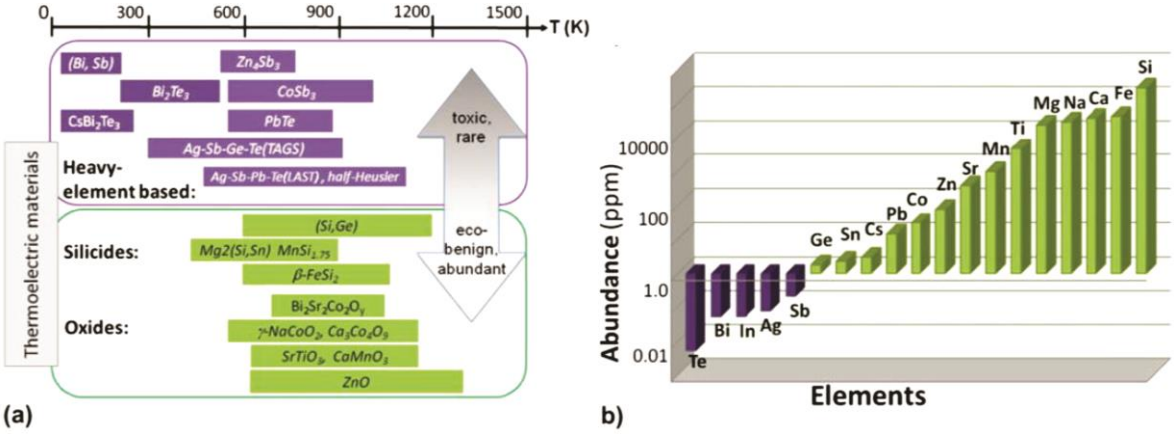


Figure 1.4: Review of thermoelectric materials, based on their optimal operating temperature and toxicity (a) and abundancy of materials constituents in the Earth's crust (b) adapted from He et al. [20].

The attention towards oxide-based materials was attracted at the end of the previous century when several scientists reported promising thermoelectric properties of these kinds of materials. In 1997 Terasaki et al. [21] recognized a low thermal conductivity coupled with a high power factor of p-type $NaCo_2O_4$ single crystals, comparable with Bi_2Te_3. Despite its promising thermoelectric characteristics, it was later realized that this kind of material suffers from instability due to its hygroscopic nature [22] and chemical deterioration at elevated temperatures [23]. In this sense, another cobaltate - $Ca_3Co_4O_9$ was found to be a more adequate candidate for a future p-type thermoelectrics. ZT of $Ca_3Co_4O_9$-based single crystals reaches as much as 0.87 at 973 K [24]; however the values of polycrystalline bulk analogues are much lower, about 0.2 at 973 K [25]. Generally accepted approaches to improve the figure of merit in the $Ca_3Co_4O_9$ system are either to align the plate-like grains or to substitute Ca with heavier atoms. Some relative enhancement of ZT was observed in a highly textured ceramics as compared to a lower degree of alignment, reported by Itahara et al. [26], while a high ZT of 0.5 at 1000 K was obtained in an Ag-substituted $Ca_3Co_4O_9$. It should be mentioned that ZT values of textured ceramics can be misleading, if the measurements of individual thermoelectric parameters are performed as a combination of in-plane and out-of-plane measurements, which can result in overestimated values.

While the p-type promising thermoelectric oxides are mostly limited to cobalt-based oxides, there are quite a few n-type oxide based candidates. In 1995, Ohtaki et al. [27] studied the suitability of $CaMnO_3$, doped with various elements as a thermoelectric material. The highest ZT was measured in the Bi-doped sample; 0.085 at 1173 K. A significant enhancement of a ZT in $CaMnO_3$, doped with 2% of Nb, reaching 0.32 at 1060 K, was achieved by employing the *chimie douce* synthesis technique, which resulted in a nanograined microstructure and consequently a severely reduced thermal conductivity [28]. ZnO is another prospective n-type thermoelectrics. In 1996 [29] Al-doped ZnO exhibited a high PF and a calculated ZT of 0.24 at 1273 K. The authors suggested that even higher values could be obtained by lowering the relatively high thermal conductivity which boosted a number of studies of the ZnO-system [30]–[32]. Up to date the highest ZT of 0.47 at 1000 K in the ZnO system was achieved by Ohtaki at al. [33] in 2009, when ZnO was doped with Al and Ga. A study by Moos et al. [34] recognized a high Seebeck coefficient in La-doped $SrTiO_3$, which initiated numerous studies in this kind of material. Wunderlich et al. [35] subsequently found that Nb is a more appropriate choice for doping

in comparison to La, since Nb-doped $SrTiO_3$ has a higher carrier effective mass in comparison to La-doped $SrTiO_3$ which could lead to a high Seebeck coefficient. In the studies that followed, attempts to enhance figure of merit involved either experimenting with different dopants on A-site [36]–[38], B-site [39] or both [40], or microstructural modifications, for example forming Ruddlesden-Popper phases [41] in order to enhance the phonon scattering. However, in spite of all the efforts to improve the thermoelectric properties, the best reported ZT for this system remains in the range of other bulk n-type oxides; 0.37 at 1000 K [42], [43] for 20% Nb doped $SrTiO_3$. In the following chapters, Nb-doped $SrTiO_3$ is presented in detail from a view of its physical properties, microstructural features and thermoelectric characteristics reported up to date.

1.2.1 Nb-Doped $SrTiO_3$ Thermoelectric Material

1.2.1.1 Crystal Structure of $SrTiO_3$ and Nb-Doped $SrTiO_3$

$SrTiO_3$ (STO) exhibits a perovskite stucture with a body-centered cubic unit cell (Pm3m). The corner positions are occupied by strontium ions, the edge centers by oxygen ions, and the center by the titanium ion (Figure 1.5). The titanium and oxide ions form corner sharing TiO_6 octahedra, while strontium ions occupy the interstitials of the octahedra. This results in a 12-fold oxygen coordination of strontium and 6-fold oxygen coordination of the titanium. The cubic structure of STO is stable down to temperature of 105 K where it undergoes a phase transition into tetragonal structure [44]. Perovskite structure accomodates considerably high amounts of doping, while retaining the basic stucture. Goldschmidt [45] found that the stability of a perovkite stucture - ABX_3 is determined by the size ratio of the A and B cation and anion X which he described by the structural tolerance factor t (Eq. 1.17).

$$t = \frac{r_A + r_X}{\sqrt{2}(r_B + r_X)} \tag{1.17}$$

where r_A is the radius of A, r_B radius of B and r_X radius of X.

Accordingly, when t equals 1, the structure is cubic. In the range where the t lies between 0.9 and 1, the perovskite structure is distorted cubic. When t values are higher than 1, the structure is hexagonal, while at smaller t values the structure is either othorombic or rhombohedral. By doping the A-sites with e.g. a slightly smaller ion, the structure balances the ionic size difference by tilting the BX_6 octahedra without changing the basic perovskite stack. STO is one of the most stable perovskite structures, since it exhibits a tolerance factor of 0.98.

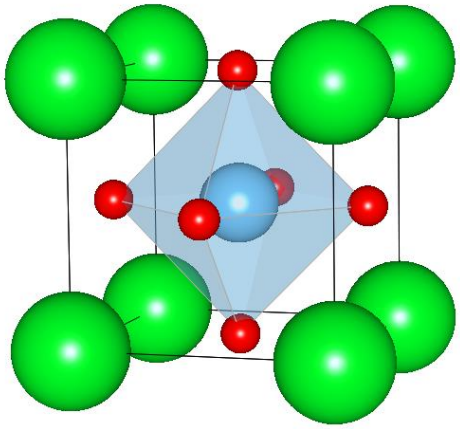


Figure 1.5: Unit cell of $SrTiO_3$ and TiO_6 octahedra, formed by the oxygen atoms. Green spheres are the strontium atoms, blue is the titanium and red are the oxygen atoms (model made by VESTA).

Frequently, STO is doped with donor or acceptor elements in order to improve the electrical conductivity of the material. Since Nb-doped STO (STNO) is the topic of this thesis, it will be structurally defined hereinafter. By doping STO with Nb, the dopant takes the titanium positions and therefore the crystal lattice constant expands, due to larger radius of Nb^{5+} (0.064 nm) in comparison with Ti^{4+} (0.061 nm) and also due to reduction of Ti^{4+}(0.061 nm) into Ti^{3+} (0.067 nm) [46], [47], [11]. Consequently, unit cell dimensions depend on the doping concentration and/or on level of reduction. The STO structure can accommodate different amounts of dopant niobium in a form of STNO solid solution, depending on the surrounding $P(O_2)$. Once the solubility of the dopant is exceeded, secondary phases form in addition to the solid solution. $SrO\text{-}TiO_2\text{-}Nb_2O_5$ is a complex ternary system (Figure 1.6), where numerous phase compounds exist [48]. Exceeding the solid solubility of Nb in STNO can thus result in several possible secondary phases.

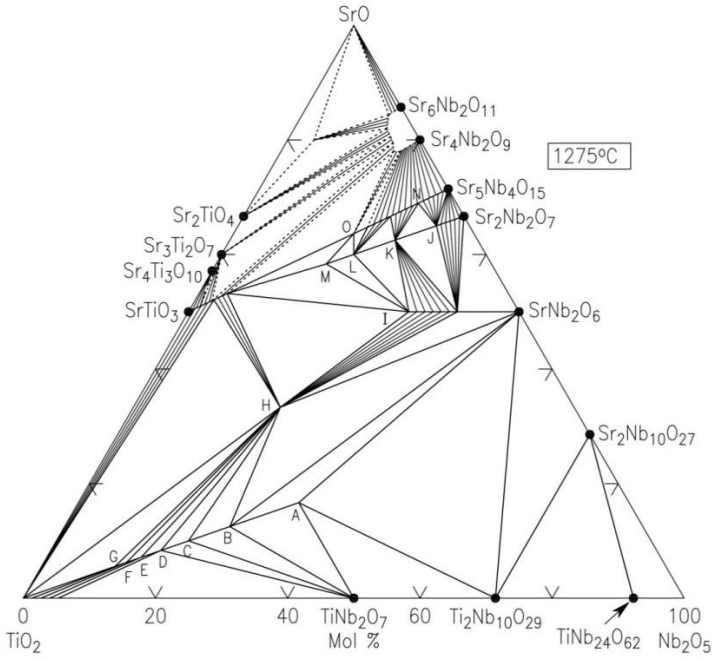


Figure 1.6: Complex ternary system SrO-TiO_2-Nb_2O_5 in air in the temperature range from 1275 to 1475 °C [48].

Up to 0.2 mol% of excess AO (A = Ba, Sr, Ca) in STO is found to be accomodated in a form of solid-solution [49]. By exceeding this value, the excess AO is accomodated by formation of AO × n$SrTiO_3$ (n > 1) homologous compounds (Figure 1.7), initially described by Ruddlesden and Popper [50]. N represents the number of perovskite blocks interleaved by a single rock-salt-type AO layer. The stacking/ordering of the AO planar faults in these structures occurs along the [001] perovskite direction. The AO rock-salt structure causes the shift of perovskite unit cells across the AO fault by half of the perovskite unit cell in the [110] direction, i.e. ½ [110]. RP-phases form a tetragonal body-centered unit cell.

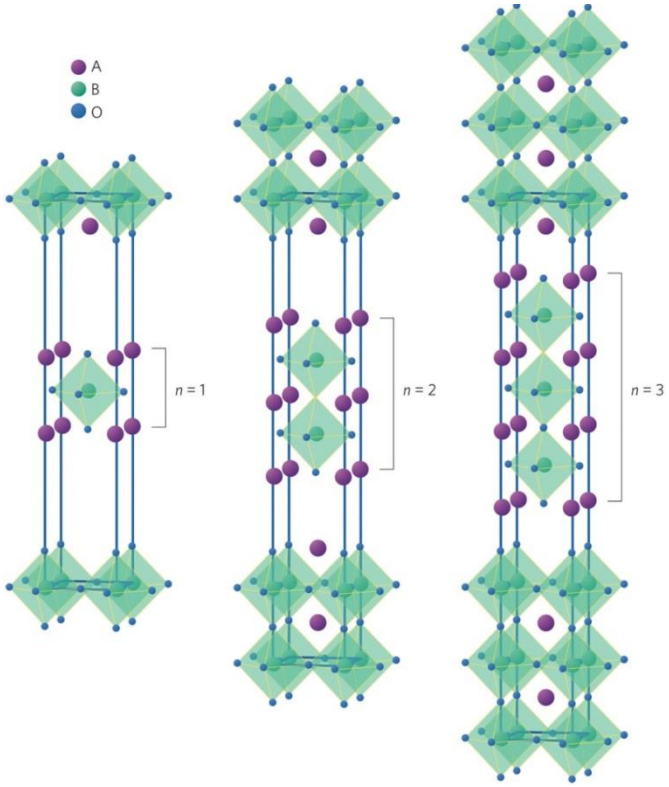


Figure 1.7: First three members of the Ruddlesden-Popper series, adapted from a paper from Rijnders [51].

1.2.1.2 Defect Chemistry of Nb-Doped $SrTiO_3$

Defect chemistry of STNO can be described according to defect model of donor-doped STO proposed by Blennow et al. [11] and Moos and Härdtl [52] by using the Kroeger-Vink [53] notations. Nb^{5+} occupies the Ti^{4+} positions of STO and brings an extra electron into the structure. The electroneutrality is obtained by different compensation mechanisms depending on the surrounding atmosphere. High oxygen partial pressure - $P(O_2)$ leads to ionic compensation, while low $P(O_2)$ favors electronic compensation. Ionic compensation referes to formation of strontium vacancies and thus the incorporation reaction can be written as (Eq. 1.18):

$$SrO + (1\text{-}x)TiO_2 + x/2\ Nb_2O_5 \rightarrow (1\text{-}x/2)Sr_{Sr}^{x} + x/2V_{Sr}^{''} + (1\text{-}x)Ti_{Ti}^{x} + xNb_{Ti}^{\bullet} + 3O_{O}^{x} + x/2SrO \quad (1.18)$$

Reaction in Eq. (1.18) suggests that an ideal perovskite ratio of Sr/Ti = 1 should result in second phase SrO upon calcination in oxidizing atmosphere due to formation of strontium vacancies. Eventual loss of the second phase should be achieved at low $P(O_2)$ (1.19), where strontium vacancies can be neglected:

$$V_{Sr}^{''} + SrO \leftrightarrow ySr_{Sr}^{x} + y/2O2 + 2ye' \quad (1.19)$$

Extra electrons are coupled with Ti^{3+}/Ti^{4+} redox couples, thus associated with Ti^{3+} sites in the perovskite structure. Similarly, it could be expected that niobium is reduced from Nb^{5+} into Nb^{4+} as well, however it was shown experimentally that only Ti^{4+} is reduced into Ti^{3+} and that the niobium stays in the pentavalent state even after sintering STNO in highly reducing atmospheres [11], [54]. The cation compensation is shifted to electronic compensation at very low $P(O_2)$, by formation of oxygen vacancies. In such $P(O_2)$ conditions these vacancies are the predominant defects and all other defects can be neglected. At higher temperatures (> 1273 K), the oxygen vacancies are twofold positively ionized by emitting two electrons into the conduction band (Eq. 1.20),

$$O_O^x \leftrightarrow V_O^{\bullet\bullet} + 2e' + (1/2)\ O_2 \quad (1.20)$$

while at lower temperatures (< 873 K) they are singly ionized [52] (Eq. 1.21).

$$V_O^{\bullet\bullet} + e' \leftrightarrow V_O^{\bullet} \quad (1.21)$$

At high $P(O_2)$ the dopant concentration determines the number of defects formed, while at low $P(O_2)$, the concentration of oxygen vacancies does not depend on the donor doping level. Relation between $P(O_2)$, donor concentration and total vacancy concentration is represented in Figure 1.8, a graph from Chung et al. [55]. In a hydrogen atmosphere, additional donors in the form of hydroxide ions may be formed during processing [56], [57], according to Eq (1.22):

$$O_O^x + (1/2)\ H_2 \leftrightarrow (OH)_O^{\bullet} + e \quad (1.22)$$

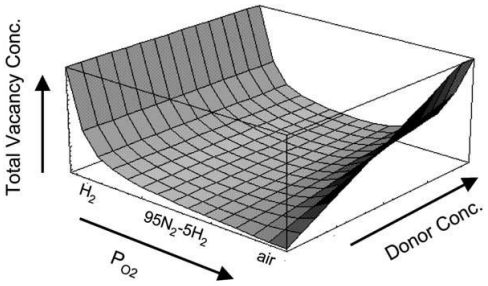


Figure 1.8: Vacancy concentration depending on the oxygen partial pressure $P(O_2)$ and donor concentration [55].

1.2.1.3 Energy Band Structure of $SrTiO_3$ and Nb-Doped $SrTiO_3$

Theoretical calculations of the electronic structure of undoped STO suggest that the top of the valance band is made of predominantely O 2p states and the bottom of conduction band of Ti 3d states [58]. In addition, the width of the conduction band is directly related to the distance between neighbouring Ti atoms (Figure 1.9) [59].

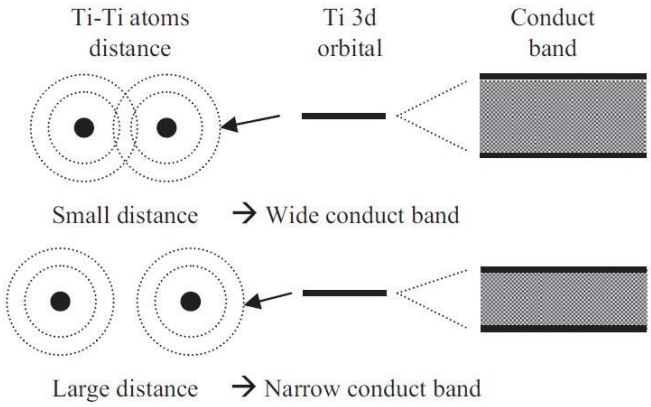


Figure 1.9: Energy band structure of STNO depending on the Ti-Ti distance [59].

The main electronic properties of STO are dominated by the network of corner-shared TiO_6 octahedra, due to the Ti 3d - O 2p interaction. Figure 1.10 shows the density of states of undoped, 20%-Nb doped and 50% Nb-doped STO. Undoped STO is an insulator with an experimentaly determined band gap between occupied O 2p and unnocupied Ti 3d states of 3.2 eV at room temperature (the theoretical value is 1.85 eV). By niobium doping, the valance band is distorted and the Fermi level enters the conduction band, seen in Figure 1.10 for 25% Nb-doped STO [60]. Reduction of Ti^{4+} into Ti^{3+} introduces electrons into Ti 3d bands which leads to very high electrical conductivity [61]. Consequently, the band structure of heavily Nb-doped STO (at > 10% Nb) shows a metallic behavior [46], [60]. By increasing the Nb concentration (50% Nb-doped STO), the disturbance of the valance band is weakened by the free carriers screening effect and, in addition, the edge of the conduction band shifts to lower energy region. Therefore, in STNO, free carriers concentration does not show linear behavior by increasing the Nb concentration in the whole range [46], [60].

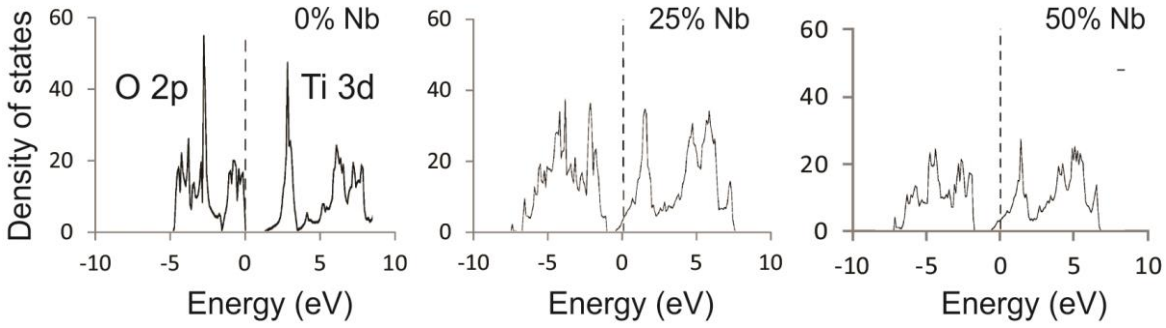


Figure 1.10: Density of states of 0%, 25% and 50% Nb-doped $SrTiO_3$ [60].

The energy band structure depends also on the $P(O_2)$ and consequently on the compensation mechanism (Figure 1.11) [62]. When extra charges are compensated by the

formation of strontium vacancies ($Sr_{0.9}Ti_{0.8}Nb_{0.2}O_3$) STNO exhibits an insulating behavior with a 1.80 eV band gap. When the Nb-doping is partially compensated by Sr-vacancies, the Fermi energy shifts into the conduction band. Finally, fully electronically compensated STNO with no strontium vacancies ($SrTi_{0.8}Nb_{0.2}O_{3-\delta}$) contributes even more electrons into the conduction band and therefore the material shows a metallic behavior.

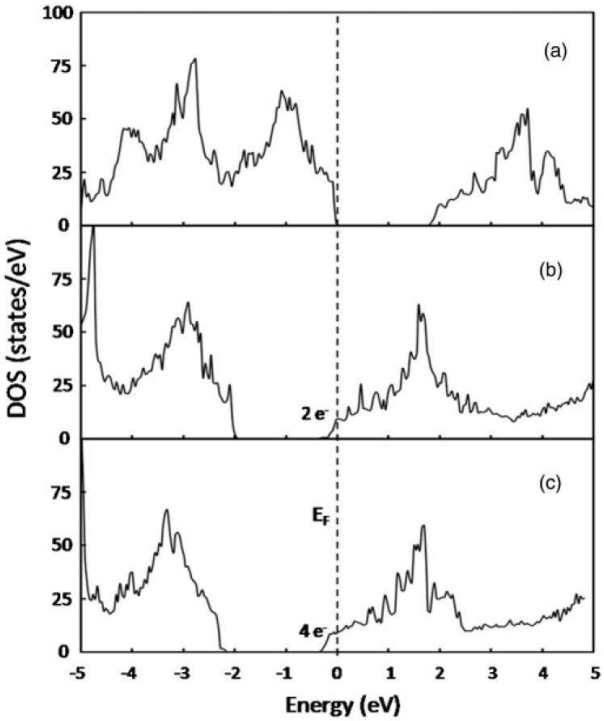


Figure 1.11: Density of states of (a) 10%, (b) 5% deficient and (c) 0% Sr-deficient STNO (fully electronically compensated) [62].

1.2.1.4 Carrier Concentration of Nb-Doped $SrTiO_3$

Charged defects resulting from donor doping determine the charge carrier concentration (n) of STNO. Which defects predominate in STNO is highly dependent on the $P(O_2)$. Schematic plot adapted from Blennow et al. [11] in Figure 1.12 shows the relations between $P(O_2)$, donor content and carrier concentration.

At high $P(O_2)$ strontium vacancies are the predominant charged defect which results in a low carrier concentration and thus the entire carrier concentration is basically determined by the concentration of strontium vacancies. At intermediate $P(O_2)$ the carrier concentration is determined by the donor concentration. At a certain intermediate range of $P(O_2)$ a »plateau region« is present where the carrier concentration is constant. Increasing the donor content results in a left-hand shift and widening of the plateau region. Consequently, highly doped STNO has to be processed in strongly reducing atmospheres in order to achieve a fully electronic compensation.

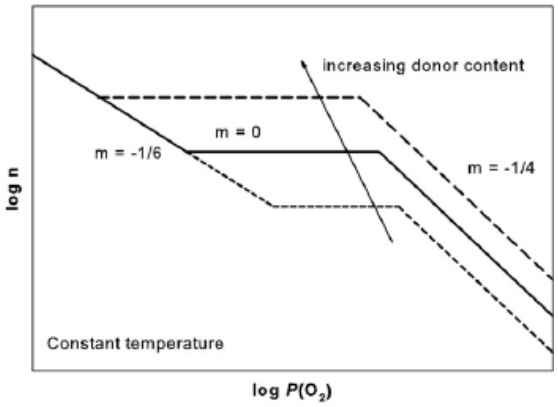


Figure 1.12: Carrier concentration (n) depending on $P(O_2)$ and donor content [11].

By decreasing the temperature, the "pleteau region" shifts to the left and widens, which leads to higher electrical conductivity due to higher electron mobility at lower temperatures. At low $P(O_2)$, however, there is another shift in the defect structure of STNO. The oxygen vacancies start to predominate over the donor concentration and all other defects can be neglected. Thus, at very high $P(O_2)$, the carrier concentration depends only on the concentration of oxygen vacancies.

1.2.1.5 Thermoelectric Properties of Nb-Doped $SrTiO_3$

Rewiev of STNO thermoelectric properties based on different studies is given in this chapter. Ohta et al. [63] studied electrical conductivity, Hall mobility and carrier concentration versus temperature of STNO single crystals (Figure 1.13 a). It can be seen from the graph in Figure 1.13 that the carrier concentration is basically temperature independent, whereas the mobility decreases with temperature. Consequently, decreased electrical conductivity of donor doped STO with temperature can be connected to lower mobility of charge carriers at high temperatures. Graphs in Figure 1.13 b present carrier concentration, Hall mobility, Seebeck coefficient and carrier effective mass versus Nb doping concentration of STNO epitaxial films from a study of Ohta et al. [64]. Carrier concentration was found to be proportional to doping concentration, since it increased with higher doping concentrations. On the other hand, the Hall mobility decreased slightly with higher doping concentration. This was explained by enhancement of STNO's carrier effective mass as the Nb concentration is increased, which was on the other hand also the reason for the increased Seebeck coefficient.

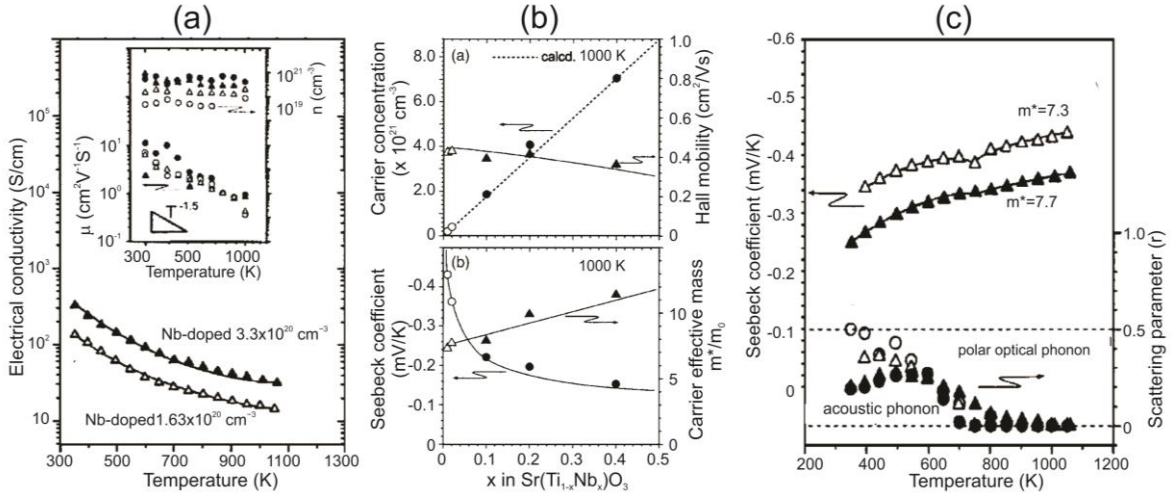


Figure 1.13: Thermoelectric properties of STNO single crystals [63] and epitaxial films [64]; (a) Electrical conductivity and Hall mobility (inset) of versus temperature, (b) carrier concentration, Hall mobility, Seebeck coefficient and carrier effective mass versus niobium doping concentration, (c) Seebeck coefficient versus temperature and calculated scattering parameter.

Irvine et al. [65] studied electrical transport properties of STNO with respect to different concentrations of Nb and various $P(O_2)$. They found that at low $P(O_2)$ the electrical conductivity of STNO initially increased as the Nb concentration increased, however at $x > 0.25$ it decreased. Increasing the $P(O_2)$ led to a decrease of the electrical conductivity. A rapid decrease of electrical conductivity was observed in the lightly doped samples, while the heavily doped samples showed a slow decrease in conductivity. This phenomenon was explained in terms of Nb stabilizing the Ti^{3+} generated by reduction. The study concluded that minor reduction of $STNO_{3-\delta}$ ($\delta \sim 0.05$, which corresponds to ~ 0.1 Ti^{3+}) produces a large increase in the electrical conductivity. Tinh and Tsuji [39] reported on thermoelectric properties of Sr-deficient polycrystalline STO, synthesized in forming gas (H_2/N_2), and concluded that the electrical conductivity increased with higher Nb concentration up to 20% Nb and then decreased. This is in agreement with the findings of Irvine [65].

Frye et al. [66] measured the electrical conductivity of STO with respect to the samples annealing temperature. They found that the conductivity increased as the annealing temperature of the samples was higher. In several studies a change from semiconducting to metallic behavior of the electrical conductivity of polycrystalline bulk STNO in the temperature range 150 – 300 °C was observed [11], [39], [42], [47]. On the other hand, heavily doped STNO single crystals [64] and STNO thin films [46] showed metallic behavior in the whole temperature range and no such temperature-dependent change was observed. This implies that in the low temperature range, the grain boundaries influence the electrical transport by decreasing the electron mobility. A study of Yamamoto [67] suggested that accumulation of point defects in the vicinity of otherwise "clean" grain boundaries represents a potential barrier for electrons if they are negatively charged up. Another cause for the negative charge distribution at grain boundaries, sintered in hydrogen, may be trapped electrons. Chung et al. [54] observed negatively charged Nb segregation on the grain boundaries in highly reducing atmospheres, whereas there was no such segregation in the grain boundaries in STNO synthesized in air. Frye at al. [66] realized that the resistivity of the samples decreases with increased reduction, yet free carrier densities are also decreased, suggesting an increase in electron mobility with

reduction. Finally, a quadratic temperature dependance of resistivity indicates an electron-electron scattering process, since the collisions between electrons at higher temperatures increase, which turns in lower electron mobility [11].

The Seebeck coefficient (S) of STNO is rather high considering its high carrier concentration. The reason for the high S values is believed to be connected to materials high effective mass ($m^* = 11m_0$) [43]. When the effective mass is increased, the Seebeck coefficient is pronounced much more than the electron mobility is decreased, which results in an enhanced PF. The absolute value of S of STNO monotonically increases with temperature due to the fact that chemical potential of the material decreases with temperature.

Thermal conductivity of STNO is strongly dominated by the lattice contribution and drops proportionally to T^{-1} above room temperature (Figure 1.13 c), indicating Umklapp-type phonon-phonon interaction [68]. Thermal conductivity increases with carrier concentration above the carrier concentration of 3×10^{20} cm^{-3}. Below this value the thermal conductivity is independent of the carrier concentration [64]. The thermal conductivities of bulk polycrystalline STNO are reported to vary from as high as 10 W/mK [43] to 4.8 W/mK [42] at room temperature. Differences can arise from the specific features of bulk samples, such as phonon scattering at grain boundaries, scattering at inhomogeneities, or grain boundary seggregation of charged defects [54]. Nevertheless, differences can also occur due to using different measuring techniques and measuring conditions [69]. A systematic study of grain boundary effect on the thermal conductivity of pure STO was reported by Wang et al. [70]. Undoped STO was used in order to exclude the electronic conctribution to the thermal conductivity. By measuring thermal conductivity of STO ceramics with different grain sizes, a clear connection between the number of grain boundaries versus lattice thermal conductivity was found (Figure 1.14 a). The single crystals of STNO exhibited 10 W/mK at room temperature, while this value was reduced to 8 W/mK at the same temperature in a typical polycrystalline STNO ceramics with grain size ~ 20 μm. Nanosized STNO ceramics showed significantly lowered thermal conductivity of 5.3 W/mK at room temperature. This phenomenon was connected to increased phonon scattering of the low frequency (long wavelength) phonons due to lowering the phonon mean free path as the grains become smaller (Figure 1.14 b).

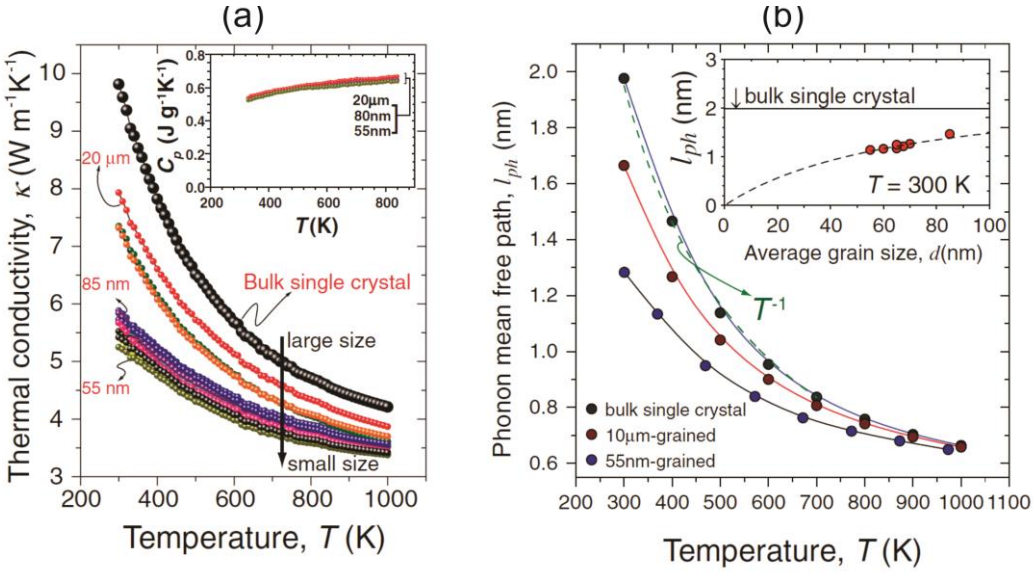


Figure 1.14: Thermal conductivity of STO ceramics depending on the grain size. Phonon mean free path of single crystal and polycrystalline ceramics depending on temperature [70].

Several studies focused on reducing thermal conductivity of STNO by adding constituents with low thermal conductivity in order to achieve higher ZT. For instance, Wang et al. [71] added mesoporous silica, Lingner et al. [72] fabricated STO glass-ceramics by adding SiO_2 and B_2O_3, while Wang et al. [73] introduced yttria-stabilized-zirconia (YSZ) nano-inclusions. Even though the thermal conductivity in all cases was succesfully lowered, this was not acompanied with improved ZT (0.17 at 900 K for mesoporous silica addition, 0.0001 at 923 K for glass-ceramic STNO, 0.22 at 900 K for YSZ STNO), since the electrical conductivity was reduced as well. Ohta et al. [64] studied the ZT of STNO versus the doping concentration. Up to x = 0.2 the figure of merit increased and then it droped. Reduction of ZT at x > 0.2 was connected to increased thermal conductivity once the carrier concentration exceeded 3×10^{21} cm^{-3}.

Absolute ZT values are strongly dependent on the fabrication processes as well as on thermoelectric measurement techniques and measurement conditions used. Reported absolute ZT values of bulk STNO differ significantly; from 0.02 – 0.37 at 1000 K, which could be connected to the reasons mentioned before [42], [43], [71], [72]. It is therefore reasonable to compare thermoelectric properties of samples syntesized at the same conditions and also using the same measurement equipment. The best ZT for bulk polycrystalline STNO at 1000 K remains 0.37, firstly reported by Ohta et al. [43] in 2006.

Chapter 2

Aims and Hypothesis

2.1 Description of the Problem

Electrical conductivity, Seebeck coefficient and thermal conductivity determine the figure of merit (ZT) of a thermoelectric material. Several studies imply that the reason for inherently low ZT of STNO is due to its high thermal conductivity. Hence, lowering this specific property without hindering power factor of thermoelectric oxide-based materials is a generally accepted hypothesis to improve its figure of merit. In transition metal oxides, phonons are the major contributors to the thermal conductivity making it possible to tune the phonon transport with negligible effect on electrical conductivity [74]. Improvement of ZT is therefore expected by effectively blocking the phonon vibrations in the STNO crystal lattice. Several approaches to hinder phonon propagation in thermoelectric materials have been proposed [75], including the complex crystalline structure [4], doping with heavy elements [76], mass fluctuations between different semiconductors with the same structure [77], impurities and structural defects, fabrication of phonon-glass electron-crystal [78] (PGEC) and nanostructuring [79].

Lattice conductivity can be reduced by various types of defects, which can scatter the charge carriers too. The mean free path for electrons/holes is usually greater than for phonons ($<$ 1 nm) [5], so it could be expected that the defects primarily effect the mobility rather than lattice conductivity. However, in many practical cases the ratio of the mobility to the lattice conductivity can be raised through defect scattering [5]. In 1956, Ioffe et al. [77] suggested that the formation of a solid solution of two semiconductors with the same crystal structure should lead to reduction of lattice conductivity. This was argued by the preservation of long-range order and since the wavelength of charge carriers is also large, they would suffer no additional scattering. However, the phonons that predominate in the heat conduction have short wavelenghts and they get scattered which is followed by reduced lattice thermal conductivity.

2.2 Aims of the Dissertation

The main aim of the study presented in this thesis was to enhance phonon scattering of STNO in order to lower its lattice thermal conductivity and consequently increase thermoelectric figure of merit. The phonon mean free path was assumed to be lower than the one of electron mean free path. The lattice thermal conductivity of STNO primarily contributes to the total thermal conductivity and it is expected that it can be lowered by introducing planar faults in the structure. Well known planar faults in the STO system are derived from the Ruddlesden-Popper [50] (RP) phases of $SrO(SrTiO_3)_n$ type, where perovskite n $\times$ $SrTiO_3$ blocks are interleaved by single SrO layers, which results in

parallel planar faults in [001] direction. This kind of defects can be introduced in two ways; either by initially following the $SrO(SrTiO_3)n$ stoichiometry or by adding a sufficient amount of excess AO (A = Ba, Sr, Ca) to STO. In the first case, the planar faults are SrO type, while in the second case they are AO-type (eg. SrO, (Sr/CaO), while (Sr/BaO) are not as energetically favourable). This is however not the only difference between the resulting RP-structure. When adding excess AO to STO, the final structure tends to be STO based, with randomly distributed planar faults. This led us to the asumption that Nb-doped STO with randomly spreaded faults in a STNO matrix would be a promissing candidate for a thermoelectric material, since we could retain the electrical transport in the basic Nb-doped STO matrix and enhance phonon scattering at the RP-type faults.

2.3 Organisation of the Experimental Work

STNO with 20% Nb was prepared by conventional solid-state synthesis using different atmospheres at equal temperature and holding time to evaluate the phase formation and degree of reduction depending on the oxygen partial pressure – $P(O_2)$.

Afterwards, two approaches were applied in order to modify the microstructure of STNO;

(a) addition of platelet Ruddlesden-Popper(RP)-type seeds or

(b) addition of excess SrO or CaO.

This was followed by solid state synthesis at 1500 °C for three hours in hydrogen (H_2) atmosphere. For a relative comparison of the thermoelectric properties, STNO, made in equal conditions as STNO with seeds (seeded STNO) and as STNO with SrO (STNO;SrO) or CaO (STNO;CaO) was studied using the same thermoelectric measurement equipment.

Prior to choosing the appropriate seeds to be added to STNO, a systematic study with regard to the platelet seeds was also done in order to possibly obtain already Nb-doped RP-type seeds, since it is assumed that electrically conductive seeds would lead to better thermoelectric performance as undoped RP-type seeds. Molten salt synthesis was estimated to be the most appropriate method to grow the desired crystals. Different doping concentrations and synthesis conditions were employed. The obtained seeds were evaluated in terms of microstructure and phase composition.

Chapter 3

Materials and Methods

3.1 Synthesis

3.1.1 Solid State Synthesis of 20% Nb-Doped $SrTiO_3$

Conventional solid-state synthesis by sintering the samples at 1500 °C for three hours using different atmospheres was employed to fabricate STNO. $SrCO_3$ (>99.9 %, Sigma–Aldrich), TiO_2 (99 %+, Alfa Aesar) and Nb_2O_5 (99 %+, Merck) starting powders were first mixed corresponding to the $Sr(Ti_{0.8}Nb_{0.2})O_3$ stoichiometry in ethanol, homogenized and calcined twice at 1200 °C for 12 h with intermediate ball milling. The calcined material was then crushed and milled in a planetary mill for 1 h in order to obtain the starting STNO powder that was used in all the subsequent sintering experiments.

Starting STNO powder was then cold-pressed into pellets and sintered at 1500 °C for 3 h in different atmospheres; either air, argon (High-Temperature Tube Furnace RHTH 120-300 -Nabertherm GmbH - Figure 3.1 a), mixture of argon and hydrogen (95:5) or pure hydrogen (Chamber Furnace Astro Industries 1100V-3080-W2 - Figure 3.1 b).

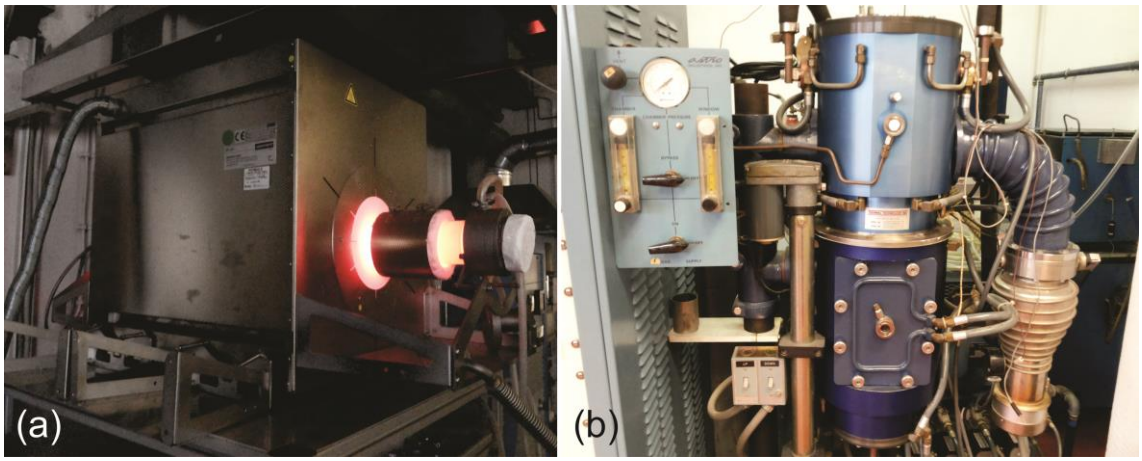


Figure 3.1: (a) High-temperature tube furnace adjusted for sintering in air or argon and (b) Chamber furnace for sintering in argon/hydrogen or hydrogen atmosphere.

3.1.2 Molten Salt Synthesis of Ruddlesden-Popper Type Platelet Crystals

Molten salt synthesis (MSS) was applied in order to synthesize RP-type seeds (Figure 3.2). The principle of MSS is crystal growth in a mixture of two salts, which have the eutectic temperature fairly lower than the melting temperature of individual salt.

Different doping concentrations (0 – 20% Nb) in addition to various synthesis temperatures were used in order to study the crystal development and phase formation of RP-type platelets. $SrCO_3$ (>99.9 %, Sigma Aldrich), TiO_2 (99 %+, Alfa Aesar) and Nb_2O_5 (99 %+, Merck) were used as initial powders in order to obtain $Sr_3Ti_2O_7$. The powders were mixed with ethanol and NaCl/KCl salts and then homogenized in planetary mill for one hour. The NaCl/KCl molar ratio was 1:1 and the reagents to salts volume ratio was 1:1. The dried mixture was then put into alumina crucible and heated at different temperatures; 1200 °C, 1250 °C and 1300 °C for four hours. After the synthesis the salts were removed by washing the product with hot deionized water several times and intermediate centrifuging.

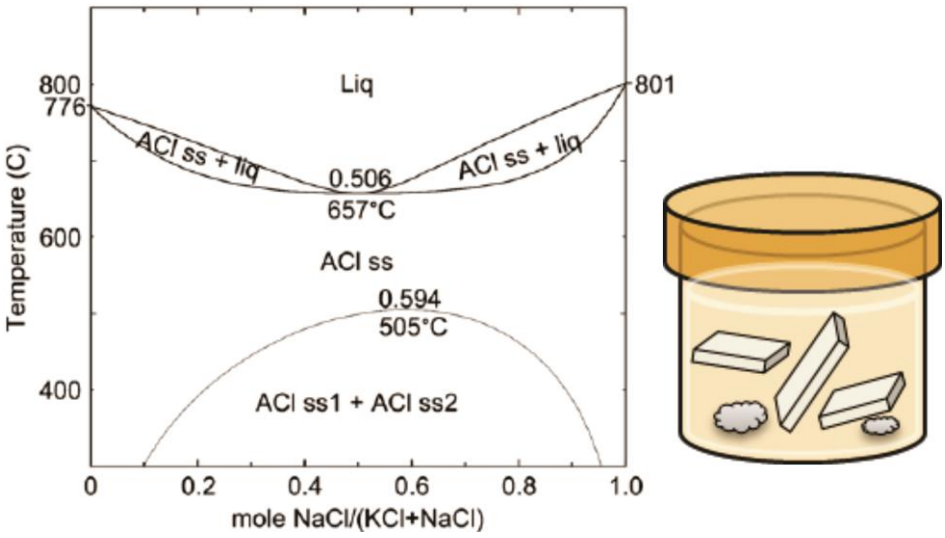


Figure 3.2: Binary phase diagram [80] showing the NaCl-KCl eutectic at 657 °C, at the 1:1 molar ratio of the salts. The scheme on the right illustrates the crystal growth in a molten salts medium when the temperature is raised above the eutectic temperature of the salts.

3.1.3 Seeded Nb-Doped $SrTiO_3$

Undoped product of the molten salt synthesis containing RP-type platelet crystals was chosen to be added to the initial STNO, since the systematic study of Nb-doped products showed a presence of undesired secondary phases. 10 w% of the product powder was added to STNO powder and stirred in an agate mortar. The powder mixture was then uniaxial pressed into pellets and sintered for 3 h in H_2 atmosphere. The obtained sample is hereinafter referred to as *Seeded STNO*.

3.1.4 Nb-Doped $SrTiO_3$ with Excess SrO or CaO

10% SrO or 10% CaO in the form of carbonates ($SrCO_3$ >99.9 % Sigma-Aldrich, $CaCO_3$ 99+%, Merck) were added to STNO in proper stoichiometry to obtain $Sr_{1.1}(Ti_{0.8}Nb_{0.2})O_3$ (*STNO;SrO*) or $SrCa_{0.1}(Ti_{0.8}Nb_{0.2})O_3$ (*STNO;CaO*). Ethanol was added to the powder mixtures and homogenized in a planetary mill for 1 h at 170 RPM. The dried mixtures were cold-pressed into pellets and sintered at 1500 °C in H_2 for 3 h.

3.2 Characterisation Methods

3.2.1 X-Ray Powder Diffraction (XRD)

X-ray powder diffraction analyses were carried out in a XRD diffractometer (XRD; D4 Endeavor, Bruker AXS) with a Bragg-Bretano geometry, a Cu-Kαradiation source (λ = 0.154 nm), and a Sol-X energy-dispersive detector. The XRD data were analyzed by the Diffrac.EVA software from Bruker.

3.2.2 Scanning Electron Microscopy (SEM)

The sintered pellets were cut perpendicular to the pressing direction, polished and chemically etched in 10% HF solution for 10-60 seconds. All samples were coated with a few-nm-thick carbon coating in order to ensure electrical conductivity.

The microstructural analysis was carried out using scanning electron microscopy (SEM) (Jeol JSM-5800, Jeol JSM-7600F) with energy-dispersive X-ray spectroscopy (EDXS) (Oxford Instruments Isis 300, Oxford Instruments INCA).

3.2.3 Transmission Electron Microscopy (TEM)

The thin foils for the TEM observations from the bulk materials were prepared using ion-milling techniques (Gatan, PIPS). For TEM observation of RP-type seeds two different specimen preparation techniques were applied; mechanical polishing and dimpling followed by conventional ion-milling or tripod polishing with additional ion-milling. In both preparation procedures RP-type crystals were embedded in epoxy resin and pressed between Si supports in order to align platelets parallel to the supports. Specimens were mechanically grinded to a thickness of 100 µm, followed by dimpling in a cross-section geometry down to a thickness of ~ 16 µm. Afterwards, the specimen was argon-ion milled at an accelerating voltage of 3.5 kV at an ion beam incidence angle of 8° to perforation in a Precision Ion Polishing System (PIPS) without sample cooling. In order to avoid eventual damage caused by ion-milling, specimens were prepared by tripod polishing in an automatic tripod polisher. The specimens were cut into slabs of ~ 1.5 mm wide and 2 mm long and attached to a specimen holder using thermoplastic wax. The specimens were polished using a diamond-lapping film (DLF) with 15 µm grain size to provide a planar surface. This was followed by polishing with DLFs. The final polishing step was done on a polyurethane cloth using a silica solution with 50 nm particle size in order to avoid wedge chipping and scratches on the polished surface. The specimen was thinned down to a thickness of 200 µm using 15 µm DLF. A wedge angle of 1° was introduced, which made the specimen more robust to handle. The specimens were polished down to a thickness of 10 µm using DLFs. The final polishing was performed to thin the wedge to electron transparency. The wedge-shaped specimens were additionally cleaned and thinned in PIPS at 3.5 keV for 60 minutes and at 0.6 kV for 20 min. During the ion-milling process the specimens were cooled using liquid nitrogen. The HRTEM revealed

that the amorphous region in ion-milled specimens was approximately 5 times as thick as compared to the specimens prepared by the tripod polishing method.

Transmission electron microscopy was carried out in Jeol microscopes (STEM, HRTEM) (Jeol JEM-2100, Jeol JEM-2010F, Jeol JEM-ARM CF) with energy-dispersive X-ray spectroscopy (Jeol JED, Oxford Isis 300).

3.2.4 Thermogravimetric Analysis (TGA)

Thermogravimetric analysis was conducted in a Netzsch instrument (STA 449 C/6/G Jupiter – QMS 403). The investigation was carried out in air atmosphere from room temperature to 1000 °C with a heating rate 10 °C/min.

3.2.5 Rietveld Analysis

The unit cell dimensions of the samples were determined by employing the Rietveld refinement of the XRD diffraction patterns, by using the Bruker analysis software Topas.

3.2.6 Measurement of Thermoelectric Properties

3.2.6.1 Thermal Conductivity Measurements

Thermal diffusivity (α) of the samples was carried out employing a commercial Laser Flash Apparatus (LFA, 427, Netzsch). The specific heat (c_p) was determined using a high-temperature Differential Scanning Calorimeter (DSC, Netzsch). The density (ρ) was determined by the Archimedes method. The thermal conductivity κ was then calculated from $\kappa = \rho \times \alpha \times c_p$. The measurement accuracy was determined as 8%.

3.2.6.2 Seebeck Coefficient and Electrical Conductivity Measurements

Seebeck coefficient and electrical conductivity were measured simultaneously by a custom-made measuring system with a four-probe in-line arrangement [81]. The temperature gradient was established in the sample by two gradient heaters, which are able to generate temperature gradient in both directions by alternately switching them on. The thermoelectrically induced voltage (V) was then measured by two n-type thermocouples. The sample conductivity was then calculated by the system from the following formula (Eq. 3.1):

$$\sigma = \frac{1}{2\pi s V C} \tag{3.1}$$

where s is the spacing between the tips and C is a geometrical correction factor accounting the sample size and geometry, as well as the spacing between the tips. The measurement accuracy was estimated to be 5% for electrical conductivity and 5% for Seebeck coefficient.

Chapter 4

Nb-Doped $SrTiO_3$ Synthesized in Different Atmospheres

From the defect chemistry of STNO (see Chapter 1.2.1.2) it is known that the sintering atmosphere influences the compensation mechanism of the extra charge of Nb^{5+} which is substituting for Ti^{4+} in STO. When high $P(O_2)$ is used, extra charge is compensated by the formation of strontium vacancies, while at low $P(O_2)$ it is compensated by the reduction of Ti^{4+} into Ti^{3+} and the formation of oxygen vacancies.

In order to study the level of reduction based on different surrounding partial pressures of oxygen $P(O_2)$ as well as the microstucture evolution and phase composition of STNO, cold-pressed STNO pellets with an initial composition of $Sr(Ti_{0.8}Nb_{0.2})O_3$ were sintered in various atmospheres; air (STNO-air), pure argon (STNO-Ar), argon/hydrogen mixture (95:5) (STNO-Ar-H_2) and pure hydrogen (STNO-H_2) by using the same sintering temperature and holding time.

Figure 4.2 shows powders of the crushed pellets after sintering them in different atmospheres. The level of reduction of Ti^{4+} into Ti^{3+} can be observed in the color of the sintered samples, since higher reduction appears in darker color. STNO-air exhibits a light gray color (Figure 4.1 a), STNO-Ar moderate gray (Figure 4.1 b), while STNO-Ar/H_2 and STNO-H_2 dark gray and black, respectively, indicating a high level of reduction (Figure 4.2 c and d).

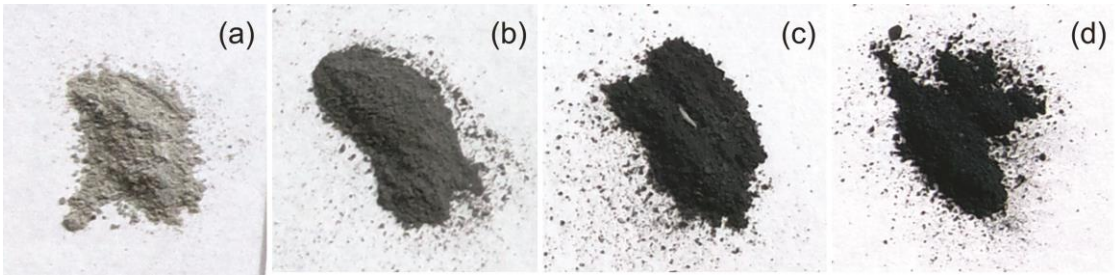


Figure 4.1: STNO powders obtained by crushing the pellets, sintered in (a) air, (b) argon, (c) argon/hydrogen and (d) hydrogen atmosphere.

The level of reduction was evaluated by thermogravimetric analysis (TGA) by exposing the sintered samples to oxygen atmosphere at elevated temperatures and measuring the weight gain due to the incorporation of ambient oxygen into the oxygen-deficient STNO structure [11]. The oxygen vacancies of oxygen deficient STNO are namely only stable up to ~ 400 °C in air. Figure 4.2 presents the curves obtained from the TGA measured from room temperature to 1000 °C in flowing air of STNO samples which were initially

sintered in different atmospheres. The powders of all four samples have turned to white color after TGA, indicating sufficient oxidation.

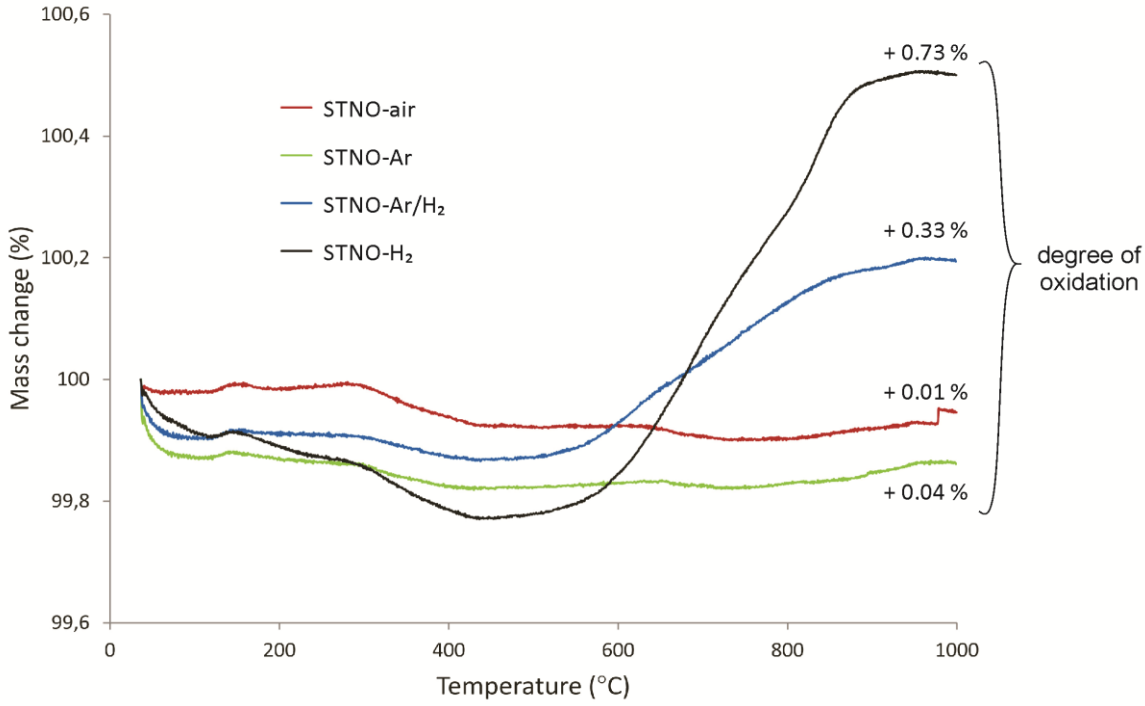


Figure 4.2: TGA curves of STNO samples initially sintered in different atmospheres (air-red, argon-green, argon/hydrogen-blue and hydrogen-black line). Weight increases are proportional to degrees of oxidation due to the incorporation of oxygen into the STNO oxygen deficient structures.

Table 4.1 presents the weight increase (in %) of the samples after oxidation. The samples that have been sintered in low $P(O_2)$ (STNO-Ar/H_2 and STNO-H_2) exhibit evident weight gain above 400 °C due to oxidation (0.33 and 0.73 mass % increase, respectively), while the samples sintered at higher $P(O_2)$ (STNO-air and STNO-Ar) show only a minor increase in weight (0.01 and 0.03 weight %, respectively). The weight loss in the range from room temperature to 400 °C is probably due to desorption of water, also observed in a study by Blennow et al. [11]. Weight increase was used to calculate the estimated concentration of Ti^{3+} in variously reduced STNO, based on the defect chemistry model proposed by Blennow et al. [82]. The concentration of [Ti^{3+}] (mol Ti^{3+}/mol of nominal $Sr(Ti_{0.8}Nb_{0.2})O_3$) in STNO is in this context basically equal to the concentration of oxygen vacancies, therefore (Eq. 4.1):

$$[Ti^{3+}](\%) = \frac{2\Delta m}{M_O} \frac{M_{STNO}}{(100 - \Delta m)} \times 100 \tag{4.1}$$

where Δm is weight increase in % after oxidation, M_{STNO} is the molar mass of STNO, and M_O is the molar mass of oxygen. The calculated Ti^{3+} concentrations, representing the proportion of reduced Ti^{4+}, are given in Table 4.1. It can be seen that STNO-air and STNO-Ar were just slightly reduced with less than 1% of Ti^{3+}, while the STNO-Ar/H_2 contained a substantial amount of reduced Ti^{3+} (~ 8%) and STNO-H_2 even more than twice the amount of Ti^{3+} (~ 18%) than STNO-Ar/H_2.

Table 4.1: Mass change (in %) and calculated concentration of [Ti^{3+}] (in %) of STNO samples sintered in different atmospheres.

Sintering atmosphere	air	Ar	Ar/H_2	H_2
Mass change 400 – 1000 °C (%) (±0.03 %) of STNO	0.01	0.04	0.33	0.73
[Ti^{3+}] (%)	0.24	0.96	7.94	17.57

Microstructures of chemically etched samples are revealed in Figure 4.3. Grain sizes of STNO-air, STNO-Ar and STNO-Ar/H_2 are similar, ranging from 0.7 µm to 3 µm. The grain size is bimodal in the sample STNO-H_2, where the grains range from 3 µm to 20 µm. Exaggerated grain growth in the STO-system is usually connected to excess TiO_2, which forms a liquid phase at high temperature. Excess TiO_2 also causes enhanced grain growth. However, no TiO_2 phase was detected in our samples. The back-scattered electron images (BEI) in the insets of Figure 4.3 reveal the phase composition of the samples. STNO-air and STNO-Ar consist of gray matrix, identified as STNO solid solution by the EDXS analysis (measuring points 1 and 3 in Table 4.2 and Figure 4.4) and bright elongated secondary phases (marked with arrows), which were assigned to $Sr_5(Nb_{1-x}Ti_x)_4O_{15}$ by the EDXS analysis (measuring points 2, 4 and 5). On the other hand, STNO-Ar and STNO-Ar/H_2 show a uniform contrast of the STNO solid solution (measuring points 6 and 7) without secondary phases.

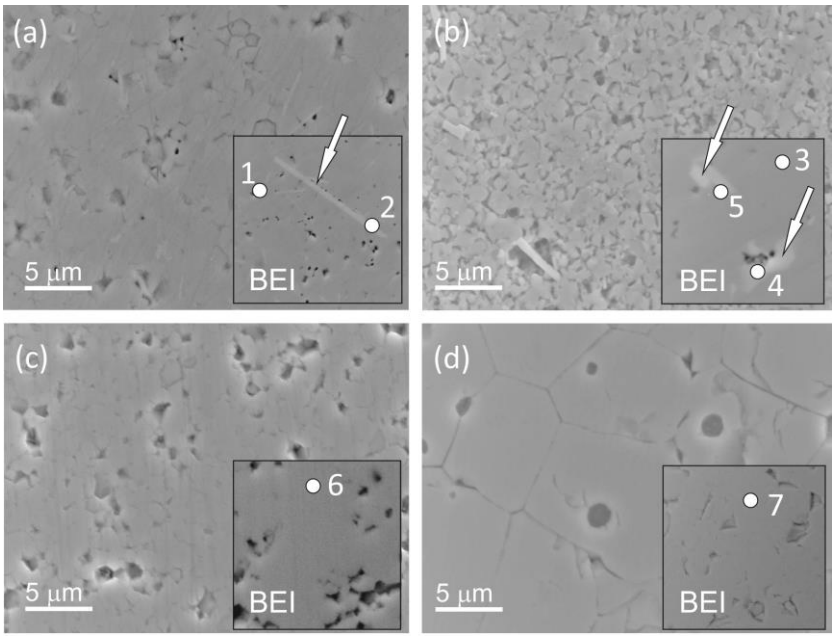


Figure 4.3: Secondary electron images (SEI) and Back-scattered electron images (BEI) of STNO samples, sintered in different atmospheres; (a) air, (b) argon, (c) argon/hydrogen, and (d) hydrogen. Numbered dots are the EDXS measuring points the results of which are given in Table 4.2.

Table 4.2: Atomic elements concentration (± 0.2 %) from the EDXS measurements of STNO-air, STNO-Ar, STNO-Ar/H_2 and STNO-H_2. Atomic % of oxygen is calculated by the STO stoichiometry. Measuring points are indicated in the SEM image of Figure 4.3.

sample	**point#**	Sr (at %)	Ti (at %)	Nb (at %)	O (at %)
STNO-air	**1**	19.4	16.7	3.2	60.8
	2	19.2	11.7	7.6	61.5
STNO-Ar	**3**	19.0	16.4	3.6	60.9
	4	19.0	10.3	8.9	61.8
	5	19.2	9.9	9.1	61.8
STNO-Ar/H_2	**6**	19.5	16.1	3.6	60.8
STNO-H_2	**7**	19.6	16.2	3.5	60.7

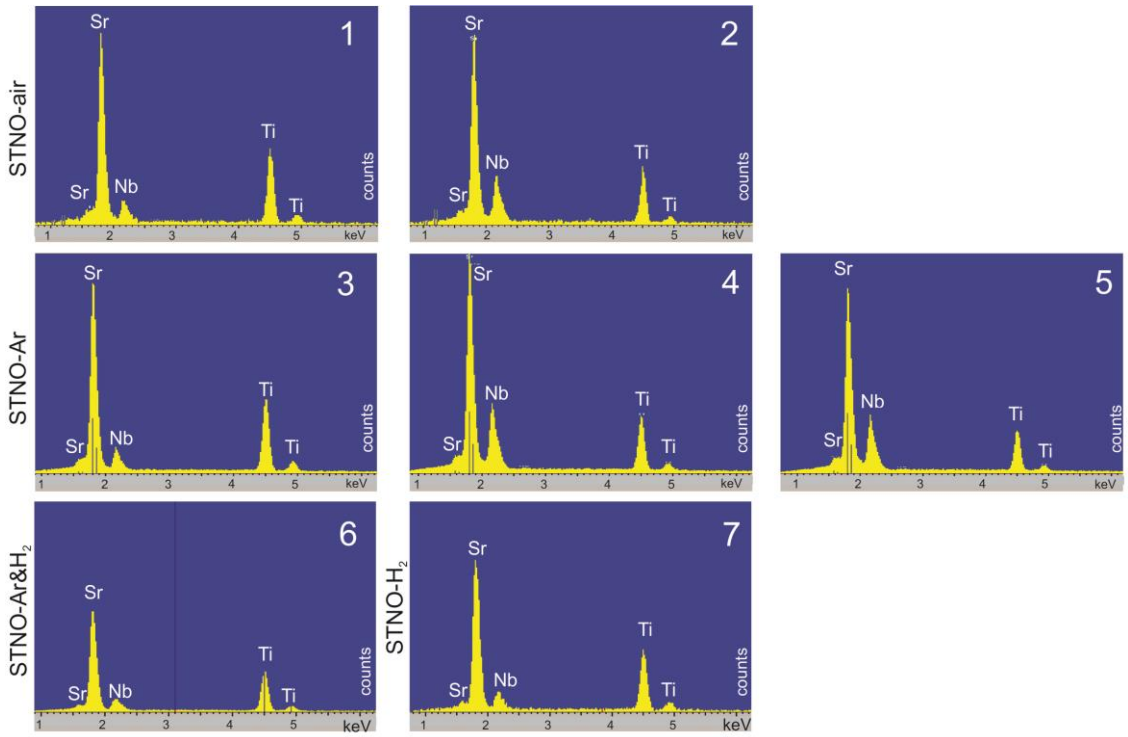


Figure 4.4: EDXS specters. Measuring points (1-7) are indicated in Figure 4.3.

Phase composition of the samples was also studied by XRD. For the purpose of comparison, XRD was performed on the initial STNO powder as well. All the resulting XRD patterns are joined in Figure 4.5. The XRD of the initial powder reveals diffraction peaks of STO phase in addition to low intensity diffraction peaks of a secondary phase, which were assigned to $Sr_5Nb_4O_{15}$. In the sintered samples, however, the diffraction peaks of the secondary phase decreased, regardless of the sintering atmosphere. Some traces of the secondary phase could still be detected in the samples which were sintered in high $P(O_2)$ (STNO-air and STNO-Ar), which is in agreement with the findings of the SEM analysis. The samples sintered in low $P(O_2)$ (STNO-Ar/H_2, STNO-H_2) exclusively showed diffraction peaks of the STO phase, indicating a complete formation of STNO solid solution. The presence of a secondary phase in the samples sintered at high $P(O_2)$ could be connected with the defect chemistry of the STNO; where the extra charge of the dopant is compensated by formation of the strontium vacancies and consequently the SrO secondary phase, which in these conditions apparently prefers to react with Nb_2O_5 to form $Sr_5Nb_4O_{15}$. STNO diffraction peaks show a shift to the left in low $P(O_2)$ (right hand side of Figure 4.5), which indicates an increase of the unit cell dimensions due to a higher level of Nb^{5+} (0.064 nm) replacements of the smaller Ti^{4+} (0.060 nm) in the STNO solid solution.

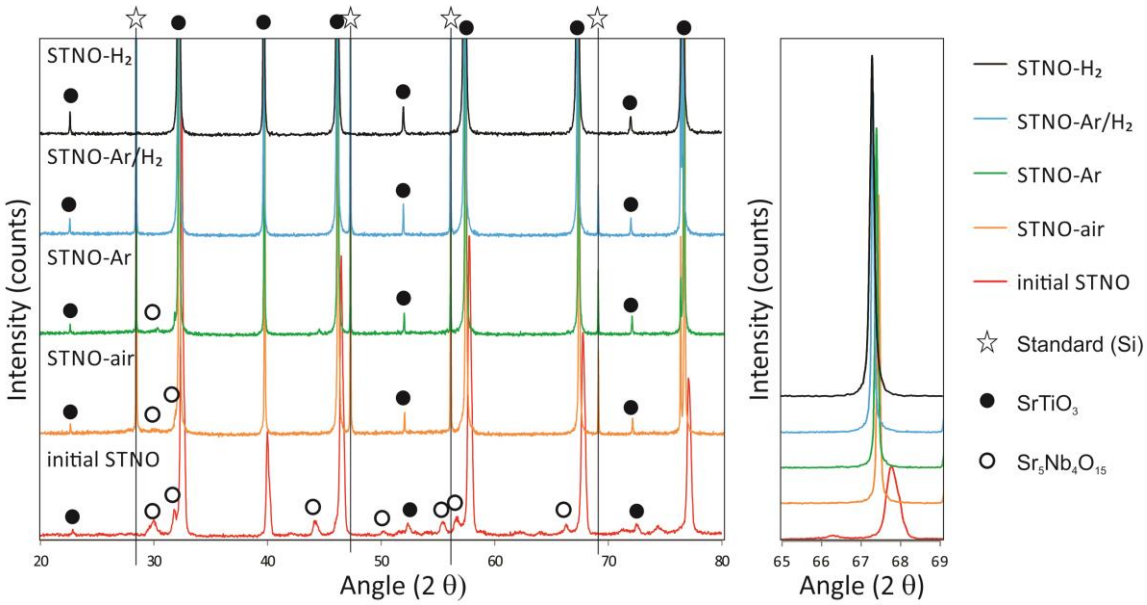


Figure 4.5: XRD patterns of initial STNO powder (red line) and STNO powders sintered in different atmospheres: air (orange line), argon (green line), argon/hydrogen (blue line) and hydrogen (black line).

XRD patterns were used for the Rietveld refinement in order to determine the unit cell dimensions of the STNO samples, sintered in different atmospheres. Results are given in Table 4.3.

Table 4.3: Unit cell dimensions based on the Rietveld analyses of XRD data of STNO, sintered in different atmospheres; a (cube edge length) and V (volume).

Sintering atmosphere	air	Ar	Ar/H_2	H_2
a (nm) of STNO	0.3925	0.3927	0.3931	0.3934
V ($\times 10^{-3}$ nm^3) of STNO	60.47	60.56	60.76	60.88

Based on the data from Table 4.3, the graph in Figure 4.6 illustrates the unit cell expansion as the $P(O_2)$ decreases, which is in agreement with the observed diffraction left peak shift of the reduced samples, seen from the XRD patterns (Figure 4.5).

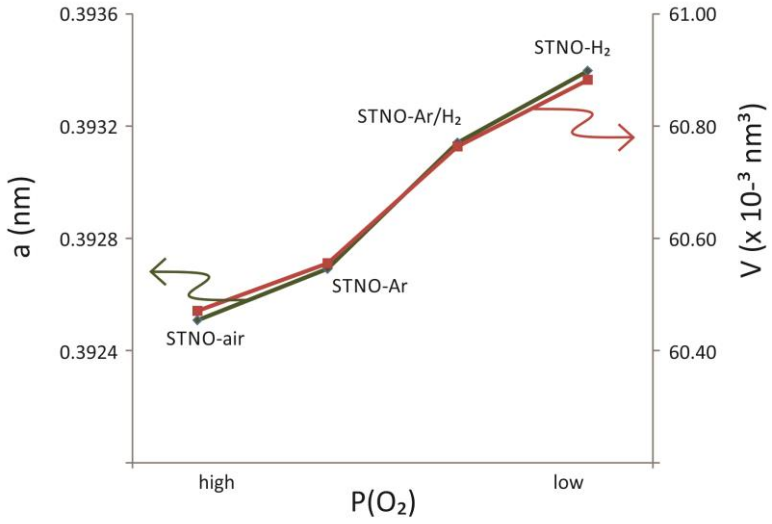


Figure 4.6: Unit cell dimensions of STNO samples, sintered in different atmospheres (different $P(O_2)$) obtained by the Rietveld refinement of the XRD patterns.

In conclusion, from characterization results of STNO samples sintered in different atmospheres it is evident that lower $P(O_2)$ leads to higher reduction of Ti^{4+} into Ti^{3+}. Lower $P(O_2)$ is also more favorable in terms of forming single phase STNO, while at higher $P(O_2)$ traces of secondary $Sr_5Nb_4O_{15}$ were detected by XRD and by SEM. Grain growth was significantly enhanced in the samples, sintered in low $P(O_2)$. Absence of the $Sr_5Nb_4O_{15}$ second phase and a larger unit cell of the STNO-Ar-H_2 and STNO-H_2 indicate that low $P(O_2)$ enhances the diffusion of the niobium from $Sr_5Nb_4O_{15}$ into STNO solid solution. This is in agreement with the SEM observation with back-scattered electrons (BEI), where in the darker gray matrix composed of STNO, brighter phases could be seen in the STNO-air and STNO-Ar. The STNO-Ar/H2 and STNO-H_2 showed a uniform contrast, with no secondary phases.

Chapter 5

Lowering the Thermal Conductivity of $Sr(Ti_{0.8}Nb_{0.2})O_3$ by SrO and CaO Doping: Microstructure and Thermoelectric Properties

In this chapter, a paper entitled "Lowering the Thermal Conductivity of $Sr(Ti_{0.8}Nb_{0.2})O_3$ by SrO and CaO Doping: Microstructure and Thermoelectric Properties" [83] by Marja Jerič, Johannes deBoor, Janez Zavašnik and Miran Čeh is presented.

The purpose of this article was to study the microstructure development by doping STNO with excess SrO (STNO;SrO) or CaO (STNO;CaO) and evaluate the obtained microstructure in terms of influence on thermoelectric properties.

It was found that in both cases the excess doping resulted in planar faults, derived from the RP-type phases, embedded in the STNO matrix. When STNO was doped with SrO, up to 50-µm-long lamellae were grown in the microstructure of STNO grains. CaO doping resulted in more or less isotropic grains with intergrowth of planar faults in some grains and also somewhat higher porosity was observed. Thermoelectric measurements showed that the presence of planar faults successfully reduced the thermal conductivity in STNO;SrO and STNO:CaO. The Seebeck coefficient of STNO; SrO was comparable with STNO, while the STNO:CaO was enhanced, which resulted in an improved thermoelectric figure of merit.

In conclusion, SrO and CaO doping proved to be a promising approach in terms of lowering the thermal conductivity of STNO.

J Mater Sci (2016) 51:7660–7668

Lowering the thermal conductivity of $Sr(Ti_{0.8}Nb_{0.2})O_3$ by SrO and CaO doping: microstructure and thermoelectric properties

Marja Jerič[1,2,*], Johannes de Boor[3], Janez Zavašnik[4], and Miran Čeh[1,4]

[1] Department for Nanostructured Materials, Jožef Stefan Institute, Jamova cesta 39, 1000 Ljubljana, Slovenia
[2] Jožef Stefan Postgraduate School, Jamova 39, 1000 Ljubljana, Slovenia
[3] Institute of Materials Research, German Aerospace Center, 51147 Cologne, Germany
[4] Center for Electron Microscopy and Analysis, Jamova 39, 1000 Ljubljana, Slovenia

Received: 1 March 2016
Accepted: 7 May 2016
Published online: 20 May 2016

© Springer Science+Business Media New York 2016

ABSTRACT

Excess SrO and CaO were added to the $Sr(Ti_{0.8}Nb_{0.2})O_3$ thermoelectric material, which was structurally compensated by the formation of Ruddlesden–Popper-type planar faults with the compositions SrO and/or (Sr, Ca)O. Both types of doping significantly changed the original isotropic $Sr(Ti_{0.8}Nb_{0.2})O_3$ microstructure and resulted in the formation of lamellar Ruddlesden–Popper-type phases within the $Sr(Ti_{0.8}Nb_{0.2})O_3$ grains. Three-dimensional networks of single Ruddlesden–Popper-type faults were also observed in the $Sr(Ti_{0.8}Nb_{0.2})O_3$ for both types of doping. The combination of both structural features significantly lowered the thermal conductivity in comparison with $Sr(Ti_{0.8}Nb_{0.2})O_3$ due to the enhanced phonon scattering observed at the planar faults, which proves that introducing such defects is a promising method for lowering the thermal conductivity of the $Sr(Ti_{0.8}Nb_{0.2})O_3$ thermoelectric material. The highest figure of merit ($ZT = 0.08$) was achieved with CaO doping, since the significantly reduced thermal conductivity was accompanied by an increased power factor.

Introduction

Nb-doped $SrTiO_3$ (STNO) exhibits one of the highest thermoelectric figure of merit (ZT) for oxide-based n-type thermoelectric materials, i.e., $ZT = 0.40$ at 1100 K [1].

Even though the thermoelectric properties of this material are not yet satisfactory for practical applications, the material clearly exhibits some advantageous properties over its metal/alloy counterparts, such as a high-temperature stability, nontoxicity, and relative abundance. The thermoelectric ZT is given by the following equation: (Eq. 1):

$$ZT = \frac{\sigma S^2}{\kappa} T, \quad (1)$$

where σ denotes the electrical conductivity, S is the Seebeck coefficient, κ is the thermal conductivity, and

Address correspondence to E-mail: marja.jeric@ijs.si

DOI 10.1007/s10853-016-0048-8

T is the absolute temperature of the material. Thus, for an efficient thermoelectric material, a high electrical conductivity and Seebeck coefficient coupled with a low thermal conductivity are required. Since STNO exhibits a relatively high thermal conductivity [2], it is understandable that recent studies have focused on how to reduce this particular thermoelectric parameter in order to achieve a higher ZT [3–7].

The thermal conductivity is the sum of two contributions: the electronic contribution (κ_e) and the lattice contribution (κ_L). For STNO, the lattice thermal conductivity contribution strongly prevails over the electronic contribution, which is due to the high-phonon frequencies of the major constituent oxygen [3]. One way to lower the lattice thermal conductivity is to introduce crystallographic defects into the basic microstructure, which would result in phonon scattering at the defects [3]. The well-known planar defects in SrO-excess $SrTiO_3$, often referred to as Ruddlesden–Popper (RP)-type defects [8], can, if ideally ordered, result in the formation of the $SrO{\cdot}(SrTiO3)_n$ homologous series compounds, where n represents the number of perovskite blocks interleaved by a single SrO layer. Although the microstructure of non-stoichiometric $SrTiO_3$ (STO) with AO-excess (A = Ca, Sr, Ba) has been extensively studied over recent decades [9–14], there are no reports on the thermoelectric properties of STO and/or STNO with the addition of AO.

In contrast to stoichiometric RP ceramics with the $(AO){\cdot}(ABO_3)_n$ stoichiometry, up to 10 mol% AO doping of STO results in more-or-less ordered RP faults embedded within the perovskite structure [14]. While the RP-based ceramic is reported to have a lower thermal conductivity than the perovskite STO due to phonon scattering at the $(SrO)/(SrTiO_3)_n$ interfaces, the electrical conductivity and the Seebeck coefficient are lower as well, leading to decreased ZT values [3].

The lower electrical conductivity in RP phases is coupled with the numerous insulating SrO layers that are randomly distributed, whereas the reduced Seebeck coefficient is connected with a decreased effective mass (m*) of the RP phases as compared to the STO [3]. This may lead to a conclusion that AO-doped (A = Sr, Ca) STNO would be an appropriate candidate for a thermoelectric material, since phonon scattering interfaces in the form of AO planar faults would be introduced to lower the thermal conductivity, while the electrical conductivity of the main phase, donor-doped STO perovskite, would be retained.

Since STNO ceramics are reported to have one of the best ZT [1, 15, 16], we chose this composition and doped it either with SrO to obtain $(SrO)_{1.1}(SrTi_{0.8}Nb_{0.2}O_3)$ or with CaO to obtain $((Ca,Sr)O)_{1.1}(SrTi_{0.8}Nb_{0.2}O_3)$. After the synthesis, we studied the excess doping effect on the microstructure development as well as on the thermoelectric properties. We focused on the influence of planar faults incorporation on reducing the thermal conductivity in these AO-excess solid solutions with the perovskite structure.

Materials and methods

To obtain 20 at.% Nb-doped STO, the $SrCO_3$ (Sigma-Aldrich), TiO_2 (Rutile, Alfa Aesar), and Nb_2O_5 (Merck) starting powders were weighed according to the $Sr(Ti_{0.8}Nb_{0.2})O_3$ stoichiometry. The powders were mixed with ethanol and homogenized in a planetary mill for 1 h. The slurry was dried at 80 °C. The homogenized powder was pressed into pellets and calcined twice at 1200 °C for 12 h, with intermediate planetary-mill homogenization. After the calcinations, the pellet was crushed again and milled in order to obtain a homogenous Nb-doped initial powder for subsequent reactions with SrO and CaO, which were added to the initial $Sr(Ti_{0.8}Nb_{0.2})O_3$ stoichiometric composition in the form of carbonates. The following three compositions were prepared and pressed into pellets: $Sr(Ti_{0.8}Nb_{0.2})O_3$ (STNO), $Sr(Ti_{0.8}Nb_{0.2})O_3$ with 10 mol% of excess SrO (STNO:SrO), and $Sr(Ti_{0.8}Nb_{0.2})O_3$ with 10 mol% of excess CaO (STNO:CaO). Prior to pressing the powder mixtures into pellets, they were homogenized in a planetary mill for 1 h with the addition of ethanol. The pressed pellets were sintered at 1500 °C for 3 h in a hydrogen atmosphere.

The pellet powder, obtained by crushing the sintered pellets in an agate mortar, was investigated by XRD (D4 Endeavor, Bruker AXS, Karlsruhe, Germany) using the Bragg-Brentano geometry, Cu-Kα radiation, and a Sol-X energy-dispersive detector. The microstructural analysis of the sintered pellets was performed using scanning electron microscopy (SEM) (Jeol JSM-5800, Jeol JSM-7600F) with energy-dispersive X-ray spectroscopy (EDXS) (Oxford Instruments Isis 300, Oxford Instruments INCA) and

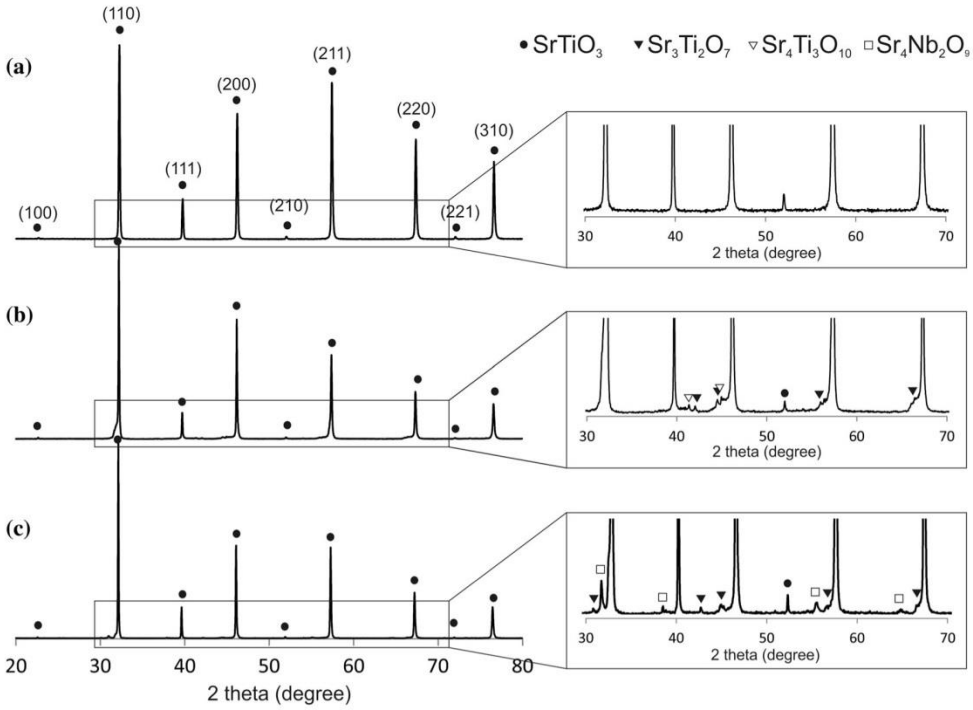


Figure 1 X-ray powder diffraction patterns of **a** STNO, **b** STNO:SrO and **c** STNO:CaO.

transmission electron microscopy (TEM) (Jeol JEM-2100, Jeol JEM-2010F) with energy-dispersive X-ray spectroscopy (Jeol JED, Oxford Isis 300). The sample preparation for the SEM microstructural analysis involved cutting the sintered pellets perpendicular to the pressing direction, with subsequent grinding, polishing, and chemical etching. In the end, all the samples were coated with a few-nm-thick carbon layer in order to ensure electrical conductivity. Thin foils for the TEM observations were prepared from the bulk materials using ion-milling techniques (Gatan, PIPS).

The thermal conductivity κ was calculated using $k(T) = \alpha(T) \times c_p(T) \times \rho(T)$, where k is the thermal conductivity, α is the thermal diffusivity, c_p is the specific heat, and ρ is the density of the material. The thermal diffusivity was measured using a commercial Laser Flash Apparatus (LFA, 427, Netzsch Gerätebau, Selb, Germany). The specific heat was determined using DSC (Netzsch) and the density was determined by Archimedes' method. The temperature-dependent S and σ measurements were carried out in a custom-built setup in a He atmosphere [17]. The electrical conductivity was determined by employing a four-probe, in-line geometry, and the Seebeck coefficients were determined using a variable temperature gradient to account for any undesired voltage offsets. The measurement accuracy was estimated to be 8 % for κ, 5 % for σ, and 5 % for S, based on an intra-laboratory comparison and the data analysis described elsewhere [18].

Results and discussion

XRD analysis

Figure 1 shows the X-ray powder diffraction patterns for the STNO, STNO:SrO, and STNO:CaO. The main diffraction peaks in all three samples were consistent with those corresponding to $SrTiO_3$, thus confirming the formation of a $Sr(Ti_{1-x}Nb_x)O_3$-type solid solution. No secondary phases could be seen in the XRD pattern of the STNO sample (Fig. 1a), whereas relatively low-intensity diffraction peaks of secondary phases were detected for the STNO:SrO

and the STNO:CaO in the corresponding XRD patterns. The detected secondary phases in STNO:SrO were identified as $Sr_3Ti_2O_7$ and $Sr_4Ti_3O_{10}$ (Fig. 1b), while the detected secondary phases in STNO:CaO were $Sr_3Ti_2O_7$ and $Sr_4Nb_2O_9$ (Fig. 1c). The presence of the $Sr_4Nb_2O_9$ secondary phase was also observed by Lee et al. [19] in STO doped with Nb and Ca. This was explained as a consequence of exceeding the structural tolerance factor for perovskite (ABO_3) by Goldschmidt [20] in the case when there is mutual substitution of Ca on the Sr sites and Nb on the Ti sites in STO.

SEM analysis

The SEM secondary-electron (SE) images of the chemically etched surfaces of STNO, STNO:SrO, and STNO:CaO are shown in Fig. 2. The STNO sample (Fig. 2a) contains isotropic grains in the size range from 1 to 5 μm. The STNO:SrO sample (Fig. 2b), on the other hand, reveals a microstructure where up to 50-μm-long lamellae are intergrown within the STNO grains. Due to this intergrowth and the etching of the polished surface, it is very difficult to distinguish the grain boundaries, especially since the lamellar phase seems to be etched away much more quickly than the STNO grains. However, from the back-scattered electron (BE) image of the polished STNO:SrO surface (inset of Fig. 2b), we can clearly distinguish a brighter and a darker phase. It was concluded that the bright phase is related to the Ruddlesden–Popper-type phases, since the Sr content in these phases is higher than in the stoichiometric STNO, leading to a brighter BE image. Also, the EDXS analysis from this region confirmed a higher content of Sr, as compared to the Sr content measured in the darker phase (Table 1). The SEM image of STNO:CaO (Fig. 2c) shows a more-or-less isotropic grain growth, in comparison to the sample STNO:SrO. The observed pores represent not only the initial porosity, but also the porosity caused by the chemical etching of the Ruddlesden–Popper(RP)-type phases. Namely, a closer inspection of the larger voids in Fig. 2c clearly shows the layered morphology of the etched-away phase, which is characteristic for RP-type phases. The CaO doping also resulted in somewhat higher porosity (Fig. 2d) in comparison with the STNO- and SrO-doped samples. This may well be a consequence of agglomeration of $CaCO_3$ particles, resulting in relatively large isolated pores. When imaging the polished surface using back-scattered electrons (BE) (inset in Fig. 2c), we can also observe the presence of two phases. The EDXS analysis of the darker phase showed that it is a solid solution of the

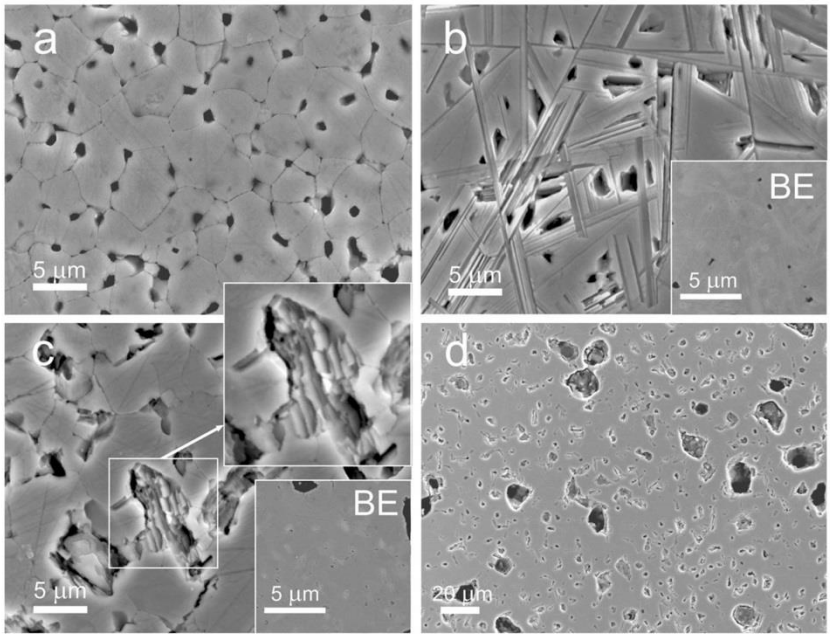


Figure 2 Secondary-electron SEM images of chemically etched **a** STNO, **b** STNO:SrO and **c** STNO:CaO. The *insets* show the back-scattered electron images (BE) of STNO:SrO and STNO:CaO. **d** STNO:CaO at a lower magnification showing isolated pores.

Table 1 EDXS analysis of brighter and darker areas in the STNO:SrO and STNO:CaO in at.%, calculated to the oxygen stoichiometry

	Sr (at.% ± 0.2)	Ti (at.% ± 0.3)	Nb (at.% ± 0.2)	Ca (at.% ± 0.2)	O (at.%) (calc)
STNO:SrO					
Brighter (1)	23.3	14.1	3.2		59.5
Brighter (2)	22.5	14.6	3.2		59.7
Darker (1)	20.0	15.4	4.0		60.7
Darker (2)	20.5	15.5	3.5		60.4
STNO:CaO					
Brighter (1)	20.4	13.6	3.1	3.8	59.1
Brighter (2)	19.4	10.6	4.9	6.2	59.0
Darker (1)	17.9	15.8	3.7	2.0	59.1
Darker (2)	18.3	15.8	3.4	2.0	60.5

perovskite type with a composition corresponding to $(Sr_{1-x}Ca_x)(Ti_{1-y}Nb_y)O_3$, while the composition of the brighter phase corresponds to Nb- and Ca-enriched RP phases (Table 1).

It should be mentioned that during the sample preparation for the SEM, the STNO and STNO:CaO samples were relatively compact, while the STNO:SrO was brittle and mechanically unstable, which can be related to the existence of numerous lamellae of RP-type phases that are growing in random directions, very often through many grains, as was also observed in the SrO–$SrTiO_3$ system [11].

TEM analysis

The transmission electron microscopy investigation was conducted in order to confirm the existence of RP-type planar faults in the STNO samples with the addition of SrO and/or CaO. A pure STNO solid solution was also investigated for a comparison. TEM bright-field images of the pure STNO showed that the STNO solid solution grains contained no planar faults of any kind (Fig. 3a). Furthermore, the interfaces between the grains were clean with no observable interface phase. However, when SrO and/or CaO were added to the STNO, various nanostructured features were observed.

In the SrO-doped STNO, we can observe three distinctly different regions, i.e., the STNO solid solution, the regions with ordered SrO faults, and regions with disordered and/or isolated SrO planar faults (Fig. 3b). In the STNO solid solution regions, no planar faults are observed. In the ordered regions, one SrO layer is always followed by two perovskite STNO blocks, which correspond to the $Sr_3(Ti_{1-x}Nb_x)_2O_7$ RP-type phase in which Nb and Ti occupy the same crystallographic site. In the region containing disordered and/or isolated SrO faults, they always run parallel to the {001} low-index zone axes of the $Sr(Ti_{1-x}Nb_x)O_3$ perovskite structure. The resulting difference in the incorporation of SrO faults, i.e., ordered or disordered, may well result from the different starting local compositions of excess SrO. If the local concentration of SrO (after thermal decomposition of $SrCO_3$) is sufficient to form a nuclei of the $Sr_3(Ti,Nb)_2O_7$-type RP phase at the of STNO/SrO interface, it is expected that these nuclei will grow as long as there is sufficient amount of available SrO. Since the growth in the *a* and *b* directions of the RP phase is much faster compared to the growth rate in the *c* direction, the RP-type phase is formed in the shape of a stand-alone lamella (phase) and which can also be topotactically intergrown with the STNO matrix phase. When the STNO grains contain no disordered and/or isolated SrO planar faults, the starting local SrO concentration was not sufficient to form thermodynamically stable $Sr_3(Ti_{1-x}Nb_x)_2O_7$-type RP phase. This implies that initial distribution of SrO phase during calcination and sintering plays a decisive role in the nature of SrO planar faults intergrowth with the perovskite matrix. Our previous investigations confirmed that it is very difficult to synthesize ideal, stoichiometric, Ruddlesden-Popper phases using solid-state reactions where the SrO layers and the perovskite blocks alternate in exact ordering [12].

A similar structural phenomenon was observed in STNO with excess CaO. Again, ordered and/or random 3D networks of RP-type planar faults can be observed in the STNO grains (Fig. 3c–f). According to previous investigations, it can be concluded that the

J Mater Sci (2016) 51:7660–7668 7665

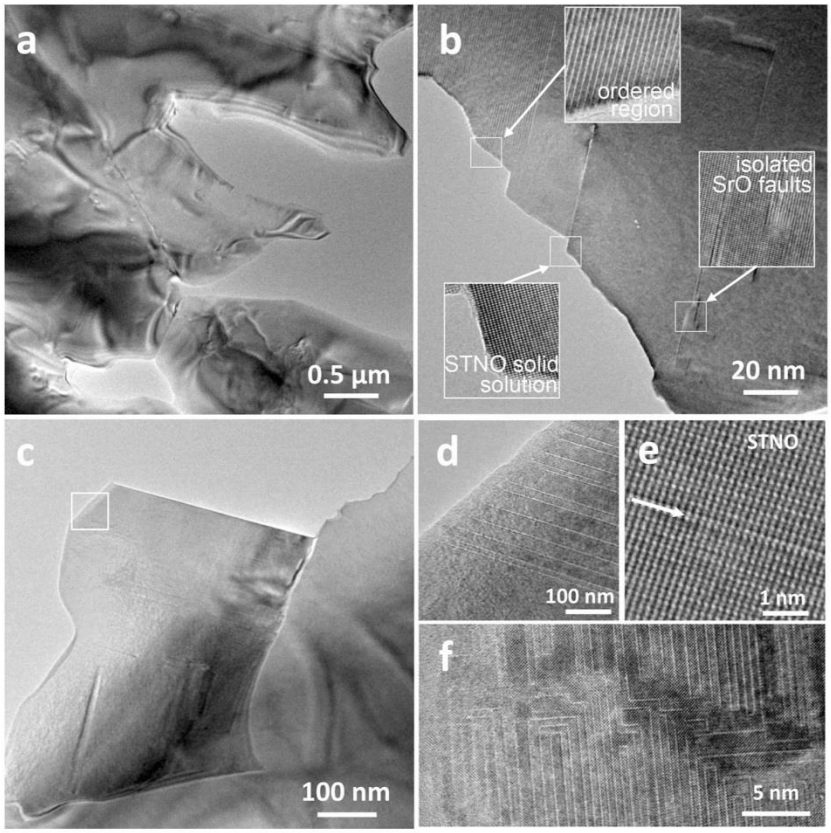


Figure 3 **a** Bright-field TEM micrograph of pure STNO. No planar faults can be observed within the grains. **b** TEM micrographs of STNO:SrO showing three different regions; a region of ordered SrO layers ($Sr_3(Ti_{1-x}Nb_x)_2O_7$ RP-type phase), STNO solid solution (perovskite structure $Sr(Ti_{1-x}Nb_x)O_3$ with no planar faults), and isolated SrO faults (individual SrO planar faults in the $Sr(Ti_{1-x}Nb_x)O_3$ matrix). **c** TEM micrograph of STNO:CaO with marked region having parallel RP faults (**d**). HRTEM of a single RP fault as seen in the [110] zone axis. **e** Isolated SrO planar fault (marked with an arrow) in a $Sr(Ti_{1-x}Nb_x)O_3$ perovskite matrix **f** 3D network of RP faults in STNO:CaO.

planar faults are predominately CaO-rich [13], since due to the smaller Ca ion it is easier for the Ca to be incorporated at the faults, thus minimizing the local stresses in the lattice. This would also explain why in CaO-excess STNO many more planar-fault loops are observed as compared to the SrO-excess STNO (Fig. 3f). The TEM investigations thus confirmed that the addition of SrO and/or CaO to the STNO perovskite solid solution in fact caused the formation of RP-type planar faults that were observed within the STNO grains, either as ordered sequences or 3D networks.

Thermoelectric properties

Figure 4 shows the thermoelectric properties of STNO, STNO:SrO, and STNO:CaO. The thermal conductivity (κ) is shown in Fig. 4a. The κ of STNO is 10 W/mK at room temperature, but this drops with increasing temperature to 5 W/mK at 650 °C. The κ of STNO:SrO is 5.9 W/mK at room temperature, but drops linearly with increasing temperature to 3.7 W/mK at 650 °C. Similarly, the κ of STNO:CaO drops linearly from 4.1 W/mK at room temperature to 3.3 W/mK at 650 °C. The κ values for STNO:SrO and STNO:CaO were thus successfully lowered in comparison with the pure STNO, especially in the low-temperature region where the thermal conductivity is connected to phonon scattering at the RP-planar faults. Moreover, at room temperature, the κ of STNO:CaO is even lower than the κ of STNO:SrO, whereas at 650 °C they exhibit similar values. The additional reduction of κ at room temperature for the STNO:CaO as compared with the STNO:SrO could be due to several reasons: mass-defect phonon scattering between the Sr and Ca [19], the phonon scattering at the planar-fault loops, observed with the TEM and also due to the locally isolated pores.

7666 J Mater Sci (2016) 51:7660–7668

The electronic (κ_e) and the lattice (κ_L) contributions to the thermal conductivity were calculated using the Wiedemann–Franz law [21] (Eq. 2)

$$\kappa_e = LT\sigma, \tag{2}$$

where L is the theoretical Lorenz factor calculated by applying the free electron theory (2.45×10^{-8} WΩ/K^2), T is the temperature, and σ is the measured electrical conductivity. The κ_L is consequently (Eq. 3)

$$\kappa_L = \kappa_{tot} - \kappa_e. \tag{3}$$

The electrical contribution to the total thermal conductivity in all three samples is ~1 % (Fig. 4a—inset), so we can conclude that $\kappa_{tot} \approx \kappa_L$. Therefore, the reduction of κ for STNO:SrO and STNO:CaO in comparison with the pure STNO can be attributed to the planar faults due to two reasons: the reduction of κ_L for the STNO:SrO and STNO:CaO, and the emphasized reduction of κ at lower temperatures, where the phonon scattering at the crystallographic defects is predominant.

The electrical conductivity measurements are shown in Fig. 4b. The σ of STNO increases slightly from 137 S/cm at room temperature to 156 S/cm at 350 °C, where it reaches a plateau. For STNO:CaO the σ drops with temperature from 125 S/cm at room temperature to 107 S/cm at 650 °C, and a change from semiconducting at lower temperature to metal behavior at higher temperature can be seen at 250 °C. However, the σ is lower than the one for STNO. On the other hand, the σ for STNO:SrO shows a slight enhancement with increasing temperature from 60.5 S/cm at room temperature to 64.0 S/cm at 650 °C. In comparison with STNO, the σ values for STNO:CaO and STNO:SrO are lower across the whole temperature range. The reason for the decreased σ of STNO:CaO could be the lower solubility of the electron donor Nb in $SrTiO_3$ due to Ca substitution on the Sr site and, furthermore, the presence of the secondary phase $Sr_4Nb_2O_9$, as mentioned in the XRD analysis section. A decreased electrical conductivity in Nb-doped $SrTiO_3$ in the presence of a secondary phase and at lower Nb-doping levels was also recently observed by Zhang et al. [1]. Another reason for the lower electrical conductivity could be the reduced grain size in the STNO:CaO in comparison with the STNO, which leads to a larger grain-boundary surface area that scatters the electrons. On the other hand, the even lower electrical conductivity of STNO:SrO in comparison with STNO:CaO could

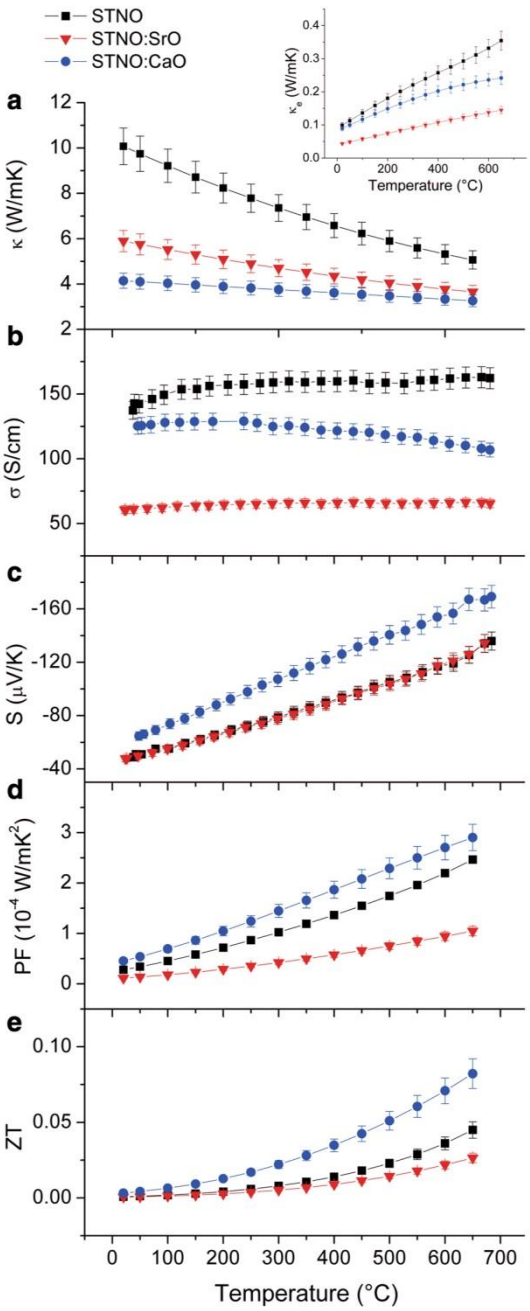


Figure 4 **a** Thermal conductivity (κ) and electrical contribution to the total thermal conductivity (κ_e) (*inset*) **b** Electrical conductivity (σ), **c** Seebeck coefficient (S), **d** Power factor (PF) and **e** Figure of merit (ZT) of STNO (*black*), STNO:SrO (*red*), and STNO:CaO (*blue*).

J Mater Sci (2016) 51:7660–7668 7667

be related to the numerous planar faults in the grains of STNO:SrO, running in random directions. Furthermore, the decreased σ for STNO:SrO and STNO:CaO with no, or only a slight, increase in S can be related to the lower electron mobility, caused by the crystallographic defects in the SrO- and CaO-doped samples.

The measured values for the Seebeck coefficients (S) are shown in Fig. 4c. The values of S are negative, which is typical for n-type semiconductors. The S for the samples STNO and STNO:SrO exhibit similar values in the whole temperature range. S of STNO and STNO:SrO are -44.9 and -42.6 μV/K at room temperature and increase to -125.5 and -128.0 μV/K at 650 °C, respectively. On the other hand, the S for STNO:CaO is higher across the whole temperature range and increases from -60.4 μV/K at room temperature to -165.0 μV/K at 650 °C. This increase of S for the STNO:CaO in comparison with the STNO and STNO:SrO is in agreement with a study of Fukuyado et al. [22], where an increase in S for $(Sr_{1-x}Ca_x)(Ti_{1-y}Nb_y)O_3$ with increasing Ca substitution at the Sr sites was observed.

The power factors (PFs) calculated from the Seebeck coefficients and the electrical conductivities are shown in Fig. 4d. At room temperature, the values of all three samples are comparable, whereas at higher temperatures the differences are more evident. Therefore, the highest PF of 2.9×10^{-4} W/mK^2 occurs for the STNO:CaO at 650 °C, due to the highest S and in spite of the lower σ. The PF of STNO reaches 2.5×10^{-4} W/mK^2 at 650 °C, which is higher than 1.0×10^{-4} W/mK^2 for STNO:SrO at 650 °C, due to the higher σ of the STNO.

The values for the electrical conductivity, the Seebeck coefficient, and the thermal conductivity were used to calculate the thermoelectric figure of merit (ZT) for STNO, STNO:SrO, and STNO:CaO (Fig. 3e). The values of ZT are enhanced with temperature and reach maxima at the highest temperature of 650 °C: the ZT of STNO:CaO reaches a value of 0.08, whereas the ZT of STNO and STNO:SrO are 0.05 and 0.03, respectively. The enhancement of ZT for STNO:CaO is due to the significantly lowered κ and the improved PF. On the other hand, in spite of the successfully reduced κ for STNO:SrO, the ZT was lower due to the decreased PF. Finally, in this study, it was shown that the relative ZT was increased for the STNO:CaO in comparison with pure STNO. However, the absolute ZT values of STNO:CaO and even STNO are quite low in comparison with the best ZT for the STNO reported in the literature (0.40 at 1100 K or 0.37 at 1000 K) [1]. Indeed, quite a large scatter of the ZT values for bulk STNO can also be found in different studies reported [1, 2, 4, 6]; in the range of 0.02–0.37 (~1000 K) where different synthesis methods and thermoelectric measurement techniques were used. Fabrication processes were found to strongly affect the microstructural development and the charge carrier concentration which consequently led to various thermoelectric properties of a material. Therefore, it is reasonable to expect that higher absolute ZT values for STNO, STNO:SrO, and STNO:CaO could be achieved by optimizing the processing conditions.

Conclusion

Excess SrO and CaO were added to a $Sr(Ti_{0.8}Nb_{0.2})O_3$ (STNO) solid solution with the perovskite structure in order to lower the thermal conductivity of this thermoelectric material. While the XRD analysis of the STNO showed only the presence of the STO phase, relatively low-intensity diffraction peaks of the secondary phases were detected in the STNO:SrO and STNO:CaO. The microstructures of the SrO- and CaO-excess STNO revealed the presence of lamellar phases within the STNO grains, which contained ordered AO-type (A = Sr, Ca) planar faults and were thus identified as Ruddlesden–Popper-type phases. In some regions, random three-dimensional networks of these AO-type (A = Sr, Ca) planar faults were also observed. In comparison with the STNO, the thermal conductivities of the STNO:SrO and STNO:CaO were successfully lowered due to phonon scattering at the planar faults. The thermal conductivity of STNO:CaO was even lower as STNO:SrO, which was connected to mass-defect phonon scattering between the Sr and Ca and also to closed porosity. SrO doping resulted in low power factor, leading to a low ZT of 0.03 at 650 °C in comparison with the STNO. On the other hand, the ZT values for the CaO-doped STNO increased to 0.08 at 650 °C, as compared to a ZT of 0.05 for the STNO, which proves that CaO doping is a promising approach to increase the ZT of STNO due to the significantly lowered κ and the increased power factor. Finally, our observation that embedded planar faults in the microstructure coupled with a closed porosity lowered the thermal conductivity in

doped STNO can most likely also be applied as a more general approach in other oxide thermoelectric materials in order to reduce the thermal conductivity.

Acknowledgements

The authors would like to thank the Slovenian Research Agency (ARRS), project number PR-03768, and to the European Union Seventh Framework Programme [FP7/2007-2013] under grant agreement n°312483 (ESTEEM2), for the financial support of this work. Also, we would like to thank Silvo Zupančič for technical assistance in the high-temperature sintering, Medeja Gec and Andreja Šestan for TEM sample preparation, Werner Schönau for thermal conductivity measurements, and Paul McGuiness for proofreading.

References

[1] Zhang B, Wang J, Zou T, Zhang S, Yaer X, Ding N, Liu C, Miao L, Li Y, Wu Y (2015) High thermoelectric performance of Nb-doped $SrTiO_3$ bulk materials with different doping levels. J Mater Chem C 3(43):11406–11411

[2] Ohta S, Ohta H, Koumoto K (2006) Grain size dependence of thermoelectric performance of Nb-doped $SrTiO_3$ polycrystals. J Ceram Soc Jpn 114(1325):102–105

[3] Lee KH, Kim SW, Ohta H, Koumoto K (2006) Ruddlesden-Popper phases as thermoelectric oxides: Nb-doped $SrO(SrTiO_3)_n$(n = 1,2). J Appl Phys 100(6):063717

[4] Wang N, Han L, He H, Ba Y, Koumoto K (2010) Effects of mesoporous silica addition on thermoelectric properties of Nb-doped $SrTiO_3$. J Alloy Compd 497(1–2):308–311

[5] Lingner J, Letz M, Jakob G (2013) $SrTiO_3$ glass–ceramics as oxide thermoelectrics. J Mater Sci 48(7):2812–2816

[6] Wang N, Chen H, He H, Norimatsu W, Kusunoki M, Koumoto K (2013) Enhanced thermoelectric performance of Nb-doped $SrTiO_3$ by nano-inclusion with low thermal conductivity. Sci Rep 3:3449

[7] Jerič M, de Boor J, Jančar B, Čeh M (2016) An enhanced thermoelectric figure of merit for $Sr(Ti_{0.8}Nb_{0.2})O_3$ based on a Ruddlesden–Popper-polytype-induced microstructure. J Eur Ceram Soc 36(5):1177–1182

[8] Ruddlesden SN, Popper P (1958) The compound $Sr_3Ti_2O_7$ and its structure. Acta Crystallogr A 11(1):54–55

[9] Masayuki F, Junzo T, Shinichi S (1988) Planar faults and grain boundary precipitation in non-stoichiometric (Sr, Ca)TiO_3 ceramics. Jpn J Appl Phys 27(7R):1162

[10] Fujimoto M, Suzuki T, Nishi Y, Arai K, Tanaka J (1998) Calcium-ion selective site occupation at Ruddlesden-Popper-type faults and the resultant dielectric properties of a-site-excess strontium calcium titanate ceramics. J Am Ceram Soc 81(1):33–40

[11] Šturm S, Rečnik A, Scheu C, Čeh M (2000) Formation of Ruddlesden-Popper faults and polytype phases in SrO-doped $SrTiO_3$. J Mater Res 15(10):2131–2139

[12] Šturm S, Rečnik A, Čeh M (2001) Nucleation and growth of planar faults in SrO-excess $SrTiO_3$. J Eur Ceram Soc 21(10–11):2141–2144

[13] Šturm S, Rečnik A, Kawasaki M, Yamazaki T, Watanabe K, Shiojiri M, Čeh M (2002) Experimental atomically resolved HAADF-STEM imaging—a parametric study. JEOL News 37(1):22

[14] Šturm S, Shiojiri M, Čeh M (2009) Atomic-scale structural and compositional analyses of Ruddlesden-Popper planar faults in AO-excess $SrTiO_3$ (A = Sr^{2+}, Ca^{2+}, Ba^{2+}) ceramics. J Mater Res 24(08):2596–2604

[15] Ohta H, Kim S, Mune Y, Mizoguchi T, Nomura K, Ohta S, Nomura T, Nakanishi Y, Ikuhara Y, Hirano M, Hosono H, Koumoto K (2007) Giant thermoelectric Seebeck coefficient of a two-dimensional electron gas in $SrTiO_3$. Nat Mater 6(2):129–134

[16] Ohta S, Nomura T, Ohta H, Hirano M, Hosono H, Koumoto K (2005) Large thermoelectric performance of heavily Nb-doped $SrTiO_3$ epitaxial film at high temperature. Appl Phys Lett 87(9):092108

[17] de Boor J, Stiewe C, Ziolkowski P, Dasgupta T, Karpinski G, Lenz E, Edler F, Mueller E (2013) High-temperature measurement of seebeck coefficient and electrical conductivity. J Electron Mater 42(7):1711–1718

[18] de Boor J, Müller E (2013) Data analysis for Seebeck coefficient measurements. Rev Sci Instrum 84(6):065102

[19] Lee KH, Kim SW, Ohta H, Koumoto K (2007) Thermoelectric properties of layered perovskite-type $(Sr_{1-x}Ca_x)_3(Ti_{1-y}Nb_y)_2O_7$. J Appl Phys 101(8):083707

[20] Goldschmidt VM (1926) Die Gesetze der Krystallochemie. Naturwissenschaften 14(21):477–485

[21] Franz R, Wiedemann G (1853) Ueber die Wärme-Leitungsfähigkeit der Metalle. Ann Phys 165(8):497–531

[22] Fukuyado J, Narikiyo K, Akaki M, Kuwahara H, Okuda T (2012) Thermoelectric properties of the electron-doped perovskites $Sr_{1-x}Ca_xTi_{1-y}Nb_yO_3$. Phys Rev B 85(7):075112

Chapter 6

Influence of Nb-Doping of $Sr_3Ti_2O_7$ Platelet Crystals on Their Composition and Crystal Growth

In this chapter, a paper "Influence of Nb-Doping of $Sr_3Ti_2O_7$ Platelet Crystals on Their Composition and Crystal Growth", (submitted to journal Materials and Technology) by Marja Jerič, Medeja Gec and Miran Čeh is presented.

The purpose of this research was to investigate the influence of Nb doping on phase formation and crystal growth of RP-type seeds and finally to obtain $Sr_3(Ti_{0.8}Nb_{0.2})_2O_7$ platelet crystals. Donor doped seeds were namely assumed to be more appropriate to be added to STNO thermoelectric ceramics as they would not hinder the electrical transport in contrast to undoped $Sr_3Ti_2O_7$.

The study revealed that the dopant had a significant effect on the crystal growth and phase formation of the final product powder. Thus, the formation of platelet-like seeds was inhibited as the Nb concentration was increased and moreover emergence of the strontium niobate phase increased. However, the EDXS analysis revealed that the platelet seeds indeed contain Nb in the solid solution and an exact ordering of the SrO in the RP-type phase of the platelet seeds was observed. Finally, a formation mechanism for Nb-doped $Sr_3Ti_2O_7$ based on our findings was proposed.

In conclusion, the study showed that in the synthesis conditions used, Nb-doped RP-type seeds indeed started to form. However a major part of the Nb was also used to form undesired strontium niobates. Based on the proposed formation mechanism, it is expected that by adjusting the synthesis conditions it would be possible to increase the amount of platelet Nb-doped seeds and decrease the secondary phase in the final product.

Influence of Nb-Doping of $Sr_3Ti_2O_7$ Platelet Crystals on Their Composition and Crystal Growth

Marja Jerič[1,2,*], Medeja Gec[1], Miran Čeh[1,3]

[1] Jožef Stefan Institute, Department for nanostructured materials, Jamova 39, Ljubljana, Slovenia

[2] Jožef Stefan Postgraduate School, Jamova 39, Ljubljana, Slovenia

[3] Center for Electron Microscopy and Microanalysis

We investigated the influence of different amounts of Nb doping as well as the influence of the synthesis temperature on composition and crystals growth of $Sr_3(Ti_{1-x}Nb_x)_2O_7$ platelet crystals prepared by the molten salt synthesis (MSS). The size of the platelet crystals, as well as their thickness, depends on the synthesis temperature as well as on the amount of added Nb. The platelet crystals with a Ruddlesden-Popper-like structure grow much faster along the ***a*** and ***b*** directions than along the ***c*** direction. Furthermore, $SrTiO_3$ was always detected as a secondary phase due to the evaporation of SrO during the MSS. Nb-doping in excess of 10 mol% also resulted in the formation of strontium niobates. TEM investigations confirmed that the platelet $Sr_3(Ti_{1-x}Nb_x)_2O_7$ crystals exhibited an ideal ordering of SrO in this Ruddlesden-Popper-type phase, i.e., each SrO layer is strictly followed by two $Sr(Ti,Nb)O_3$ perovskite blocks. It is expected that by prolonging the time of the MSS it would be possible to increase the Nb content in the $Sr_3(Ti_{1-x}Nb_x)_2O_7$ solid solution, thus increasing the electrical conductivity of the platelets.

Keywords: A1.Doping, A2.Seed Crystals, B1.Perovskites, A2.Growth from melt

1. Introduction

One of the possible uses of $Sr_3Ti_2O_7$ platelet crystals is to add them to the $Sr(Ti_xNb_{1-x})O_3$ thermoelectric material [1-3] in order to improve its figure of merit (ZT). Namely, the $Sr_3Ti_2O_7$ seeds incorporated into the $Sr(Ti_xNb_{1-x})O_3$ solid solution with the perovskite structure could serve as phonon barriers due to the complex crystal structure with nanostructured ordering of the SrO faults within the $Sr_3Ti_2O_7$. Preferably, the increased phonon scattering in this kind of structure would lead to a reduction of the thermal conductivity and, consequently, an improved thermoelectric figure of merit. $Sr_3Ti_2O_7$ platelet crystals were reported to be synthesized by molten salt synthesis (MSS) [4-6]. This method consists of dissolving the starting materials into liquid salts at elevated temperatures to form saturated solutions [7,8]. Upon slow cooling, the nucleation of thermodynamically stable compounds takes place with the subsequent growth of some nuclei during the process of cooling. Typically, a mixture of salts with the eutectic composition is used in order to obtain a liquid salt phase at a relatively low temperature. Upon completion of the temperature cooling cycle, the solidified salts are removed by washing the product powder with hot deionized water. The obtained material in the form of monocrystals and/or agglomerates of monocrystals can be used as a final product or can be used as an additive for other materials. In cases when monocrystals grown by the MSS process exhibit special morphological features, such as preferential growth along certain crystallographic planes, they can be used as seed crystals in polycrystalline oxide materials to induce or promote exaggerated and/or textured grain growth during sintering [9]. This approach has also frequently been used in thick-film production where doctor-blade coating has been used to spread the suspension of powders with the seeds on the substrate [10].

Among the numerous ceramic powder materials prepared by MSS [11-14], $Sr_3Ti_2O_7$ is one of the stable Ruddlesden-Popper (RP) [15] phases in which two cubic perovskite blocks are interleaved with a single SrO planar fault that has a rock-salt-type structure. Due to its tetragonal crystal structure, it is possible to synthesize $Sr_3Ti_2O_7$ by MMS in the form of platelet crystals, since the crystal growth in the *a* and *b* directions is much faster than the crystal growth in the c direction. This is why the micron-sized $Sr_3Ti_2O_7$ platelets have pronounced (100) and (010) facets.

Since $Sr_3Ti_2O_7$ is an insulator, adding $Sr_3Ti_2O_7$ platelets into the $Sr(Ti,Nb)O_3$ would, in addition to lowering thermal conductivity, also lead to an undesired reduction in the electrical conductivity of the final material. This is why donor-doped $Sr_3Ti_2O_7$, i.e., electrically conductive $Sr_3Ti_2O_7$ platelet seeds, would serve as a more appropriate choice for adding to the $Sr(Ti,Nb)O_3$ solid solution. In this way the seeds would serve as phonon-scattering centers, while not significantly hindering the electron transport. This is why we report on the synthesis of Nb-doped $Sr_3Ti_2O_7$ platelet crystals by MSS. We investigated the influence of Nb addition on the formation of $Sr_3(Ti_{1-x}Nb_x)_2O_7$ ($0<x<0.2$) platelet crystals, as well as the influence of the synthesis temperature on their crystals' size, composition and morphology.

2. Experimental procedures

Molten salt synthesis (MSS) was used to prepare Nb-doped $Sr_3Ti_2O_7$ platelet crystals. $SrCO_3$, TiO_2 and Nb_2O_5 starting powders were weighed in accordance with $Sr_3(Ti_{1-x}Nb_x)_2O_7$, with x = 0, 0.01, 0.05, 0.10, 0.15 and 0.2, whereas the KCl and NaCl salts were weighed in a 1: 1 molar ratio. The starting powders and the salts were then mixed in a 1: 1 weight ratio, dissolved in ethanol and homogenized in a planetary mill for 1 hour. The homogenized slurry was dried at 80°C. The dry powders were then sealed in several alumina crucibles and heated in a chamber furnace at 1200°C, 1250°C and 1300°C for 4 hours. The cooling rate was 1°C/min. After the reaction, the product powders were dissolved in hot distilled water and centrifuged at 5500 rpm for 10 minutes. The distilled water containing dissolved salts was drained away. The washing was repeated four times in order to completely remove the salts. The remaining sediments were dried at 80°C for several hours.

The obtained product powders were analyzed with X-ray powder diffraction (XRD) (D4 Endeavor, Bruker AXS), using Cu-K_α radiation and a Sol-x energy-dispersive detector. The microstructures of the obtained powders were investigated in scanning electron microscopes (Jeol JSM-5800, Jeol JSM-7600F) equipped with energy-dispersive X-ray spectroscopy (EDXS) (Oxford instruments Isis 300, Oxford Instruments INCA) and in a transmission electron microscope (Jeol JEM-2010F) equipped with a slow-scan CCD camera (Gatan, Orius), EDXS (Oxford Instruments Isis 300, Oxford Instruments) and EELS (Gatan, PEELS 677).

Specimens for the TEM observation were prepared by mechanical polishing and dimpling, followed by ion-milling. The first step in the preparation procedures was to mix the MSS product powder with an epoxy resin and to press the mixture between Si supports in order to align as many platelets as possible parallel to the Si supports. After conventional mechanical grinding and dimpling [16], the specimens were ion-milled to perforation with Ar+ ions at 3.5 kV using an incidence angle of 8° (Gatan, PIPS).

3. Results and discussion

3.1. X-ray powder diffraction (XRD)

Figure 1 shows XRD patterns of the obtained MSS products with initial compositions corresponding to $Sr_3(Ti_{1-x}Nb_x)_2O_7$, with x = 0, 0.01, 0.05, 0,10, 0,15 and 0.20, synthesized at 1300°C. The observed diffraction peaks for the samples with an initial stoichiometry x = 0 and for the samples with x = 0.01 and x = 0.05 of Nb-doping correspond to $SrTiO_3$, $Sr_3Ti_2O_7$ and $Sr_4Ti_3O_{10}$. It is interesting to observe that with an increasing amount of initial Nb-doping the relative intensity of the $Sr_4Ti_3O_{10}$ diffraction peaks increases, while the relative intensity of the $Sr_3Ti_2O_7$ diffraction peaks decreases. At higher Nb-doping, i.e., x > 0.1, the strontium niobate phases $Sr_4Nb_2O_9$ and Sr_2NbO_4 are present. A smaller amount of Sr_2TiO_4 can also be observed. The relative intensity of the diffraction peaks for the $Sr_4Nb_2O_9$ and Sr_2NbO_4 increases with an increasing amount of initial Nb-doping.

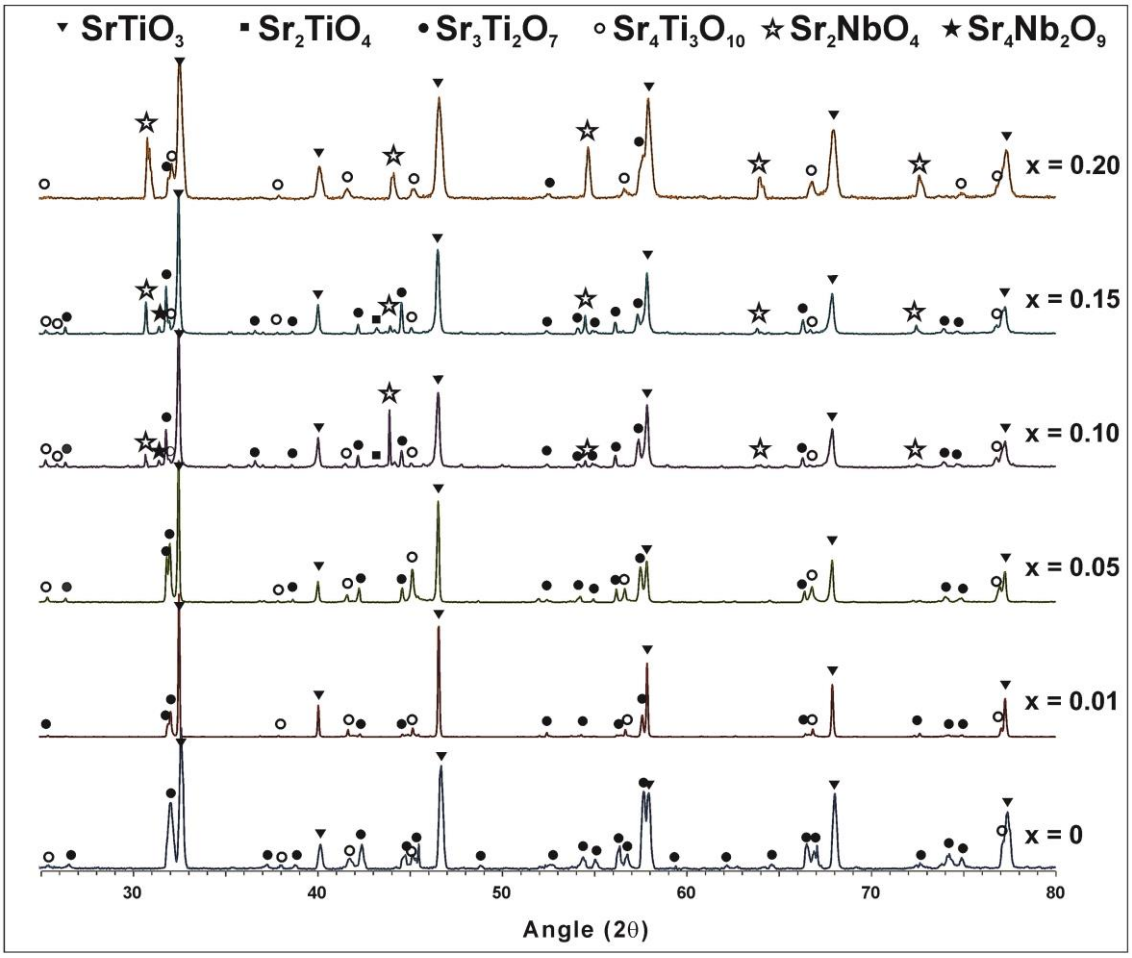


Figure 1: XRD spectra of MSS final products corresponding to initial compositions of $Sr_3(Ti_{1-x}Nb_x)_2O_7$ with x = 0, 0.01, 0.05, 0.10, 0.15 and 0.20, synthesized at 1300°C

The XRD data of the $Sr_3(Ti_{1-x}Nb_x)_2O_7$ MSS product powders with x = 0 and x = 0.20 synthesized at temperatures of 1200°C, 1250°C and 1300°C are shown in Figure 2. The sample with the initial composition of $Sr_3Ti_2O_7$ (x = 0) (Figure 2a) consists of $SrTiO_3$, $Sr_3Ti_2O_7$ with some $Sr_4Ti_3O_{10}$ and unreacted $SrCO_3$ at the lowest synthesis temperature of 1200°C. With increasing temperature the relative intensity of the $SrTiO_3$ and $SrCO_3$ diffraction peaks decreases, while the relative intensity of the diffraction peaks of the $Sr_3Ti_2O_7$ and $Sr_4Ti_3O_{10}$ increases. The relatively high content of $SrTiO_3$ in the MSS sample with the initial composition $Sr_3Ti_2O_7$ can be explained by the SrO evaporation during the synthesis[17]. Some other authors also reported that they used a SrO-excess composition in the starting material in order to compensate for the SrO loss during the synthesis, i.e., $Sr_{3.1}Ti_2O_7$ and/or $Sr_{3.2}Ti_2O_7$ [4,6].

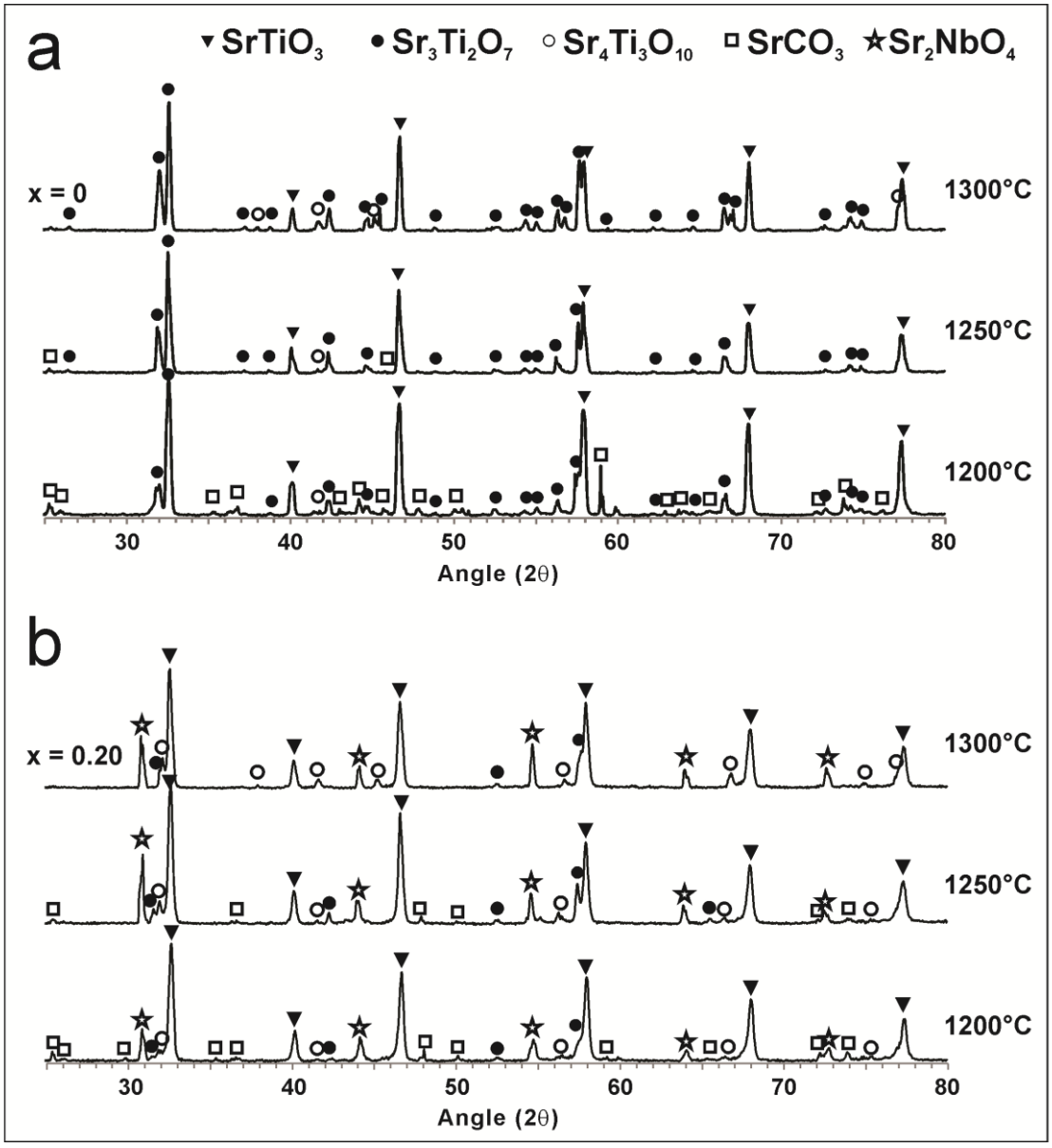


Figure 2: XRD spectra of samples synthesized at 1200°C, 1250°C and 1300°C with initial compositions $Sr_3(Ti_{1-x}Nb_x)_2O_7$ (a) x = 0 and (b) x = 0.20.

On the other hand, the XRD of the MSS sample with the initial composition $Sr_3(Ti_{0.8}Nb_{0.2})_2O_7$ (x = 0.2) (Figure 2b) synthesized at 1200°C reveals diffraction peaks of $SrTiO_3$ and strontium niobate (Sr_2NbO_4) as the main phases with some $Sr_3Ti_2O_7$, $Sr_4Ti_3O_{10}$ and unreacted $SrCO_3$. With increasing synthesis temperature the relative intensity of the diffraction peaks of $SrTiO_3$ and $SrCO_3$ decreases, while the relative intensity of the diffraction peaks of Sr_2NbO_4, $Sr_3Ti_2O_7$, $Sr_4Ti_3O_{10}$ increases.

3.2. SEM and EDXS analysis

Figure 3 shows SEM images of the $Sr_3(Ti_{1-x}Nb_x)_2O_7$ MSS products with x = 0, 0.01, 0.05, 0.10, 0.15 and 0.20, synthesized at 1300°C. The sample with the initial composition $Sr_3Ti_2O_7$ (x = 0) consists of thin orthogonal platelet crystals reaching a length of

approximately 50 µm and a thickness of approximately 10 µm. The EDXS analyses performed on these platelet crystals confirmed that their composition corresponded to the $Sr_3Ti_2O_7$ phase. Apart from these platelets, a large number of smaller (<1 µm), cubic crystals were also observed. The EDXS analyses confirmed that these small crystals correspond to $SrTiO_3$, which is in agreement with the XRD data.

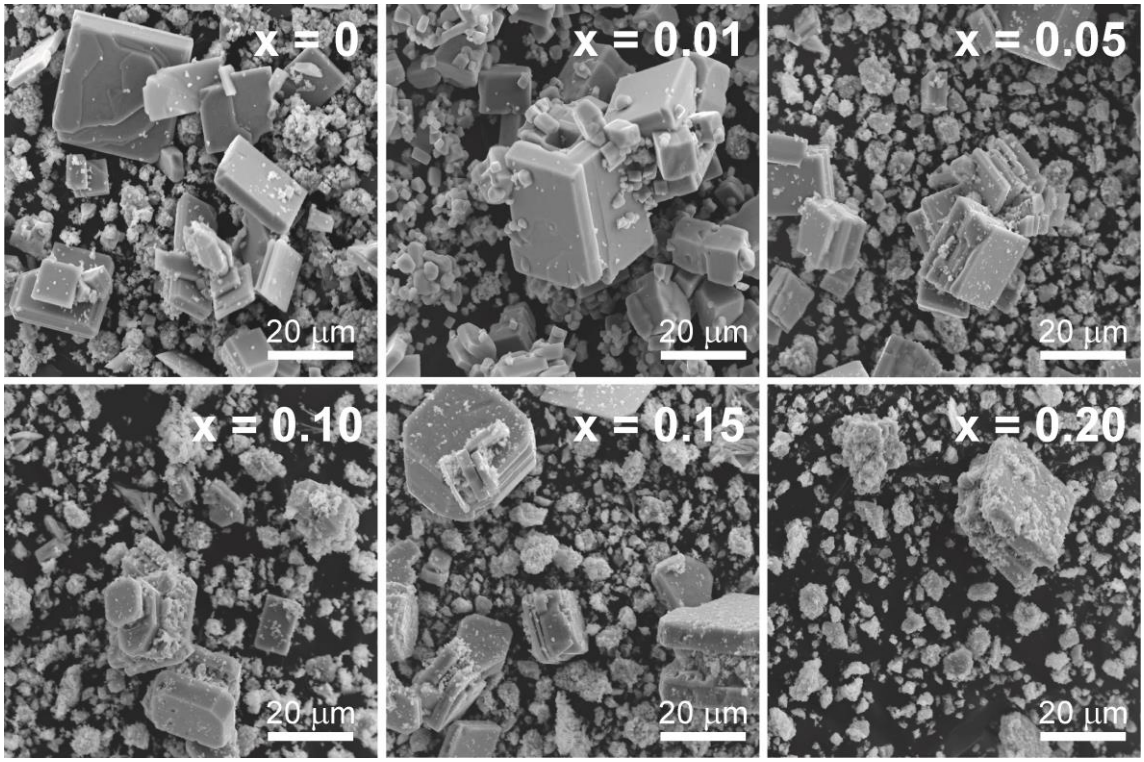


Figure 3: SEM images of MSS product powders with respect to the initial amount of Nb-doping; $Sr_3(Ti_{1-x}Nb_x)_2O_7$; x = 0–0.2.

The small amount of added niobium (x = 0.01) did not have any significant influence on the morphology and the size of the large platelet crystals. However, when adding 5 mol% of Nb (x = 0.05) the platelet crystals became smaller than the pure sample. Also, the platelet crystals became thinner (~ 5 µm). Apart from the small cubic crystals, some irregular shaped particles were also observed, which were determined by the EDXS to be strontium-enriched niobates, most likely $Sr_2(Nb,Ti)O_4$ and/or $Sr_4(Nb,Ti)_2O_9$. An additional increase in the niobium concentration (x > 0.05) had the following effect on the morphology and the size of the MSS product: the number of platelet crystals was smaller, as was their size and thickness. Nicely developed flat crystal facets in the sample $Sr_3Ti_2O_7$ (x = 0) became rougher with an increasing niobium concentration. SEM images of samples with the initial composition $Sr_3(Ti_{1-x}Nb_x)_2O_7$, with X = 0 and x= 0.20, synthesized at 1200, 1250 and 1300°C, can be seen in Figure 4.

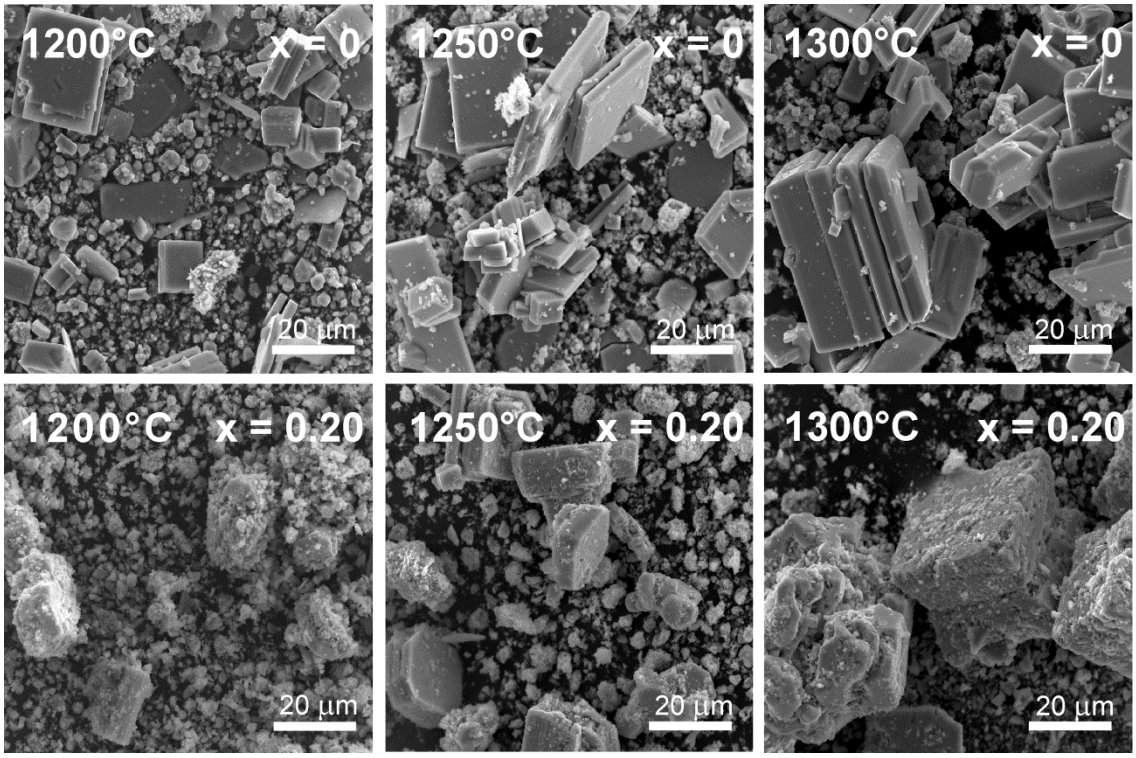


Figure 4: SEM images of $Sr_3(Ti_{1-x}Nb_x)_2O_7$ MSS products with x=0 and x=0.20 synthesized at different temperatures: 1200°C, 1250°C and 1300°C

At all synthesis temperatures the samples with no added niobium (x = 0) contain nicely developed, platelet-like crystals corresponding to $Sr_3Ti_2O_7$. The smaller cubic crystals were again determined to be $SrTiO_3$. With an increase of the synthesis temperature from 1200°C to 1300°C, the size of the platelet crystals increases. Also, the crystals are thicker and usually composed of thicker coupled slabs. The influence of the synthesis temperature on the crystal growth of the platelets is more visible in high niobium-doped $Sr_3(Ti_{1-x}Nb_x)_2O_7$ samples (x = 0.20). At 1200°C, the sample consists mostly of agglomerated nano-sized $Sr(Ti,Nb)O_3$ and platelet $Sr_3(Ti,Nb)_2O_7$ crystals. Rounded, 3–20-µm-sized formations were identified as $Sr_4(Nb,Ti)O_9$. Some not well developed platelet crystals with sizes up to 10 µm were also observed, corresponding to $SrO{*}nSr(Ti,Nb)O_3$ (n = 2, 3). At 1250°C the platelet crystals are larger, reaching up to 50 µm. The round strontium niobate formations grew in size as well, measuring approximately 10 µm. It was concluded that with the temperature increasing, the amount of $Sr_4(Nb,Ti)O_9$ was enhanced, while the formation of the platelet Ruddlesden-Popper phases was inhibited.

In order to determine the content of niobium in the platelet crystals we conducted a more systematic EDXS analysis. The EDXS results were compared to the starting MSS powder compositions and are shown in Table 1. We observed an inverse correlation in the measured concentrations between Ti and Nb, i.e., a lower Ti concentration is accompanied by an increased Nb concentration. We observed a similar correlation also for Sr and Na. It was concluded that while Nb is replacing Ti in the platelet crystals, there is also the substitution of Sr with Na. The latter is due to crystal growth in a

liquid Na-based salt melt. The composition of the platelet crystals can therefore be best described with the following formula that indicates the solid solution $(Sr,Na)_3(Ti,Nb)_2O_7$ [18].

Table 6.1. Results of EDXS analysis of platelet crystals as a function of x in $Sr_3(Ti_{1-x}Nb_x)_2O_7$.

X	Sr (at%)	Ti (at%)	Nb (at%)	Na (at%)	O (at%) By difference
0	22.6±0.2	18.4±0.2	-	-	59.0±0.8
0.01	22.0±0.2	18.5±0.3	0.1±0.1	-	59.6±0.8
0.05	22.4±0.2	17.9±0.2	0.3±0.1	0.4±0.2	59.1±0.8
0.10	23.4±0.2	16.5±0.2	1.0±0.1	0.6±0.2	58.8±0.8
0.15	23.2±0.2	16.1±0.2	1.4±0.1	0.8±0.2	59.1±0.8
0.20	22.1±0.2	16.4±0.2	1.8±0.1	1.0±0.2	59.4±0.8

The increasing amount of Nb in the platelet crystals additionally indicates that it would be possible to synthesize platelets with an even larger Nb content. The amount of Nb detected by the EDXS, as compared to the initial doping, is roughly 50% lower, whereas the remaining Nb apparently triggers the formation of strontium niobates, indicating that the formation enthalpies of the $SrO{*}nSr(Ti_{1-x}Nb_x)O_3$ solid-solution and the Sr_2NbO_4 are similar.

3.3. TEM analysis

A transmission electron microscopy investigation was conducted in order to verify whether the synthesized platelet crystals do in fact exhibit the ordering of SrO single layers, which is expected in the $Sr_3Ti_2O_7$ Ruddlesden-Popper phase. In other words, whether one SrO layer is followed by two perovskite $SrTiO_3$ blocks. Our previous investigations showed that it is very difficult to synthesize ideal, stoichiometric, Ruddlesden-Popper phases using solid-state reactions where the SrO layers and the perovskite blocks alternate in exact ordering [19]. The fact that some Na is replacing Sr and that Nb is replacing Ti in the platelet crystals, as was shown by the EDXS analysis, should not alter and/or influence the ordering sequence in this tetragonal structure. The low-magnification, bright-field TEM image of a cross-section of a $Sr_3(Ti_{0.8}Nb_{0.2})_2O_7$ platelet crystal (Figure 5a) clearly shows that the platelet crystals are composed of more crystal slabs. The orthogonal shape of the crystal was rounded in the area where the sample was ion-milled (Figure 5b).

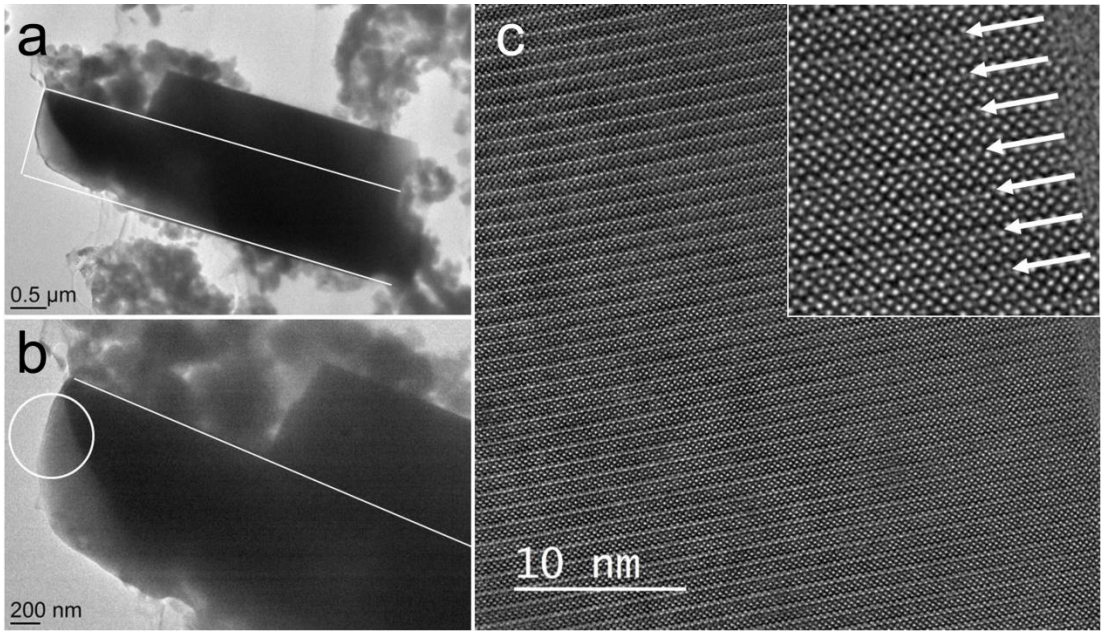


Figure 5: (a) Bright-field TEM micrograph of a cross-section of a platelet crystal. (b) Higher magnification showing thin region for HRTEM. (c) HRTEM showing perfect ordering of SrO layers between two perovskite blocks.

A high-resolution image from this thin region taken in the [010] zone axis clearly shows perfect ordering of the SrO layers along the c axis. The EDX spectrum taken from this ordered region shows that the overall composition corresponds to a formula of approximately $Sr_3(Ti_{0.91}Nb_{0.09})_2O_7$. The result is in good agreement with the EDXS results taken from the platelet crystals in the SEM, where it was shown that the niobium content was approximately 50% lower than the targeted composition. Based on the TEM results it was also concluded that MSS is a very suitable method for the preparation of stoichiometric Ruddlesden-Popper phases.

3.4. Formation mechanism of $Sr_3(Ti_{1-x}Nb_x)_2O_7$ platelet crystals

Liu et al [6] proposed a formation-mechanism model for pure $Sr_3Ti_2O_7$ based MSS: in the first step, $SrCO_3$ and TiO_2 react to form $SrTiO_3$, which is followed by the formation of $Sr_3Ti_2O_7$ in the presence of SrO. Based on the results from this study and the formation mechanism of pure $Sr_3Ti_2O_7$, we concluded that the formation mechanism of Nb-doped $Sr_3Ti_2O_7$ is as follows. The first step is the formation of submicron particles of $SrTiO_3$ and excess SrO from the $SrCO_3$ and TiO_2. Then, some of the SrO reacts with $SrTiO_3$ to form $Sr_3Ti_2O_7$ and some SrO reacts with Nb_2O_5 to form Sr_2NbO_4. Nb_2O_5 does not precipitate in the first step, since it is not soluble in alkali salts [20]. If the initial composition is, like in our case, stoichiometric $Sr_3Ti_2O_7$ (Sr/Ti = 3/2), the main phase in the final product is $SrTiO_3$, since some of the SrO is evaporated during the synthesis. However, if we were to enhance the initial Sr/Ti ratio, probably more $Sr_3(Ti,Nb)_2O_7$ would form, but at the same time also more Sr_2NbO_4. On the other hand Ianculescu et al. [21] reported that Nb does not diffuse directly into the $SrTiO_3$ lattice, but forms strontium niobates in the first stage

and then a $Sr(Ti_{1-x}Nb_x)O_3$ solid solution in the second. Therefore, we could expect a recrystallization of the strontium niobates into a $Sr(Ti_{1-x}Nb_x)O_3$ solid solution using the appropriate synthesis conditions. In summary, the formation mechanism for Nb-doped $Sr_3Ti_2O_7$ can be written as (Eq. 1-3):

$$3SrCO_3 + 2TiO_2 \xrightarrow{CO_2\uparrow} SrTiO_3 + 2SrO \quad (1)$$

$$SrTiO_3 + SrO + Nb_2O_5 \xrightarrow{SrO\uparrow} SrTiO_3 + Sr_3(Ti,Nb)_2O_7 + Sr_2NbO_4 \quad (2)$$

$$SrTiO_3 + Sr_3(Ti,Nb)_2O_7 + Sr_2NbO_4 \longrightarrow Sr_3(Ti,Nb)_2O_7 \quad (3)$$

$SrTiO_3$ in the final product could be avoided by adding excess SrO to the initial $Sr_3Ti_2O_7$ composition. In order to complete this reaction, very long times of the MSS should be applied, much longer times than in our case. Nevertheless, even under our synthesis conditions we were able to introduce enough niobium into the solid solution within the platelet crystals of the Ruddlesden-Popper type to ensure sufficient electrical conductivity that will allow these platelet crystals to be used for phonon scattering in $Sr(Ti,Nb)O_3$-based thermoelectric materials.

4. Conclusion

We have studied the influence of Nb additions on the formation of $Sr_3(Ti_{1-x}Nb_x)_2O_7$ platelet crystals ($0 < x < 0.2$) in a NaCl/KCl flux using the molten salt synthesis (MSS) method. With an increasing synthesis temperature the platelet crystals were larger for both the pure $Sr_3Ti_2O_7$ and the $Sr_3(Ti_{1-x}Nb_x)_2O_7$ solid solutions. However, with increasing content of Nb, the size of the platelet crystals decreased, compared to the pure $Sr_3Ti_2O_7$ platelets. In spite of the initial $Sr_3(Ti_{1-x}Nb_x)_2O_7$ stoichiometry, $SrTiO_3$ was always detected as a secondary phase, which was attributed to the SrO evaporation during the MSS. Additionally, heavy Nb-doping resulted in the formation of $Sr_4(Nb,Ti)_2O_9$ and $Sr_2(Nb,Ti)O_4$ strontium niobates. The EDS analysis confirmed that approximately 50% of the initially added Nb was incorporated into the $Sr_3(Ti_{1-x}Nb_x)_2O_7$ platelet crystals' solid solution, while the remaining Nb was spent for the formation of strontium niobates, which suggests similar formation enthalpies for the $Sr_3(Ti_{1-x}Nb_x)_2O_7$ and strontium niobates. TEM investigations showed that the platelet crystals exhibited ideal ordering of the SrO layers within this Ruddlesden-Popper-type structure, i.e., one SrO layer strictly followed every two $Sr(Ti,Nb)O_3$ perovskite blocks along the c-axis of the platelets. According to the proposed formation mechanism for $Sr_3(Ti_{1-x}Nb_x)_2O_7$, we expect that a higher content of Nb in the $Sr_3(Ti_{1-x}Nb_x)_2O_7$ could be achieved with an extended time for the MSS.

Acknowledgements

The authors would like to thank the Slovenian Research Agency (ARRS) (project number PR-03768) for the financial support and Paul McGuiness for proofreading.

References

1 Ohta, S. *et al.* Large Thermoelectric Performance of Heavily Nb-doped $SrTiO_3$ Epitaxial Film at High Temperature. *Applied Physics Letters* **87**, 092108, doi:doi:http://dx.doi.org/10.1063/1.2035889 (2005).

2 Teranishi, T. *et al.* Thermoelectric Efficiency of Reduced $SrTiO_3$ Ceramics Modified with La and Nb. *Journal of the American Ceramic Society* **96**, 2852-2856, doi:10.1111/jace.12379 (2013).

3 Wang, N., Han, L., He, H., Ba, Y. & Koumoto, K. Effects of Mesoporous Silica Addition on Thermoelectric Properties of Nb-Doped $SrTiO_3$. *Journal of Alloys and Compounds* **497**, 308-311, doi:10.1016/j.jallcom.2010.03.049 (2010).

4 Li, Z., Zhang, X., Hou, J. & Zhou, K. Molten Salt Synthesis of Anisometric $Sr_3Ti_2O_7$ Particles. *Journal of Crystal Growth* **305**, 265-270, doi:http://dx.doi.org/10.1016/j.jcrysgro.2007.04.017 (2007).

5 Akdogan, E. K., Brennan, R., Allahverdi, M. & Safari, A. Effects of Molten Salt Synthesis (MSS) Parameters on the Morphology of $Sr_3Ti_2O_7$ and $SrTiO_3$ Seed Crystals. *J Electroceram* **16**, 159-165, doi:10.1007/s10832-006-6243-2 (2006).

6 Liu, Y.-f., Lu, Y.-n., Xu, M. & Zhoun, L.-f. Formation Mechanisms of Platelet $Sr_3Ti_2O_7$ Crystals Synthesized by the Molten Salt Synthesis Method. *Journal of the American Ceramic Society* **90**, 1774-1779, doi:10.1111/j.1551-2916.2007.01706.x (2007).

7 Toshio Kimura, P. C. S. E. Molten Salt Synthesis of Ceramic Powders, Advances in Ceramics - Synthesis and Characterization. *InTech Processing and Specific Applications*, doi:10.5772/20472 (2011).

8 Yang, R., Cui, L. & Zheng, Y. The Synthesis of Composite Particles in Molten Salts. *Materials Transactions* **47**, 584-586, doi:10.2320/matertrans.47.584 (2006).

9 Seabaugh, M. M. *et al.* Development of a Templated Grain Growth System for Texturing Piezoelectric Ceramics. *Journal of Intelligent Material Systems and Structures* **15**, 209-214, doi:10.1177/1045389x04040131 (2004).

10 Setasuwon, P. & Kijamnajsuk, S. Synthesis of $Na_{0.5}Bi_{0.5}TiO_3$ Anisotropic Particles with Grain Orientation by Conversion of $Na_{0.5}Bi_{4.5}Ti_4O_{15}$ Crystals. *Science and Technology of Advanced Materials* **7**, 780-784, doi:http://dx.doi.org/10.1016/j.stam.2006.10.006 (2006).

11 Zhao, L., Gao, F., Zhang, C., Zhao, M. & Tian, C. Molten Salt Synthesis of Anisometric $KSr_2Nb_5O_{15}$ Particles. *Journal of Crystal Growth* **276**, 446-452, doi:http://dx.doi.org/10.1016/j.jcrysgro.2004.11.388 (2005).

12 Zhang, S., Jayaseelan, D. D., Bhattacharya, G. & Lee, W. E. Molten Salt Synthesis of Magnesium Aluminate ($MgAl_2O_4$) Spinel Powder. *Journal of the American Ceramic Society* **89**, 1724-1726, doi:10.1111/j.1551-2916.2006.00932.x (2006).

13 Li, Z., Zhang, S. & Lee, W. E. Molten Salt Synthesis of $LaAlO_3$ Powder at Low Temperatures. *Journal of the European Ceramic Society* **27**, 3201-3205, doi:http://dx.doi.org/10.1016/j.jeurceramsoc.2007.01.008 (2007).

14 Kan, Y. *et al.* Anisotropic Grain Growth of $Bi_4Ti_3O_{12}$ in Molten Salt Fluxes. *Materials Research Bulletin* **38**, 567-576, doi:http://dx.doi.org/10.1016/S0025-5408(03)00029-1 (2003).

15 Ruddlesden, S. N. & Popper, P. The Compound $Sr_3Ti_2O_7$ and its Structure. *Acta Crystallographica* **11**, 54-55, doi:doi:10.1107/S0365110X58000128 (1958).

16 Barna, Á., Pécz, B. & Menyhard, M. TEM Sample Preparation by Ion Milling/Amorphization. *Micron* **30**, 267-276, doi:http://dx.doi.org/10.1016/S0968-4328(99)00011-6 (1999).

17 Šturm, S., Rečnik, A. & Čeh, M. Microstructure Evolution in $SrTiO_3$ with Different Sr/Ti ratios. *Materials and Technology* **33** (1999).

18 Villars, P. *et al.* in *Structure Types. Part 10: Space Groups (140) I4/mcm – (136) P42/mnm* Vol. 43A10 *Landolt-Börnstein - Group III Condensed Matter* (eds P. Villars & K. Cenzual) Ch. 401, 483-483 (Springer Berlin Heidelberg, 2011).

19 Šturm, S., Rečnik, A. & Čeh, M. Nucleation and Growth of Planar Faults in SrO-Excess $SrTiO_3$. *Journal of the European Ceramic Society* **21**, 2141-2144, doi:http://dx.doi.org/10.1016/S0955-2219(01)00189-3 (2001).

20 G. Picard, P. B. The Niobium Chemistry in Molten LiCl+KCl Eutectic. *Materials science forum* **73-75**, 505-512, doi:10.4028/www.scientific.net/MSF.73-75.505 (1991).

21 Ianculescu, A. *et al.* Formation and Properties of Some Nb-Doped $SrTiO_3$-Based Solid Solutions. *Journal of Thermal Analysis and Calorimetry* **72**, 173-180, doi:10.1023/a:1023975904764 (2003).

Chapter 7

An Enhanced Thermoelectric Figure of Merit for $Sr(Ti_{0.8}Nb_{0.2})O_3$ Based on RP-Polytype Induced Microstructure

In this chapter, a paper entitled "An Enhanced Thermoelectric Figure of Merit for $Sr(Ti_{0.8}Nb_{0.2})O_3$ Based on RP-Polytype Induced Microstructure" [84] by Marja Jerič, Johannes de Boor, Boštjan Jančar, and Miran Čeh is presented.

In this study microstructural aspects of STNO with the addition of platelet RP-type seeds and moreover its influence on thermoelectric properties were investigated. Even though Nb-doped RP-type seeds were successfully synthesized by the molten salt synthesis, the resulting powder made in this manner consisted of a significant amount of strontium niobates phases, therefore undoped RP-type platelet seeds were chosen as more appropriate to be added to STNO to avoid formation of undesired secondary phases. It was expected that the platelet seeds would induce growth of RP-type grains and consequently enhance phonon scattering at the faults.

The study revealed that the planar faults were successfully introduced into the STNO matrix. Thermoelectric measurements showed that the thermal conductivity was slightly lowered in the seeded STNO in comparison to pure STNO. Contrary to our expectation, electrical conductivity of seeded STNO was significantly increased while the Seebeck coefficient was practically unchanged, which resulted in improved ZT by 50% of seeded STNO at 650 °C. This trade-off was connected to the formation of highly conductive local paths in the seeded STNO which enhanced the electrical transport. Although these paths are most probably generally connected to the direction of the planar faults, the interconnectivity of faults, despite their random orientation, also plays a major role in increased conductivity.

In conclusion, introducing RP-type faults into the STNO via seeding has shown to be a promising approach in order to not only lower thermal conductivity, but mostly to enhance the power factor.

Journal of the European Ceramic Society 36 (2016) 1177–1182

Contents lists available at www.sciencedirect.com

Journal of the European Ceramic Society

journal homepage: www.elsevier.com/locate/jeurceramsoc

An enhanced thermoelectric figure of merit for $Sr(Ti_{0.8}Nb_{0.2})O_3$ based on a Ruddlesden–Popper-polytype-induced microstructure

Marja Jerič[a,b,*], Johannes de Boor[c], Boštjan Jančar[a], Miran Čeh[a]

[a] Jožef Stefan Institute, Ljubljana, Slovenia
[b] Jožef Stefan International Postgraduate School, Ljubljana, Slovenia
[c] Institute of Materials Research, German Aerospace Center, Cologne, Germany

ARTICLE INFO

Article history:
Received 7 September 2015
Received in revised form
19 November 2015
Accepted 5 December 2015
Available online 17 December 2015

Keywords:
Thermoelectric materials
Nb-doped $SrTiO_3$
Ruddlesden–Popper polytypes
Seed crystals
Molten-salt synthesis

ABSTRACT

Platelet crystals based on Ruddlesden–Popper (RP) polytypes prepared by molten-salt synthesis were used to influence the microstructural development of Nb-doped $SrTiO_3$ (STO;Nb) perovskite and, consequently, to change the thermoelectric properties. Electron microscopy revealed intergrowth of RP-polytypic phases within the STO;Nb solid-solution matrix phase. The morphology of the grains varied from isotropic to anisotropic, containing polytypic faults up to 100 μm in length. Such a microstructure increased the thermoelectric figure of merit by 50% at 650 °C, due to substantially enhanced electrical conductivity, slightly increased Seebeck coefficient and lowered thermal conductivity.

© 2015 Elsevier Ltd. All rights reserved.

1. Introduction

$SrTiO_3$ (STO) perovskite is a promising candidate for n-type high-temperature thermoelectric materials [1,2] since it is stable at elevated temperatures (>1000 °C), in contrast to the common non-oxide thermoelectrics [3] used in thermoelectric generators. The thermoelectric properties of a material are described by the dimensionless thermoelectric figure of merit (ZT), given by the following equation:

$$ZT = \frac{\sigma \times S^2}{\kappa} T \quad (1)$$

where σ denotes the electrical conductivity [S/cm], S is the Seebeck coefficient [V/K], κ is the thermal conductivity [W/Km], and T is the absolute temperature [K] of the material. Up to date, the best ZT at ~1000 K for STO thermoelectrics is reported to be 0.37 for 20% Nb-doped STO epitaxial films [4], 0.37 for bulk La-doped STO [5] and 0.35 for bulk 20% Nb-doped STO [6]. The ZT of oxide materials is usually far below 1, which is considered to be the threshold value for practical applications. The reason for the inherently low ZT of oxide materials is partly their high lattice thermal conductivity (κ), which is associated with the lattice vibrations of the low-atomic-weight oxygen [7]. In order to significantly increase the ZT value, the κ should be as low as possible, coupled with high σ and S, as can be seen from Eq. (1).

One of the possibilities for reducing the high κ is to incorporate ordered and/or partly ordered layered structures into the thermoelectric material that would enhance the phonon scattering and consequently reduce the lattice κ of the material, which is a predominant component of the thermal transport in semiconductors [3]. The structural interfaces are expected to scatter phonons to a greater extent than the electrons, thus resulting in an improved ZT. Furthermore, by introducing layered structures into a bulk material, additional favorable effects, such as the filtering of low-energy electrons and quantum-confinement effects, can take place, thereby increasing the power factor of the material. The energy-filtering effect occurs at the interfaces that preferentially scatter low-energy electrons, thus eliminating their negative contribution to the Seebeck coefficient and, consequently, increasing the power factor. The spatial confinement of the electrons leads to an increased density of states near the Fermi level, which also results in an enhancement of the Seebeck coefficient [8–10].

Recent attempts to lower the thermal conductivity of Nb-doped STO (STO;Nb) include combining bulk materials with low-thermal-conductivity constituents such as mesoporous silica (ZT = 0.17 at 900 K) [11], glass-forming oxides (SiO_2, B_2O_3) (ZT = 0.001 at 923 K) [12], and yttria-stabilized-zirconia nano-inclusions (ZT = 0.21 at

* Corresponding author at: JSI Institute, Jamova cesta 39, 1000 Ljubljana, Slovenia.
E-mail address: marja.jeric@ijs.si (M. Jerič).

http://dx.doi.org/10.1016/j.jeurceramsoc.2015.12.001
0955-2219/© 2015 Elsevier Ltd. All rights reserved.

900 K) [13]. On the other hand, Lee et al. [14] successfully reduced the thermal conductivity in Nb-doped natural superlattices of $SrO/(SrTiO_3)_n$ ($n = 1, 2$) due to phonon scattering on the $SrO/(SrTiO_3)$ interfaces; however, in comparison with STO the electrical conductivity was lowered as well, resulting in a ZT of 0.14 at 1000 K. Following this basic idea we modified the microstructure of 20% Nb-doped $SrTiO_3$ by incorporating Ruddlesden–Popper (RP) polytipic phases [15] in the form of platelet seeds to serve as a phonon-scattering structural feature, thus reducing the lattice's thermal conductivity.

A STO;Nb solid solution with the general formula $Sr(Ti_{1-x}Nb_x)O_3$ exhibits a distorted cubic perovskite structure in which the Ti and Nb randomly occupy the B sites. In order to introduce layered structures into such a material, a similar chemical composition and crystal structure should be chosen, which would allow the coexistence of both phases/structures, i.e., like in the case of topotactical intergrowth. Also, the incorporation of such similar structures could possibly minimize the formation of undesired secondary phases that would adversely affect the thermoelectric properties of the material. Based on these requirements, an apparent choice for a layered-structured phase that could be added to the $Sr(Ti_{1-x}Nb_x)O_3$ solid solution is one of the RP-polytypic phases, which are described as $SrO \times nSrTiO_3$ ($n = 1, 2, 3\ldots$) [15]. These homologous compounds only differ in terms of the number of perovskite blocks that are interleaved with the SrO layers that have a rock-salt-type crystal structure. In order to incorporate a structurally and chemically similar phase compared to the STO;Nb solid solution, we chose to incorporate platelet crystals of the $SrO \times 2SrTiO_3$, i.e., $Sr_3Ti_2O_7$, which can be synthesized in the form of micron-size platelet seed crystals using molten-salt synthesis [16–18].In RP structures, the $SrTiO_3$ cubic perovskite blocks are interleaved with a single SrO planar fault. The stacking/ordering of the SrO planar faults in these structures occurs along the [0 0 1] perovskite direction. Any deviation from the RP-polytype stoichiometry, i.e., depletion of the SrO, results in disordered sequences of SrO planar faults and an increased number of perovskite blocks between the SrO layers. The growth of RP-polytype crystals during MSS is much faster in the [1 0 0] and [0 1 0] directions compared to the [0 0 1] direction, which results in the formation of platelet-like crystals. This is why the RP-type platelet crystals have pronounced {0 0 1} facets. One of the additional advantages of incorporating RP-polytype platelet crystal seeds into $Sr(Ti_{1-x}Nb_x)O_3$-based ceramics is the possibility of triggering exaggerated anisotropic grain growth during the sintering, which results in textured microstructures and a decreased surface of the grain boundaries. In our work we report on the synthesis of RP-polytype crystal seeds, and on the microstructural development and thermoelectric properties of the seeded STO;Nb.

2. Experimental procedures

The STO;Nb solid solution was prepared by conventional solid-state synthesis. The $SrCO_3$ (Sigma–Aldrich), TiO_2 (Alfa Aesar) and Nb_2O_5 (Merck) starting powders were mixed corresponding to the $Sr(Ti_{0.8}Nb_{0.2})O_3$ stoichiometry, homogenized and calcined twice at 1200 °C for 12 h. The calcined material was then crushed and milled in a planetary mill for 1 h in order to obtain the starting powder that was used in all the subsequent sintering experiments.

The RP-polytype platelet seeds that were added to the starting STO;Nb material were synthesized by molten-salt synthesis (MSS), which is described in detail elsewhere [16]. The starting $SrCO_3$ (Sigma–Aldrich) and TiO_2 (Alfa Aesar) powders were mixed in a 1:1 weight mixture of NaCl (Merck) and KCl (Merck). The initial stoichiometry of the RP-polytype was $Sr_3Ti_2O_7$ ($SrO \times 2SrTiO_3$). The starting $SrCO_3$ and TiO_2 powder mixtures with NaCl and KCl salts were first dissolved in absolute ethanol and homogenized in a planetary mill for one hour. The slurry was dried at 80 °C. Dry powders and salts were then sealed in several alumina crucibles to avoid any leakage of the molten salts. The crucibles were heated at different temperatures in a chamber furnace, i.e., at 1200 °C, 1250 °C and 1300 °C, for 4 h, to study the crystals' development with different temperatures. After the reaction, the products were put in hot distilled water to dissolve the salts, followed by centrifugation of the suspension at 5500 rpm for 10 min. The water with dissolved salts was poured out, whereas the sediment was washed in this manner an additional three times for the complete removal of the salts. After washing, the product powder was dried at 80 °C.

The calcined STO;Nb powder was uniaxially cold-pressed into pellets and sintered in a hydrogen atmosphere for 3 h at 1500 °C, with heating and cooling rates of 15 °C/min. In order to introduce a layered structured phase into the basic STO;Nb composition, 10 w% of the MSS product powder with RP-polytype crystal seeds was added to the initial STO;Nb powder in an agate mortar. After careful mixing, the mixture of STO;Nb and MSS powder containing platelet seeds was uniaxially cold-pressed into pellets and sintered under the same conditions as the STO;Nb.

X-ray diffraction (XRD; D4 Endeavor, Bruker AXS, Karlsruhe, Germany) with the Bragg–Bretano geometry, Cu-Kα radiation, and a Sol-X energy-dispersive detector was used to monitor the completion of the reaction and to identify the phases during the sintering process. The microstructural analysis was carried out using scanning electron microscopy (SEM) (Jeol JSM-5800, Jeol JSM-7600F) with energy-dispersive X-ray spectroscopy (EDXS) (Oxford Instruments Isis 300, Oxford Instruments INCA) and transmission electron microscopy (CTEM, HRTEM) (Jeol JEM-2100, Jeol JEM-2010F) with energy-dispersive X-ray spectroscopy (Jeol JED, Oxford Isis 300). The sintered pellets were cut perpendicular to the pressing direction, polished and chemically etched for the SEM microstructural analysis. All the samples were coated with a few-nm-thick carbon coating in order to ensure electrical conductivity. The thin foils for the TEM observations from the bulk materials were prepared using ion-milling techniques (Gatan, PIPS).

The STO;Nb and seeded STO;Nb were characterized with respect to their thermoelectric properties. The thermal diffusivity measurement was carried out employing a commercial Laser Flash Apparatus (LFA, 427, Netzsch Gerätebau, Selb, Germany). The specific heat was determined using DSC (Netzsch) and the density was determined by the Archimedes method. The value of κ was calculated using $k(T) = a(T) \times c_p(T) \times \rho(T)$, where k is the thermal conductivity, a is the thermal diffusivity, c_p is the specific heat and ρ is the density of the material. Temperature-dependent S and σ measurements were carried out in a custom-built setup in a He atmosphere [19]. The electrical conductivity was determined by employing a four-probe, in-line geometry and the Seebeck coefficients were determined using a variable temperature gradient to account for any undesired voltage offsets. The measurement accuracy was estimated to be 8% for κ, 5% for σ and 5% for S, based on an intra-laboratory comparison and the data analysis described elsewhere [20].

3. Results and discussion

3.1. Synthesis of platelet seeds

The XRD patterns of the materials obtained after the heat treatment of the starting powders mixtures by the MSS at 1200 °C, 1250 °C and 1300 °C show that after slow cooling all the samples contained more than one phase, irrespective of the synthesis temperature (Fig. 1). The sample synthesized at 1200 °C, in addition to $Sr_3Ti_2O_7$, also contained some $SrTiO_3$ and non-reacted $SrCO_3$. With increasing temperature the content of the $SrTiO_3$ and $SrCO_3$ phases

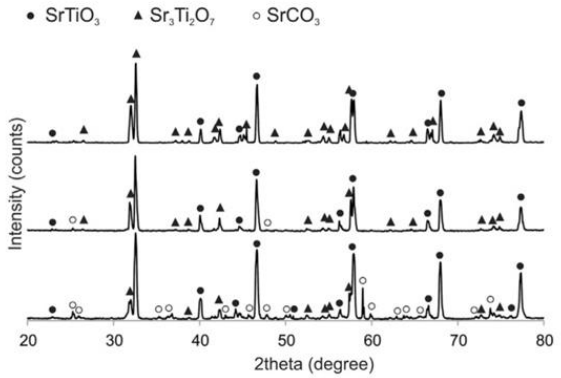


Fig. 1. XRD patterns of molten-salt synthesis product powders synthesized at 1200, 1250 and 1300 °C.

decreased, while the content of the $Sr_3Ti_2O_7$ phase increased. We concluded that the reaction was nearly completed at the highest synthesis temperature of 1300 °C, and that the remaining excess of $SrCO_3$ (SrO) and $SrTiO_3$ would react completely to form RP phases after a longer annealing time.

Regardless of the synthesis temperature, all the product powders consisted of orthogonal, square, platelet crystals with edges up to 50 μm long and agglomerated, nano-sized crystals (Fig. 2). The EDXS analysis confirmed that the large, orthogonal, platelet-like crystals are Sr-enriched RP-polytype phases, while the agglomerated, nano-sized crystals are $SrTiO_3$. All the RP-polytype platelets have very well developed {0 0 1} facets. With increasing temperature, the platelets become thicker and larger.

3.2. $Sr(Ti_{8}Nb_{0.2})O_3$ (STO;Nb) and seeded $Sr(Ti_{0.8}Nb_{0.2})O_3$ (seeded STO;Nb)

3.2.1. XRD

The XRD patterns of STO;Nb and seeded STO;Nb sintered in a hydrogen atmosphere at 1500 °C for 3 h can be seen in Fig. 3a and b, respectively. The observed diffraction peaks of both samples can be indexed according to the Pm3m cubic perovskite structure [21] $SrTiO_3$, which indicates that the STO;Nb solid solution was readily formed in both samples without any secondary phases during the sintering.

The XRD pattern of the seeded STO;Nb reveals no diffraction peaks corresponding to the RP-polytype phases indicating that the excess SrO from the $Sr_3Ti_2O_7$ platelets was mainly used to form RP faults within STO;Nb grains instead of forming individual RP-polytype phases.

3.2.2. SEM and EDXS analysis

Fig. 4 shows the SEM images of STO;Nb and seeded STO;Nb. The grain size and grain shape can be readily observed from the secondary-electron micrographs of the etched surfaces of STO;Nb (Fig. 4a) and seeded STO;Nb (Fig. 4b). The grains of STO;Nb are isotropic in shape and range from 5 to 30 μm in size. Apart from the porosity, regions containing pull-outs can also be observed. On the other hand, the etched surface of seeded STO;Nb clearly reveals the intergrowth of the RP-polytypic phase within the STO;Nb solid-solution matrix phase. Due to the higher SrO content within the polytypic phase, it is etched faster than the matrix phase. The observed planar faults can reach up to 100 μm in length. The grains containing these planar faults are anisotropic in shape reaching the length of the planar faults, while the grains with no faults are isotropic and smaller (~20 μm). Similar anisotropic grain growth induced by RP-faults was observed in SrO-doped $SrTiO_3$ ceramics by Šturm et al [22].

Back-scattered electron micrographs of the polished STO;Nb sample surface showed uniform contrast, indicating that the material is homogeneous in terms of composition on the micron and sub-micron scales. On the other hand, the back-scattered SEM micrograph of polished surface of seeded STO;Nb sample clearly reveals two regions with different contrast, i.e., a dark matrix-phase region and brighter elongated regions (Fig. 4b-inset). According to the EDXS analysis, the brighter regions correspond to RP-polytypic phase/platelets with a varying Nb content embedded into the darker STO;Nb solid-solution matrix. The amount of the RP-polytypic phases was however below the detectable limit of XRD (Fig. 3b).

3.2.3. TEM analysis

Transmission electron microscopy was used for more detailed information about the microstructure on the nano-scale. TEM of the STO;Nb sample (Fig. 4c) revealed no additional structural features within the individual STO;Nb grains. The grain boundaries and triple junctions were clean, with no observable interface phases. The EDXS point analysis performed on different grains confirmed that the measured chemical composition corresponded to the initial stoichiometric molar ratio in the $Sr(Ti_{0.8}Nb_{0.2})O_3$, which is Sr:Ti:Nb:O = 20:16:4:60. The TEM micrograph of the seeded STO;Nb sample from the region of the RP-polytipic phase/platelets in Fig. 4d reveals a more-or-less random ordering of the SrO-type planar faults within the cubic STO;Nb matrix.

3.2.4. Thermoelectric measurements

The results of the thermoelectric measurements for the pure STO;Nb and for seeded STO;Nb are shown in Figs. 5 and 6. The κ value of the STO;Nb is reduced from 9.9 W/mK at room temperature to 5.0 W/mK at 650 °C. In contrast, the κ value of the seeded STO;Nb is 9.1 W/mK at room temperature and 4.7 W/mK at 650 °C. Thus, the

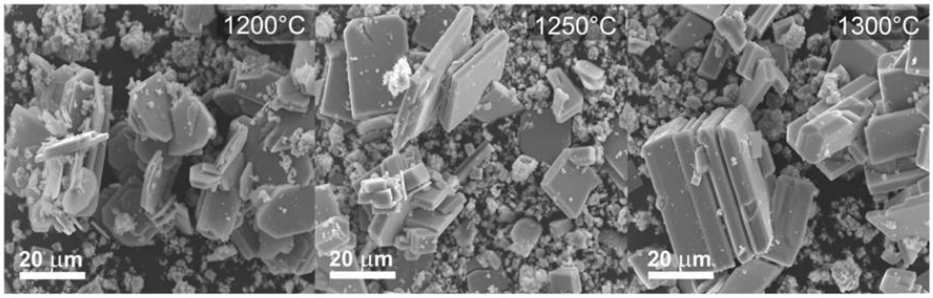


Fig. 2. SEM micrographs of MSS product powder synthesized by molten-salt synthesis at 1200, 1250 and 1300 °C.

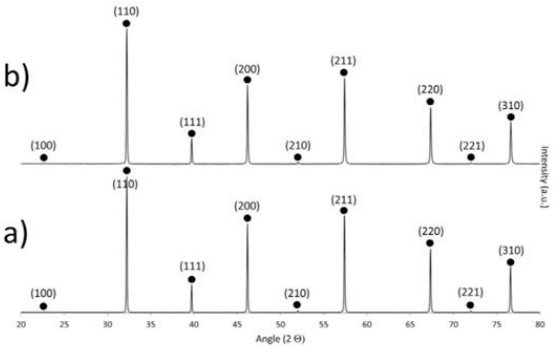


Fig. 3. XRD patterns of (a) STO;Nb and (b) seeded STO;Nb. All the observed diffraction peaks of both samples can be assigned to the $SrTiO_3$-perovskite structure, thus confirming the complete STO;Nb solid-solution formation.

κ value of the seeded STO;Nb is slightly reduced across the whole temperature range (Fig. 5a). The measured κ is the total κ, which is in fact composed of two contributions: the electrical κ_e due to the movement of carriers and the lattice κ_L due to phonons. To estimate the lattice and the electronic contributions to the total κ, the κ_e was calculated using the Wiedemann–Franz law [23] (Eq. (2)):

$$\kappa_e = LT\sigma \tag{2}$$

where L is the theoretical Lorenz factor calculated by applying the free-electron theory (2.45×10^{-8} WΩ/K^2), T is the temperature and σ is the electrical conductivity. The κ_L is then (Eq. (3)):

$$\kappa_L = \kappa_{tot} - \kappa_e \tag{3}$$

The calculated values are presented in Fig. 5b and c. A large contribution of the κ_L (98%) to the κ_{tot} is clearly evident. In addition, the decrease of κ with increasing temperature suggests a phonon-dominated thermal conduction in both samples. At room temperature the κ_L value of STO;Nb is 9.7 W/mK, whereas the κ_L value of seeded STO;Nb is 8.57 W/mK. In comparison with the STO;Nb, the κ_L value of seeded STO;Nb is visibly lowered at lower temperatures, whereas at higher temperatures the lower κ_L of seeded STO;Nb is less obvious. The lowered κ_L of the seeded STO;Nb could be attributed to phonon scattering at the $SrO/Sr(Ti_{1-x}Nb_x)O_3$ internal interfaces, like in the case of thermoelectric ceramics consisting exclusively of Nb-doped RP phases, as reported by Lee et al. [14]. With increasing temperature, the phonon scattering of the $SrO/Sr(Ti_{1-x}Nb_x)O_3$ internal interfaces becomes negligible; therefore, we observe similar values of κ_L at higher temperatures. On the other hand, the κ_e value in the seeded STO;Nb is increased across the whole temperature range, probably due to the enhanced electron mobility. However, the κ_e contribution to the κ_{tot} is minor (2%); therefore, it does not significantly influence the κ_{tot}.

Fig. 6a shows the significant difference in σ between the STO;Nb and seeded STO;Nb. We observe different temperature-dependent behavior as well as increased values of σ in the sample STO;Nb with seeds, especially at lower temperatures. The seeded STO;Nb exhibits a metallic-like temperature dependence of σ across the whole temperature range; it drops from 783 S/cm at room temperature to 382 S/cm at 650 °C. On the other hand, the σ for the STO;Nb

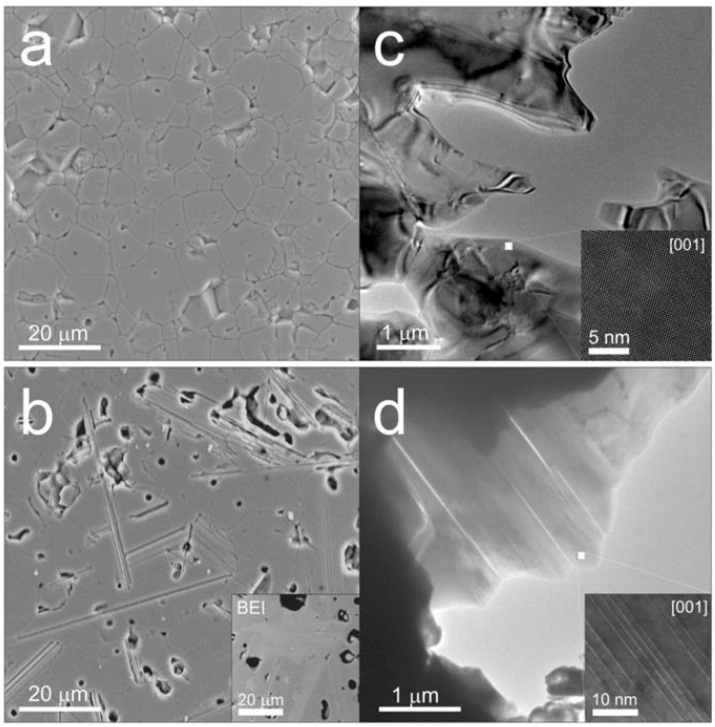


Fig. 4. Secondary-electron micrographs of etched surfaces of (a) STO;Nb revealing isotropic grains and (b) seeded STO;Nb, revealing anisotropic grains and planar faults. The inset shows the back-scattered image (BEI), with secondary phases visible. TEM micrographs of a (c) grain of STO;Nb and (d) isotropic grain of seeded STO;Nb revealing disordered planar faults in a solid-solution perovskite matrix, as seen in the [0 0 1] direction.

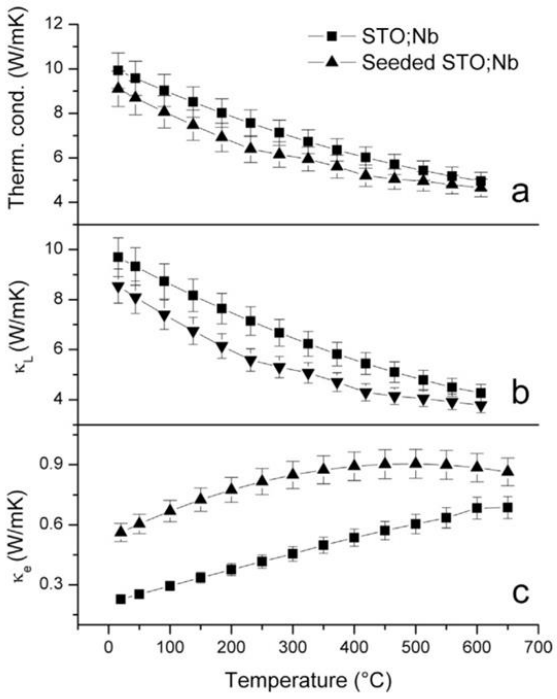


Fig. 5. (a) Thermal conductivity (κ_{tot}), (b) lattice thermal conductivity (κ_L) and (c) electrical thermal conductivity (κ_e) of STO;Nb and seeded STO;Nb.

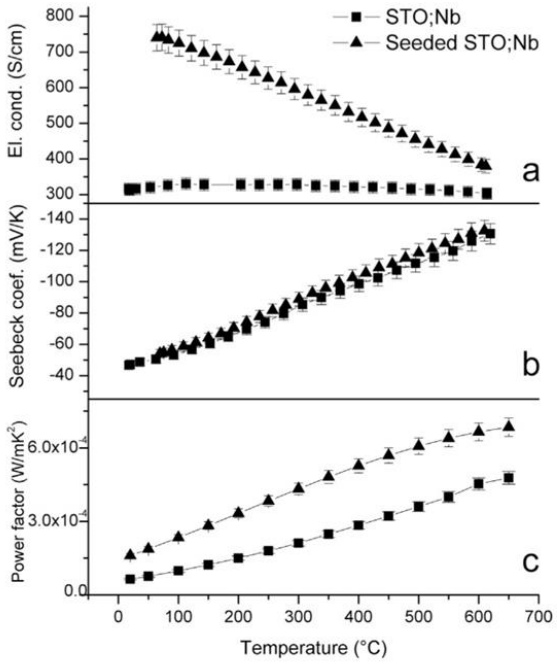


Fig. 6. (a) Electrical conductivity, (b) Seebeck coefficient and (c) power factor of STO;Nb and seeded STO;Nb.

sample does not change substantially with temperature, it reaches 317 S/cm at room temperature and drops to 304 S/cm at 650 °C. However, in the STO;Nb, a change from semiconducting to metallic behavior can be seen at ~200 °C. A similar change in the electrical conductivity behavior was reported for STO;Nb at 200 °C [24] and Nb/La-doped STO [25].

The negative *S* for STO;Nb and for seeded STO;Nb (Fig. 6b) indicates an n-type thermoelectric material, where the charge carriers are electrons. The *S* values for both samples increase linearly with the increasing temperature and *S* values for both samples reach ~−130 μV/K at 650 °C. These *S* values for STO;Nb are comparable with previous reports [13,24].

As seen from the thermoelectric measurements results there is an obvious trade-off between σ and *S* values of STO;Nb and seeded STO;Nb. Whereas the *S* for both samples is comparable, a significant enhancement of σ in seeded STO;Nb can be observed, reaching more than twice the value of STO;Nb. The power factor (PF) (Fig. 6c) of the seeded STO;Nb is therefore improved in whole temperature range due to the increased σ with no decrease in *S*. The PF for the pure STO;Nb reaches 4.8×10^{-4} W/mK^2 at 650 °C, whereas the PF for the seeded STO;Nb is 6.9×10^{-4} W/mK^2 at 650 °C. Similar kind of trade-offs between σ and *S* have recently been observed in boron carbide, $RB_{22}C_2N$, $RB_{17}CN$ and $YB_{22}C_2N$ systems by fabricating nanocomposites boron carbide/$TiB_2$$RB_{22}C_2N$/$RB_4$ [26], $RB_{17}CN$/RB_4, RB_6 [27] and $YB_{22}C_2N$/VB_2 [28,29] where they observed enhanced power factors either due to simultaneous increase in σ and *S* or due to substantial enhanced σ with just a minor degradation of the *S*. This trade-off was just recently clarified in $YB_{22}C_2N$/VB_2 system by Mori and Hara [29], where the authors suggested that nanoweb of conductive paths, caused by metallic seeding results in enhancement of σ without disturbing *S*. In the case of seeded STO;Nb, we observed significantly enhanced σ with a slightly increased *S*, therefore we could link this phenomenon based on the references mentioned above to formation of some kind of conductive paths in the material. The enhanced σ with a slight increase of *S* in the seeded STO;Nb anticipates a strong electron mobility effect. This is also in agreement with enhanced κ_e of seeded STO;Nb (Fig. 5c) discussed before. Kozuka et al. [30] reported that the electron mobility of STO;Nb next to the insulating STO layers is six times larger than in the bulk STO;Nb and also that a significant number of conduction electrons lay outside of the doped layer, giving a conduction path in the surrounding, undoped $SrTiO_3$. Based on these findings, we can expect strongly enhanced electron mobility in the nano-regions next to the isolated RP planar faults which are up to 100 μm long in some STO;Nb grains and up to 50 μm in Nb-doped RP-type grains leading to metallic-like conductivity. Also, we can also expect some conductive electrons in the SrO planar faults region, resulting in not significantly disturbed σ perpendicular to the planar faults. Nevertheless, isolated RP planar faults are known to penetrate into the surrounding STO grains [22], which was also observed in the seeded STO;Nb (Fig. 4b). In this way, RP-faults additionally serve as conductivity paths for electrons and lower the electron-scattering between grain boundaries. Additionally, the overall enhanced grain size in seeded STO;Nb decreased the absolute number of grain boundaries which reduced the interface scattering of electrons, and further contributed to the increased electron mobility, in agreement with the report of Wang et al. [13].

The measured κ, σ and *S* values were used to calculate the figure of merit (ZT) (Fig. 7). At 650 °C ZT reaches a value of 0.09 for the pure STO;Nb and 0.14 for the seeded STO;Nb. Therefore, in comparison with pure STO;Nb the ZT for the seeded STO;Nb is improved by 50% at 650 °C; this is mainly due to the strongly enhanced σ with slightly increased *S*, and moderately decreased κ of seeded STO;Nb.

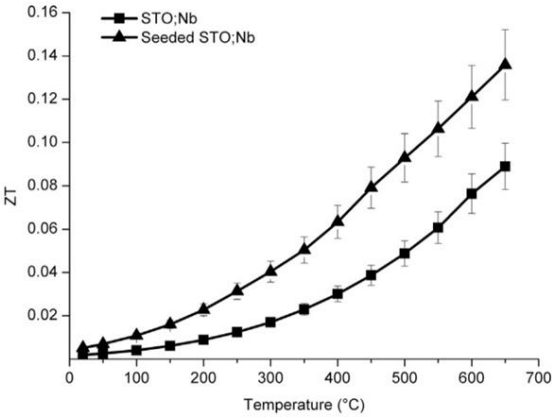


Fig. 7. Figure of merit (ZT) of STO;Nb and seeded STO;Nb.

4. Conclusion

The synthesis, microstructure evolution and thermoelectric properties of STO;Nb and seeded STO;Nb were studied using various analytical techniques. The STO;Nb was successfully synthesized using a conventional solid-state reaction procedure, whereas the RP-polytype platelet crystal seeds were synthesized by a molten-salt synthesis. The addition of platelet seeds to the STO;Nb starting composition significantly modified the microstructure of the STO;Nb sintered bodies. The κ of the seeded STO;Nb was slightly decreased, probably due to phonon scattering at the $SrO/Sr(Ti_{0.8}Nb_{0.2})O_3$ interfaces. The observed strong increase in the electrical conductivity σ for the seeded STO;Nb, as compared to STO;Nb and coupled with a slightly enhanced S, was attributed to formation of conductive paths in nano-regions and overall increased grain size in seeded STO;Nb leading to enhanced electron mobility. Finally, it was determined that the seeding of the STO;Nb solid solution improved the thermoelectric figure of merit ZT by approximately 50% at 650 °C: the ZT at 650 °C increased from 0.09 for STO;Nb to 0.14 for seeded STO;Nb.

Acknowledgements

The authors would like to thank Slavko Bernik for useful discussions on the thermoelectric measurements. Also, the authors would like to thank Silvo Zupančič for technical assistance in high-temperature sintering, Medeja Gec and Andreja Šestan for TEM sample preparation, Janez Zavašnik for the TEM investigations and Werner Schönau for thermal conductivity measurements. We thank Paul McGuiness for proofreading.

This work is financially supported by the Slovenian Research Agency (ARRS), project no. PR-03768.

References

[1] K. Koumoto, R. Funahashi, E. Guilmeau, Y. Miyazaki, A. Weidenkaff, Y. Wang, C. Wan, Thermoelectric ceramics for energy harvesting, J. Am. Ceram. Soc. 96 (2013) 1–23.
[2] J.W. Fergus, Oxide materials for high temperature thermoelectric energy conversion, J. Eur. Ceram. Soc. 32 (2012) 525–540.
[3] C.P. Godart, A. Gonçalves, E.B. Lopes, B. Villeroy, in: Veljko Zlatić, AlexC Hewson (Eds.), Properties and Applications of Thermoelectric Materials. NATO Science for Peace and Security Series B: Physics and Biophysics, Springer, Netherlands, 2009, pp. 19–49 (Chapter 2).
[4] S. Ohta, T. Nomura, H. Ohta, M. Hirano, H. Hosono, K. Koumoto, Large thermoelectric performance of heavily Nb-doped $SrTiO_3$ epitaxial film at high temperature, Appl. Phys. Lett. 87 (2005) 092108.
[5] A. Kikuchi, N. Okinaka, T. Akiyama, A large thermoelectric figure of merit of La-doped $SrTiO_3$ prepared by combustion synthesis with post-spark plasma sintering, Scr. Mater. 63 (2010) 407–410.
[6] S. Ohta, H. Ohta, K. Koumoto, Grain size dependence of thermoelectric performance of Nb-doped $SrTiO_3$ polycrystals, J. Ceram. Soc. Jpn. 1140 (2006) 102–105.
[7] R. Keyes, High-temperature thermal conductivity of insulating crystals: relationship to the melting point, Phys. Rev. 115 (1959) 564–567.
[8] M.S. Dresselhaus, G. Chen, M.Y. Tang, R.G. Yang, H. Lee, D.Z. Wang, Z.-F. Ren, J.-P. Fleurial, P. Gogna, New directions for low-dimensional thermoelectric materials, Adv. Mater. 19 (2007) 1043–1053.
[9] D. Vashaee, A. Shakouri, Improved thermoelectric power factor in metal-based superlattices, Phys. Rev. Lett. 92 (2004), 106103.
[10] L. Hicks, M. Dresselhaus, Effect of quantum-well structures on the thermoelectric figure of merit, Phys. Rev. B 47 (1993) 12727–12731.
[11] N. Wang, L. Han, H. He, Y. Ba, K. Koumoto, Effects of mesoporous silica addition on thermoelectric properties of Nb-doped $SrTiO_3$, J. Alloys Compd. 497 (2010) 308–311.
[12] J. Lingner, M. Letz, G. Jakob, $SrTiO_3$ glass–ceramics as oxide thermoelectrics, J. Mater. Sci. 48 (2013) 2812–2816.
[13] N. Wang, et al., Enhanced thermoelectric performance of Nb-doped $SrTiO_3$ by nano-inclusion with low thermal conductivity, Sci. Rep. 3 (2013).
[14] K.H. Lee, S.W. Kim, H. Ohta, K. Koumoto, Ruddlesden–Popper phases as thermoelectric oxides: Nb-doped $SrO(SrTiO_3)_n (n \approx 1, 2)$, J. Appl. Phys. 100 (2006) 063717.
[15] S.N. Ruddlesden, P. Popper, The compound $Sr_3Ti_2O_7$ and its structure, Acta Crystallogr. 11 (1958) 54–55.
[16] Z. Li, X. Zhang, J. Hou, K. Zhou, Molten salt synthesis of anisometric $Sr_3Ti_2O_7$ particles, J. Cryst. Growth 305 (2007) 265–270.
[17] E.K. Akdogan, R. Brennan, M. Allahverdi, A. Safari, Effects of molten salt synthesis (MSS) parameters on the morphology of $Sr_3Ti_2O_7$ and $SrTiO_3$ seed crystals, J. Electroceram. 16 (2006) 159–165.
[18] Y.-f. Liu, Y.-n. Lu, M. Xu, L.-f. Zhoun, Formation mechanisms of platelet $Sr_3Ti_2O_7$ crystals synthesized by the molten salt synthesis method, J. Am. Ceram. Soc. 90 (2007) 1774–1779.
[19] J. de Boor, C. Stiewe, P. Ziolkowski, T. Dasgupta, G. Karpinski, E. Lenz, F. Edler, E. Mueller, High-temperature measurement of Seebeck coefficient and electrical conductivity, J. Electron. Mater. 42 (2013) 1711–1718.
[20] J. de Boor, E. Müller, Data analysis for Seebeck coefficient measurements, Rev. Sci. Instrum. 84 (2013) 065102.
[21] J. Brous, I. Fankuchen, E. Banks, Rare earth titanates with a perovskite structure, Acta Crystallogr. 6 (1953) 67–70.
[22] S. Šturm, A. Rečnik, C. Scheu, M. Čeh, Formation of Ruddlesden–Popper faults and polytype phases in SrO-doped $SrTiO_3$, J. Mater. Res. 15 (2000) 2131–2139.
[23] R. Franz, G. Wiedemann, Ueber die Wärme-Leitungsfähigkeit der Metalle, Annalen der Physik 165 (1853) 497–531.
[24] N. Tinh, T. Tsuji, Physics and engineering of new materials, in: DoTran Cat, Annemarie Pucci, Klaus Wandelt (Eds.), Springer Proceedings in Physics, vol. 127, Springer, Berlin, Heidelberg, 2009, pp. 209–217 (Chapter 24).
[25] T. Teranishi, Y. Ishikawa, H. Hayashi, A. Kishimoto, M. Katayama, Y. Inada, Thermoelectric efficiency of reduced $SrTiO_3$ ceramics modified with La and Nb, J. Am. Ceram. Soc. 96 (2013) 2852–2856.
[26] B. Feng, H.-P. Martin, A. Michaelis, In situ preparation and thermoelectric properties of B_4C_{1-x}–TiB_2 composites, J. Electron. Mater. 42 (2013) 2314–2319.
[27] T. Mori, T. Nishimura, K. Yamaura, E. Takayama-Muromachi, High temperature thermoelectric properties of a homologous series of n-type boron icosahedra compounds: a possible counterpart to p-type boron carbide, J. Appl. Phys. 101 (2007) 093714.
[28] A. Prytuliak, S. Maruyama, T. Mori, Anomalous effect of vanadium boride seeding on thermoelectric properties of $YB_{22}C_2N$, Mater. Res. Bull. 48 (2013) 1972–1977.
[29] T. Mori, T. Hara, Hybrid effect to possibly overcome the trade-off between Seebeck coefficient and electrical conductivity, Scr. Mater. 111 (2016) 44–48.
[30] Y. Kozuka, M. Kim, H. Ohta, Y. Hikita, C. Bell, H.Y. Hwang, Enhancing the electron mobility via delta-doping in $SrTiO_3$, Appl. Phys. Lett. 97 (2010) 222115.

Chapter 8

Conclusions

This thesis is focused on lowering the thermal conductivity of STNO ceramics in order to enhance its thermoelectric figure of merit (ZT). The investigation was based on the hypothesis that introducing planar faults in the basic STNO structure would preferentially scatter phonons without significantly disturbing the electrical transport. Prior to microstructure modifications, STNO was synthesized in different atmospheres in order to study the level of reduction and phase development based on the surrounding $P(O_2)$. Sintering STNO in different atmospheres showed significant impact on reduction of Ti^{4+} into Ti^{3+}. High $P(O_2)$ resulted in low reduction rate, which was seen from low relative increase of weight detected by the TGA in addition to a light gray color of the resulting pellets. On the contrary, low $P(O_2)$ led to dark gray/black color and a substantial relative increase of mass after oxidation. Furthermore, by annealing the samples in high $P(O_2)$, final pellets revealed some secondary phases, while single STNO phase was detected in the samples sintered in low $P(O_2)$.

Then, two different approaches were taken in order to introduce planar faults into the basic STNO matrix: either by adding RP-type seeds or by adding excess SrO or CaO to STNO. Also, a separate systematical study dealing with the influence of Nb-doping on $Sr_3Ti_2O_7$ platelet seeds formation and growth was employed. The preparation of Nb-doped $Sr_3Ti_2O_7$ seeds by the molten salt synthesis guided us to a conclusion that undoped product powder is the most appropriate to be added to STNO. Namely, the Nb-doped products contained a substantial portion of secondary phases which could result in undesired phases in the final seeded ceramics.

SrO and CaO excess doping of STNO resulted in more or less ordered planar faults in STNO matrix. Both additions resulted in significantly lowered thermal conductivity attributed to phonon scattering at the planar faults and in the case of CaO also due to mass-defect scattering between Sr and Ca and somewhat higher closed porosity. SrO addition completely transformed the basic STNO microstructure; up to 50 μm long lamellae were penetrating in the surrounding grains as well. The sample showed poor electrical conductivity and to finally lower ZT. On the other hand, CaO addition resulted in compact ceramics, with planar faults embedded in some isotropic grains. While the electrical conductivity was somewhat lower in comparison to STNO, the Seebeck coefficient was enhanced, which in the end led to improved ZT. STNO with RP-type seeds showed slightly lower thermal conductivity but significantly enhanced power factor which in the end resulted in 50% higher ZT at 650 °C in comparison with pure STNO. Additional studies on how porosity affects the thermal and electrical transport by excluding other parameters, such as secondary phases, structural disorder and/or point defects are reasonable future work in the STNO system.

In conclusion, the study showed that CaO excess doping and seeding is a prospective approach to modify the microstructure of STNO-type ceramics and consequently lower the thermal conductivity. Nevertheless, by following these approaches, some additional favorable effects can possibly occur, such as formation of highly conductive paths, which were observed in seeded STNO and also enhanced Seebeck coefficient due to mass defect between Sr and Ca in the STNO doped with excess CaO. However, the absolute ZT values obtained in this thesis are low in comparison to ZT of STNO reported in some papers. This could be connected to the synthesis conditions, since fabrication methods strongly influence the thermoelectric performance of the final material. Therefore it is reasonable to assume that there is room of improvement of the absolute values of ZT of microstructurally modified STNO by further optimizing the synthesis methods and conditions.

References

[1] T. J. Seebeck, "Model for Lattice Thermal Conductivity at Low Temperatures," *Ann. Phys.*, vol. 82, no. 3, pp. 253–286, 1926.

[2] J. Peltier, "New Experiments on the Heat Effects of Electric Currents," *Ann. Chim. Phys.*, vol. 56, pp. 371–386, 1934.

[3] W. Thomson, "On the Dynamical Theory of Heat," *Trans. R. Soc.*, vol. 1, pp. 174, 1951.

[4] G. J. Snyder and E. S. Toberer, "Complex Thermoelectric Materials," *Nat. Mater.*, vol. 7, no. 2, pp. 105–114, 2008.

[5] J. Goldsmid, *Introduction to Thermoelectrics*. Berlin: Springer Berlin Heidelberg, p. 242, 2010.

[6] T. M. Tritt, Ed., *Thermal Conductivity: Theory, Properties and Applications*. Springer US, p. 290, 2004.

[7] V. R. Peierls, "Zur kinetischen Theorie der Wärmeleitung in Kristallen," *Ann. Phys.*, vol. 395, no. 8, pp. 1055–1101, 1929.

[8] R. Franz and G. Wiedemann, "Ueber die Wärme-Leitungsfähigkeit der Metalle," *Ann. der Phys. und Chemie*, vol. 165, no. 8, pp. 497–531, 1853.

[9] J. Callaway, "Model for Lattice Thermal Conductivity at Low Temperatures," *Phys. Rev.*, vol. 113, no. 4, pp. 1046–1051, 1959.

[10] M. G. Holland, "Analysis of Lattice Thermal Conductivity," *Phys. Rev.*, vol. 132, no. 6, pp. 2461–2471, Dec. 1963.

[11] P. Blennow, A. Hagen, K. K. Hansen, L. R. Wallenberg, and M. Mogensen, "Defect and Electrical Transport Properties of Nb-Doped $SrTiO_3$," *Solid State Ionics*, vol. 179, no. 35–36, pp. 2047–2058, 2008.

[12] J. Tervo, A. Manninen, and R. Ilola, "State-of-the-Art of Thermoelectric Materials Processing," *VTT Work. Pap.*, p. 29, 2009.

[13] T. Mori and T. Hara, "Hybrid Effect to Possibly Overcome the Trade-off Between Seebeck Coefficient and Electrical Conductivity," *Scr. Mater.*, vol. 111, pp. 44–48, 2016.

[14] D. M. Rowe and G. Min, "Alfa-in Sigma Plot as a Thermoelectric Material Performance Indicator," *J. Mater. Sci. Lett.*, vol. 14, no. 9, pp. 617–619, 1995.

[15] H. Goldsmid, "Bismuth Telluride and Its Alloys as Materials for Thermoelectric

Generation," *Materials (Basel).*, vol. 7, no. 4, pp. 2577–2592, 2014.

[16] Y. Kawaharada, K. Kurosaki, M. Uno, and S. Yamanaka, "Thermoelectric Properties of $CoSb_3$," *J. Alloys Compd.*, vol. 315, no. 1, pp. 193–197, 2001.

[17] M. N. Tripathi and C. M. Bhandari, "High-Temperature Thermoelectric Performance of Si – Ge alloys," *J. Phys. Condens. Matter*, vol. 15, p. 5359, 2003.

[18] M. Fedorov and G. N. Icaschenko, "Silicides: Materials for Thermoelectric Energy Conversion," *Jpn. J. Appl. Phys.*, vol. 54, p. 07JA05, 2015.

[19] J. W. Fergus, "Oxide Materials for High Temperature Thermoelectric Energy Conversion," *J. Eur. Ceram. Soc.*, vol. 32, no. 3, pp. 525–540, 2012.

[20] J. He, Y. Liu, and R. Funahashi, "Oxide Thermoelectrics: The challenges, Progress, and Outlook," *J. Mater. Res.*, vol. 26, no. 15, pp. 1762–1772, 2011.

[21] I. Terasaki, "Large Thermoelectric Power in $NaCo_2O_4$ Single Crystals," *Phys. Rev. Lett. B*, vol. 56, pp. 55–56, 1997.

[22] M. L. Foo, T. Klimczuk, and R. J. Cava, "Hydration Phase Diagram for Sodium Cobalt Oxide $Na_{0.3}CoO_2 \cdot yH_2O$," *Mater. Res. Bull.*, vol. 40, no. 4, pp. 665–670, Apr. 2005.

[23] D. Vengust, B. Jancar, A. Sestan, M. Ponikvar Svet, B. Budic, and D. Suvorov, "Chemical Decomposition as a Likely Source of Ambient and Thermal Instabilities of Layered Sodium Cobaltate," *Chem. Mater.*, vol. 25, no. 23, pp. 4791–4797, 2013.

[24] M. Shikano and R. Funahashi, "Electrical and Thermal Properties of Single-Crystalline $(Ca_2CoO_3)_{0.7}CoO_2$ with a $Ca_3Co_4O_9$ Structure," *Appl. Phys. Lett.*, vol. 82, no. 12, p. 1851, 2003.

[25] S. Li, R. Funahashi, I. Matsubara, K. Ueno, S. Sodeoka, and H. Yamada, "Synthesis and Thermoelectric Properties of the New Oxide Materials $Ca_{(3-x)}Bi_xCo_4O_{(9-\delta)}$ $(0.0 < x < 0.75)$," *Chem. Mater.*, vol. 12, no. 8, pp. 2424–2427, 2000.

[26] H. Itahara, J. Sugiyama, and T. Tani, "Enhancement of Electrical Conductivity in Thermoelectric $[Ca_2CoO_3]_{0.62}[CoO_2]$ Ceramics by Texture Improvement," *Japanese J. Appl. Physics, Part 1 Regul. Pap. Short Notes Rev. Pap.*, vol. 43, no. 8 A, pp. 5134–5139, 2004.

[27] M. Ohtaki, H. Koga, T. Tokunaga, K. Eguchi, and H. Arai, "Electrical Transport Properties and High-Temperature Thermoelectric Performance of $(Ca_{0.9}M_{0.1})MnO_3$ (M = Y, La, Ce, Sm, In, Sn, Sb, Pb, Bi)," *J. Solid State Chem.*, vol. 120, no. 1, pp. 105–111, 1995.

[28] P. Tomeš, R. Robert, M. Trottmann, L. Bocher, M. H. Aguirre, A. Bitschi, J. Hejtmánek, and A. Weidenkaff, "Synthesis and Characterization of New Ceramic Thermoelectrics Implemented in a Thermoelectric Oxide Module," *J. Electron. Mater.*, vol. 39, no. 9, pp. 1696–1703, 2010.

[29] M. Ohtaki, T. Tsubota, K. Eguchi, and H. Arai, "High-Temperature

Thermoelectric Properties of $(Zn_{1-x}Al_x)O$," *J. Appl. Phys.*, vol. 79, no. 3, pp. 1816–1818, 1996.

[30] H. Ohta, W.-S. Seo, and K. Koumoto, "Thermoelectric Properties of Homologous Compounds in the ZnO–In_2O_3 System," *J. Am. Ceram. Soc.*, vol. 79, no. 8, pp. 2193–2196, 1996.

[31] H. Takemoto, H. Kawakami, M. Saito, and H. Yamamur, "Thermoelectric Properties of $Zn_{1-(x+y)}Ga_xIn_yO$ (x + y = 0.007) System," *Procedia Eng.*, vol. 36, pp. 434–438, 2012.

[32] Y. Masuda, M. Ohta, W.-S. Seo, W. Pitschke, and K. Koumoto, "Structure and Thermoelectric Transport Properties of Isoelectronically Substituted $(ZnO)_5In_2O_3$," *J. Solid State Chem.*, vol. 150, no. 1, pp. 221–227, 2000.

[33] M. Ohtaki, K. Araki, and K. Yamamoto, "High Thermoelectric Performance of Dually Doped ZnO Ceramics," *J. Electron. Mater.*, vol. 38, no. 7, pp. 1234–1238, 2009.

[34] R. Moos, A. Gnudi, and K. H. Härdtl, "Thermopower of $Sr_{1-x}La_xTiO_3$ Ceramics," *J. Appl. Phys.*, vol. 78, no. 8, pp. 5042–5047, 1995.

[35] W. Wunderlich, S. Ohta, H. Ohta, K. Koumoto, and T. Agency, "Effective Mass and Thermoelectric Properties of $SrTiO_3$ -Based Natural Superlattices Evaluated by Ab-Initio Calculations," *25th Int. Conf. Thermoelctrics*, no. 2, pp. 237–240, 2005.

[36] M. Ito and T. Matsuda, "Thermoelectric Properties of Non-Doped and Y-Doped $SrTiO_3$ Polycrystals Synthesized by Polymerized Complex Process and Hot Pressing," *J. Alloys Compd.*, vol. 477, no. 1–2, pp. 473–477, 2009.

[37] A. Kikuchi, N. Okinaka, and T. Akiyama, "A Large Thermoelectric Figure of Merit of La-Doped $SrTiO_3$ Prepared by Combustion Synthesis with Post-Spark Plasma Sintering," *Scr. Mater.*, vol. 63, no. 4, pp. 407–410, 2010.

[38] M. Onoda and I. Goto, "Correlation and Phonon Effects for the Electronic Transport and Thermoelectric Power Factors in the Metal-Band-Insulator Crossover of Perovskite-Type Titanates.," *J. Phys. Condens. Matter*, vol. 21, p. 435603, 2009.

[39] N. T. Tinh and T. Tsuji, "Thermoelectric Properties of Heavily Doped Polycrystalline $SrTiO_3$," in *Physics and Engineering of New Materials*, 2009, pp. 209–217.

[40] J. Fukuyado, K. Narikiyo, M. Akaki, H. Kuwahara, and T. Okuda, "Thermoelectric Properties of the Electron-Doped Perovskites $Sr_{1-x}Ca_xTi_{1-y}Nb_yO_3$," *Phys. Rev. B - Condens. Matter Mater. Phys.*, vol. 85, no. 7, pp. 1–9, 2012.

[41] K. H. Lee, S. W. Kim, H. Ohta, and K. Koumoto, "Ruddlesden-Popper Phases as Thermoelectric Oxides: Nb-Doped $SrO(SrTiO_3)n$ (n=1,2)," *J. Appl. Phys.*, vol. 100, no. 6, pp. 1–7, 2006.

[42] B. Zhang, J. Wang, T. Zou, S. Zhang, X. Yaer, N. Ding, C. Liu, L. Miao, Y. Li, and Y. Wu, "High Thermoelectric Performance of Nb-Doped $SrTiO_3$ Bulk Materials with Different Doping Levels," *J. Mater. Chem. C*, vol. 3, no. 43, pp. 11406–11411, 2015.

[43] S. Ohta, H. Ohta, and K. Koumoto, "Grain Size Dependence of Thermoelectric Performance of Nb-Doped $SrTiO_3$ Polycrystals," *J. Ceram. Soc. Japan*, vol. 114, no. 1, pp. 102–105, 2006.

[44] R. Loetzsch, A. Lübcke, I. Uschmann, E. Förster, V. Groe, M. Thuerk, T. Koettig, F. Schmidl, and P. Seidel, "The Cubic to Tetragonal Phase Transition in $SrTiO_3$ Single Crystals Near its Surface Under Internal and External Strains," *Appl. Phys. Lett.*, vol. 96, no. 7, pp. 3–5, 2010.

[45] V. M. Goldschmidt, "Die Gesetze der Krystallochemie," *Naturwissenschaften*, vol. 14, no. 21, pp. 477–485, 1926.

[46] T. Tomio, H. Miki, H. Tabata, T. Kawai, and S. Kawai, "Control of Electrical Conductivity in Laser Deposited $SrTiO_3$ Thin Films with Nb Doping," *J. Appl. Phys.*, vol. 76, no. 10, pp. 5886–5890, 1994.

[47] J. Karczewski, B. Riegel, M. Gazda, P. Jasinski, and B. Kusz, "Electrical and Structural Properties of Nb-Doped $SrTiO_3$ Ceramics," *J. Electroceramics*, vol. 24, no. 4, pp. 326–330, 2010.

[48] T. A. Vanderah, A. R. Drews, R. S. Roth, J. M. Loezos, and I. Levin, "SrO-TiO_2-Nb_2O_5," 2005.

[49] S. Witek, D. M. Smyth, and H. Piclup, "Variability of the Sr/Ti Ratio in $SrTiO_3$," *J. Am. Ceram. Soc.*, vol. 67, no. 5, pp. 372–375, 1984.

[50] S. N. Ruddlesden and P. Popper, "The Compound $Sr_3Ti_2O_7$ and its Structure," *Acta Crystallogr.*, vol. 11, no. 1, pp. 54–55, 1958.

[51] G. Rijnders, "Oxide Heterostructures: Atoms on the Move," *Nat Mater*, vol. 13, no. 9, pp. 844–845, Sep. 2014.

[52] R. Moos and K. H. Hardtl, "Defect Chemistry of Donor-Doped and Undoped Strontium Titanate Ceramics Between 1000 Degrees and 1400 Degrees C," *J. Am. Ceram. Soc.*, vol. 80, no. 10, pp. 2549–2562, 1997.

[53] F. A. Kröger and H. J. Vink, "Relations between the Concentrations of Imperfections in Crystalline Solids," *Solid State Phys.*, vol. 3, pp. 307–435, 1956.

[54] S.-Y. Chung, S.-J. L. Kang, and V. P. Dravid, "Effect of Sintering Atmosphere on Grain Boundary Segregation and Grain Growth in Niobium-Doped $SrTiO_3$," *J. Am. Ceram. Soc.*, vol. 85, no. 11, pp. 2805–2810, 2002.

[55] S. Y. Chung, D. Y. Yoon, and S. J. L. Kang, "Effects of Donor Concentration and Oxygen Partial Pressure on Interface Morphology and Grain Growth Behavior in $SrTiO_3$," *Acta Mater.*, vol. 50, no. 13, pp. 3361–3371, 2002.

[56] R. Waser, "Proton Solubility in Undoped and Fe-doped SrTiO3: Temperature Dependence and Formation of Defect Associates," *Zeitschrift fur Naturforsch. -*

Sect. A J. Phys. Sci., vol. 42, no. 11, pp. 1357–1365, 1987.

[57] R. Moos and K. H. Hardtl, "Dependence of the Intrinsic Conductivity Minimum of $SrTiO_3$ Ceramics on the Sintering Atmosphere," *J. Am. Ceram. Soc.*, vol. 78, no. 9, pp. 2569–2571, 1995.

[58] K. Van Benthem, C. Elsässer, and R. H. French, "Bulk Electronic Structure of $SrTiO_3$: Experiment and Theory," *J. Appl. Phys.*, vol. 90, no. 12, pp. 6156–6164, 2001.

[59] R. Z. Zhang, X. Y. Hu, P. Guo, and C. L. Wang, "Thermoelectric Transport Coefficients of n-Doped $CaTiO_3$, $SrTiO_3$ and $BaTiO_3$: A Theoretical Study," *Phys. B Condens. Matter*, vol. 407, no. 7, pp. 1114–1118, 2012.

[60] X. G. Guo, X. S. Chen, Y. L. Sun, L. Z. Sun, X. H. Zhou, and W. Lu, "Electronic Band Structure of Nb Doped $SrTiO_3$ from First Principles Calculation," *Phys. Lett. Sect. A Gen. At. Solid State Phys.*, vol. 317, no. 5–6, pp. 501–506, 2003.

[61] S. Hashimoto, F. W. Poulsen, and M. Mogensen, "Conductivity of $SrTiO_3$ Based Oxides in the Reducing Atmosphere at High Temperature," *J. Alloys Compd.*, vol. 439, no. 1–2, pp. 232–236, 2007.

[62] S. Suthirakun, S. C. Ammal, G. Xiao, F. Chen, H.-C. zur Loye, and A. Heyden, "Density Functional Theory Study on the Electronic Structure of n- and p-type Doped $SrTiO_3$ at Anodic Solid Oxide Fuel Cell Conditions," *Phys. Rev. B*, vol. 84, no. 20, pp. 1–9, 2011.

[63] S. Ohta, T. Nomura, H. Ohta, and K. Koumoto, "High-Temperature Carrier Transport and Thermoelectric Properties of Heavily La- or Nb-Doped $SrTiO_3$ Single Crystals," vol. 034106, pp. 18–21, 2005.

[64] S. Ohta, T. Nomura, H. Ohta, M. Hirano, H. Hosono, and K. Koumoto, "Large Thermoelectric Performance of Heavily Nb-Doped $SrTiO_3$ Epitaxial Film at High Temperature," *Appl. Phys. Lett.*, vol. 87, no. 9, pp. 2–5, 2005.

[65] J. T. S. Irvine, P. R. Slater, and P. A. Wright, "Synthesis and Electrical Characterisation of the System Sr1-xYxTi1-xCoxO3," in *Solid State Ionics*, 1996, vol. 2, pp. 213–216.

[66] A. Frye, R. H. French, and D. A. Bonnell, "Optical Properties and Electronic Structure of Oxidized and Reduced Single-Crystal Strontium Titanate," *Zeitschrift für Met.*, vol. 94, no. 3, pp. 226–232, 2003.

[67] T. Yamamoto and Y. Ikuhara, "Electron Transport Behaviour in Nb-Doped $SrTiO_3$ Bicrystals," *J. Electron Microsc. (Tokyo).*, vol. 50, no. 6, pp. 485–488, 2001.

[68] K. Koumoto, R. Funahashi, E. Guilmeau, Y. Miyazaki, A. Weidenkaff, Y. Wang, and C. Wan, "Thermoelectric Ceramics for Energy Harvesting," *J. Am. Ceram. Soc.*, vol. 96, no. 1, pp. 1–23, 2013.

[69] K. A. Borup, J. de Boor, H. Wang, F. Drymiotis, F. Gascoin, X. Shi, L. Chen,

M. I. Fedorov, E. Müller, B. B. Iversen, and G. J. Snyder, "Measuring Thermoelectric Transport Properties of Materials," *Energy Environ. Sci.*, vol. 8, pp. 423–435, 2015.

[70] Y. Wang, K. Fujinami, R. Zhang, C. Wan, N. Wang, Y. Ba, and K. Koumoto, "Interfacial Thermal Resistance and Thermal Conductivity in Nanograined $SrTiO_3$," *Appl. Phys. Express*, vol. 3, no. 3, pp. 5–7, 2010.

[71] N. Wang, L. Han, H. He, Y. Ba, and K. Koumoto, "Effects of Mesoporous Silica Addition on Thermoelectric Properties of Nb-Doped $SrTiO_3$," *J. Alloys Compd.*, vol. 497, no. 1–2, pp. 308–311, 2010.

[72] J. Lingner, M. Letz, and G. Jakob, "$SrTiO_3$ Glass-Ceramics as Oxide Thermoelectrics," *J. Mater. Sci.*, vol. 48, no. 7, pp. 2812–2816, 2013.

[73] N. Wang, H. Chen, H. He, W. Norimatsu, M. Kusunoki, and K. Koumoto, "Enhanced Thermoelectric Performance of Nb-Doped $SrTiO_3$ by Nano-Inclusion with Low Thermal Conductivity," *Sci. Rep.*, vol. 3, p. 3449, Dec. 2013.

[74] S. Walia, S. Balendhran, H. Nili, S. Zhuiykov, G. Rosengarten, Q. H. Wang, M. Bhaskaran, S. Sriram, M. S. Strano, and K. Kalantar-zadeh, "Transition Metal Oxides - Thermoelectric Properties," *Prog. Mater. Sci.*, vol. 58, no. 8, pp. 1443–1489, 2013.

[75] B. Godart, C., Goncalves, A. P., Lopes, E. B., Villeroy, "Role of Structures on Thermal conductivity in Thermoelectric materials," in *Properties and Applications of Thermoelectric materials*, A. C. Zlatić, Veljko, Hewson, Ed. Springer Netherlands, 2009, pp. 19–49.

[76] P. Jood, R. J. Mehta, Y. Zhang, T. Borca-Tasciuc, S. X. Dou, D. J. Singh, and G. Ramanath, "Heavy Element Doping for Enhancing Thermoelectric Properties of Nanostructured Zinc Oxide," *RSC Adv.*, vol. 4, no. 13, pp. 6363–6368, 2014.

[77] A. F. Ioffe, S. V. Airapetiants, A. V. Ioffe, N. V. Kolomoets, and L. S. StilBans, "On Increasing the Efficiency of Semiconductor Thermocouples," *Sov. Phys. Dokl.*, vol. 1, p. 132, 1956.

[78] D. M. Rowe (ed.) *CRC Handbook of Thermoelectrics*. CRC press, p. 701, 1995.

[79] M. S. Dresselhaus, G. Chen, M. Y. Tang, R. G. Yang, H. Lee, D. Z. Wang, Z. F. Ren, J.-P. Fleurial, and P. Gogna, "New Directions for Low-Dimensional Thermoelectric Materials," *Adv. Mater.*, vol. 19, no. 8, pp. 1043–1053, 2007.

[80] M. Broström, S. Enestam, R. Backman, and K. Mäkelä, "Condensation in the KCl – NaCl System," *Fuel Process. Technol.*, vol. 105, pp. 142–148, 2013.

[81] J. De Boor, C. Stiewe, P. Ziolkowski, T. Dasgupta, G. Karpinski, E. Lenz, F. Edler, and E. Mueller, "High-Temperature Measurement of Seebeck Coefficient and Electrical Conductivity," *J. Electron. Mater.*, vol. 42, no. 7, pp. 1711–1718, 2013.

[82] P. Blennow, K. K. Hansen, L. R. Wallenberg, and M. Mogensen, "Electrochemical Characterization and Redox Behavior of Nb-Doped $SrTiO_3$,"

Solid State Ionics, vol. 180, no. 1, pp. 63–70, 2009.

[83] M. Jerič, J. de Boor, J. Zavašnik, and M. Čeh, "Lowering the Thermal Conductivity of $Sr(Ti_{0.8}Nb_{0.2})O_3$ by SrO and CaO Doping: Microstructure and Thermoelectric Properties," *J. Mater. Sci.*, vol. 51, no. 16, pp. 7660–7668, 2016.

[84] M. Jerič, J. de Boor, B. Jančar, and M. Čeh, "An Enhanced Thermoelectric Figure of Merit for $Sr(Ti_{0.8}Nb_{0.2})O_3$ Based on a Ruddlesden–Popper-Polytype-Induced Microstructure," *J. Eur. Ceram. Soc.*, vol. 36, no. 5, pp. 1177–1182, 2016.

Bibliography

Journal Articles

Jerič M, de Boor J, Jančar B, Čeh M. An enhanced thermoelectric figure of merit for $Sr(Ti_{0.8}Nb_{0.2})O_3$ based on a Ruddlesden–Popper-polytype-induced microstructure. *J Eur Ceram Soc.* 2016;36(5):1177-1182.

Jerič M, de Boor J, Zavašnik J, Čeh M. Lowering the thermal conductivity of $Sr(Ti_{0.8}Nb_{0.2})O_3$ by SrO and CaO doping: microstructure and thermoelectric properties. *J Mater Sci.* 2016;51(16):7660-7668.

Conference Paper

Jerič, M., Čeh, M. (2012) "Synthesis and characterisation of Ti-site doped $SrTiO_3$ and Sr- and Ti-site doped layered perovskite $SrO(SrTiO_3)_n$ (n=1,2,3…) as a n-type thermoelectric material" in *Program and book of abstracts of the 20th Juliee Conference on Materials and Technology*, Portorož, Slovenia, Inštitut za kovinske materiale in tehnologije.

Jerič, M., Čeh, M. (2013) "Molten salt synthesis of Nb-doped $Sr_3Ti_2O_7$ platelet seeds" In 21st International conference on Materials and Technology, Portorož, Slovenia, Inštitut za kovinske materiale in tehnologije.

Jerič, M., Čeh, M. (3013) "Microstucture of Nb-SrTiO3 ceramics with SrO-excess and with addition of platelet seeds" In 11th European conference on Thermoelectrics, Noordwijk, Netherlands, European Thermoelectric society.

Jerič, M., Čeh, M. (2014): "Microstructure of Nb-doped strontium titanate thermoelectric materials" In Program and abstract book of the 8th Young researchers day, Ljubljana, Slovenia, Jožef Stefan Institute.

Gec, M., Jerič, M., Čeh, M. (2014) "Nb-doped $Sr_3Ti_2O_7$ platelets: preparation and cross-section thin foils for TEM observation" Abstract book of the 18th International Microscopy congress, Prague, Czech Republic.

Čeh, M., Jerič, M., Šturm, S., Košir, M., Bernik, Ow.Yang, C., Gulgun, M.A. (2014) "HAADF and ABF STEM imaging of SrO-doped $Sr(Ti,Nb)O_{3-\delta}$ and In_2O_3-doped ZnO thermoelectrics" in Book of abstracts and Souvenir of the International conference on Electron Microscopy& 25th Annual Meeting of electron micoscope society of India (EMSI), New Delhi, India, Delhi: Janvani Prakashan Pvt. Ltd.

Jerič, M., de Boor, J., Čeh, M. (2015) "Thermoelectric properties of Nb-doped SrTiO3 with excess CaO doping" In book of abstracts of the 34th Annual International Conference on thermoelectric (ICT 2015) and 13th European Conference on Thermoelectrics (ECT 2015), Dresden, Germany, International Thermoelectric society and European Thermoelectric society.

Šturm, S., Tchernychova, E., Ow-Yang, C., Inan, G., Jerič, M., Čeh, M. (2015) "Applications of scanning transmission electron microscopy (STEM). In book of tutorials and abstracts of 14th European workshop on modern developments and applications in microbeam analysis, Portorož, Slovenia. Antwerpen EMAS.

Čeh, M., Jerič, M., Šturm, S., Košir, M., Bernik, S., Ow-Yang, C. Gulgun, M. A. (2015) "STEM investigations of Sr(Ti,Nb)O_3-based and In_2O_3-doped ZnO thermoelectrics" In interamerican microscopy congress, Isla de Margarita, Venezuela.

Jerič, M., Čeh, M. (2015) "Microstructure and thermoelectric properties of $Sr(Ti_{0.8}Nb_{0.2})O_3$ with addition of SrO and CaO" in Conference program of the Electronic materials and Applications, Orlando, Florida, USA, American Ceramic Society.

Čeh, M., Jerič, M., Šturm, S., Košir, M., Bernik, Ow.Yang, C., Gulgun, M.A. (2015) "High-resolution STEM imaging of oxide materials for thermoelectric applications" in Program and book of abstracts of the 23th international conference on Materials and Technology, Portorož, Slovenia, Inštitut za kovinske materiale in tehnologije.

Biography

The author of this thesis, Marja Jerič, was born on December 4th, 1985 in Slovenj Gradec, Slovenia. After graduating from Gimnasium Velenje in 2004 she enrolled the bachelor study at the University of Ljubljana, Faculty of Natural and Technical Sciences at the Department of Geology. In 2008 she attended a ten-day international student exchange with the topic »Green propulsion«, in Liege, Belgium, organized by the Board of European Students of Technology. She defended her bachelor thesis in 2009 entitled: "Geophysical survey with multichannel analysis of surface waves in Vrbina area near Krško" under the supervision of Prof. Dr. Andrej Gosar and was awarded the title Bachelor of Geology. In 2010 she enrolled into the Jožef Stefan Postgraduate School, Nanosciences and Nanotechnologies programme, within the Young Researchers programme by the Slovenian Research Agency (ARRS). The topic of her research was synthesis and microstructural and thermoelectrical characterisation of thermoelectric materials based on strontium titanate. In 2013 she was awarded for the best poster presentation at the 21th International Conference on Materials and Technology in Portorož, Slovenia. In 2015 she spent three months at the German Aerospace Center, Institute of Materials Research, Department of Thermoelectric Materials and Systems, Cologne, Germany, where she employed new synthesis methods and got familiar with thermoelectric measurement techniques under the supervision of Dr. Johannes de Boor. She presented her work in the field of oxide-based thermoelectrics at several international conferences in Slovenia (2012, 2013, 2016), Germany (2015) and the Netherlands (2013).